

THESIS / THÈSE

DOCTOR OF SCIENCES

Design of polymer coatings on Nitinol by surface-initiated polymerization Towards cardiovascular applications

Arrotin, Bastien

Award date:
2018

Awarding institution:
University of Namur

[Link to publication](#)

General rights

Copyright and moral rights for the publications made accessible in the public portal are retained by the authors and/or other copyright owners and it is a condition of accessing publications that users recognise and abide by the legal requirements associated with these rights.

- Users may download and print one copy of any publication from the public portal for the purpose of private study or research.
- You may not further distribute the material or use it for any profit-making activity or commercial gain
- You may freely distribute the URL identifying the publication in the public portal ?

Take down policy

If you believe that this document breaches copyright please contact us providing details, and we will remove access to the work immediately and investigate your claim.



UNIVERSITÉ
DE NAMUR

UNIVERSITÉ DE NAMUR

FACULTÉ DES SCIENCES
DÉPARTEMENT DE CHIMIE



UNIVERSITÉ DE MONS

FACULTÉ DES SCIENCES
DÉPARTEMENT DE CHIMIE

Design of polymer coatings on Nitinol by surface-initiated polymerization
Towards cardiovascular applications

Committee Members:

Prof. S. Lucas; UNamur (President)
Prof. Z. Mekhalif; UNamur (Advisor)
Dr. L. Mespouille; UMONS (Co-advisor)
Prof. P. Dubois; UMONS
Dr. J.-F. Vanhumbecq; CRM Group

Dissertation presented by
Bastien ARROTIN
for the degree of PhD in Sciences

December 2018

« If you want to go fast, go alone.
If you want to go far, go together.»

African Proverb

« Anything that can go right, will go right »

Yhprum's law

Foreword

Dear reader,

Before we slip into the serious world of science, I would like to bring you back into the past for a couple of minutes. Do you reminisce of “Once Upon a Time... Life”? You know, this 80’s educative animated series with characters living in our bodies and riding through our veins? I’m pretty sure you do! But did you ever wonder what would happen to them in case of a road fatality, or of a collapsed tunnel? This phenomenon, commonly known as clot, may have serious consequences and lead to a stroke or a heart attack. But don’t worry, there’s a solution! Scientists developed a metallic resort-like material called “stent”, which will act as an intern tunnel and reinforce the failing structure. One of the most promising material in this context is a nickel/titanium alloy that will behave like a rubber band to adapt the exact shape of the vessel. Because obviously, a vessel is more flexible than a road, so should be our brace!

That’s all well and good, but this already exists! And as you can imagine, all is not yet rosy. We still have two issues to face. First, like for every road, we have to ensure its maintenance and prevent it from deterioration. We have to admit Belgians are not very talented for this, but in the human body, the smallest rubble might have strong adverse effects. We thus need to be very cautious! The second issue we have to face relies on the fact that such structure has been optimized for vehicles, but on the road, there are also many pedestrians. Wouldn’t it be a shame after so much efforts that one of them stumbles over a mesh, falls, and creates a new congestion? That would be completely counterproductive!

That is where I come in with my thesis, the aim of which is to bring small molecules (called monomers) together and to weave them into a carpet that we will call “polymer”. This carpet should protect the structure from any damage, permit unobstructed movements of the little buddies, as well as blend the framework in its brand-new environment (Don’t you find a decorated room nicer than a cold metallic cage? I do think so...). I know some of you might be sceptical, and ready to tell me “Okay, a carpet is nice, but that picks up dust and can be tricky to clean!”, and you would be right! But what if I tell you that instead of dust, we could impregnate the carpet with drugs, ready to heal to patient directly after the surgery, and right on the spot? Wouldn’t that be great? I hope that this manuscript will convince you, because after all, like in all good stories, our characters also deserve to live happily (and healthy) ever after...

Adapted from the speech presented on MT180 2017 (Namur)
<https://www.youtube.com/watch?v=KM6I2QASJr>

Université de Namur
Facultés des Sciences
Rue de Bruxelles 61, 5000 Namur (BE)

Université de Mons
Facultés des Sciences
Place du Parc 20, 7000 Mons (BE)

**Design of polymer coatings on Nitinol by surface-initiated polymerization
Towards cardiovascular applications**

By Bastien Arrotin

Abstract:

Over the last decade Nitinol (NiTi) has become very appealing owing to its attractive properties (good impact and heat resistance, high fatigue strength, low density, ...). Nowadays, it is commonly used as a support material for the treatment of cardiovascular disease where it is used as a stent. However, its implementation in the biomedical fields is still hampered by nickel inclusions, making this alloy sensitive to pitting corrosion and leading therefore to the release of carcinogenic Ni²⁺ ions.

The present thesis is devoted to the improvement of NiTi properties. The main objectives are to increase the material corrosion resistance, its biocompatibility, as well as its hydrophilicity to prevent the adhesion of fat and proteins on its surface. In this context, three steps are considered and investigated: (a) the hydrothermal reinforcement of Nitinol native oxide layer; (b) the elaboration of an organic monolayers containing polymerization moieties; and (c) the subsequent growth of a biocompatible layer. More specifically, the electro-assisted elaboration of self-assembled monolayers (SAM) is proven to allow fast preparation of protective coatings in mild conditions while preventing degradation of sensitive molecules such as the ATRP initiating sites. However, the steric hindrance of ATRP initiating sites interferes with the formation of ordered and compact SAMs, leading to a bad reinforcement of the metal surface corrosion resistance. To face this issue, the elaboration of alternative initiating layers, *i.e.* mixed- or bisphosphonic-made monolayers, are investigated. Finally, the behaviour of modified Nitinol plates in human blood plasma simulated fluid, and its ability to grow endothelial cells are investigated.

PhD Thesis in Chemical Sciences

7th December 2018

Laboratory of Chemistry and Electrochemistry of Surfaces (University of Namur)

Laboratory of Polymeric and Composite Materials (University of Mons)

Supervisors: Prof. Zineb Mekhalif, Dr. Laetitia Mespouille

Acknowledgment

With this manuscript comes the end of a 11-years long era, a period full of study, of work, but also full of friends, trips and good moments. I'm grateful to many people, and I can't go further in this manuscript without thanking them.

First and foremost, I would like to express my gratitude to Prof. Zineb Mekhalif as well as to Prof. Joseph Delhalle and Prof. Philippe Dubois for their guidance and their precious advices through the thesis, but also for believing in me and giving me the opportunity to achieve this thesis in their respective labs.

I also would like to thank the members of the committee, Prof. Philippe Dubois, Prof. Stéphane Lucas and Dr. Jean-François Vanhumbecq, who accepted to be part of this journey by reading and evaluating this manuscript, and for their valuable feedback that helped improving its quality.

During my thesis, I had the opportunity to collaborate with people from different expertise fields. Among them, I would like to thank Dr. Frédéric Kanoufi from Itodys (Paris) for his warm welcome in his team, and Dr. Jean-Marc Noël who took some of his precious time back then to train me on SECM. I would also like to thank Prof. Stéphane Carlier and Dr. Kathleen Thayse from the University of Mons for their help and advices on the biomedical aspects of this thesis as well as for the cell growth studies.

My story in the Laboratory of Chemistry and Electrochemistry started in 2012 with a master thesis, a period over which I met many people who beyond being colleagues became friends. I first would like to thank Amory and Sébastien D., who were my first mentors back in my early days in CES, for their patience and their guidance through my master thesis. I am also warmly thanking all the past and current CES members: Tania, Arvind, Bastien Sr., Anthony, Grégory, Alexandre, Marie, Carolyn, Guillaume, Annelies, Jonathan and Mohamed. It was a privilege and a real pleasure to work along with them. I am obviously not forgetting Simon and Sébastien V.: thank you for all the constructive scientific discussions and for your support during the end of the thesis.

In 2014, I had the pleasure to join a second team in the Laboratory of Polymer and Composite Materials, where I had the opportunity to meet people from around the world. I would especially like to thank Antoniya, Florence, Ameni, Noémie, Sébastien D., Romain, Sébastien M., Samira, Rosica, Bertrand and Valentina for all the moments we shared together. I'm not forgetting Alexandra, Nico, Alexandre, Xavier and Rémi! Thank you for all the "out of work" moments we're having since 2014.

Many thanks also to Sarah for the many times she helped me and for all the discussions we had, to Jérémy, Manu and Maximilien for the good atmosphere of the 4th floor, and to Valérie, Cory, Pierre and Alexandre for their help in their respective fields.

Before all this thesis stuff, I've been through several years of study, along with classmates that turned out to become real friends and extended our circle with their life mates. I'm obviously talking about Jennifer & Maxime, Amandine & Thomas, Simon & Maïté, Thomas & France, Laurent & Analilia, Julien & Valentine, John & Audrey, Coralie & Pierre-Alexandre and Quentin. I would like to thank them for all the good moments we had back then, and that we keep on having since the end of the Master.

If I am here today and became a chemist, it is also thanks to Véronique Alin who was the first to give me a taste for chemistry back in highschool, and who brought me to the university of Namur for my first practical session there. Thank you for believing in me and for your support back then.

I would definitely not be here without the help and the support of my family during those long years of study. I would especially like to thank my parents, Patricia & Marc, who gave me the opportunity to follow my passion, and encouraged me all those years, in the good as well as in the bad moments. Thank you for everything you did for me!

Last but not least, I would like to thank Jonathan. He is the one who believed in me, who outstandingly supported me during the writing of the thesis, and who advised me when I was way too picky with the graphs and illustrations. Most importantly, and away from science, he is also the one who taught me the true meaning of love, of happiness, of sharing and of (self-)confidence during that period. Thank you from the bottom of my heart for the valuable moments we share, and what this relationship brings to me day after day.

Abbreviations & symbols

ACS	Acute Coronary Syndrome
A_f	Austenite finish temperature
A_s	Austenite start temperature
ATRP	Atom Transfer Radical Polymerization
AFM	Atomic Force Microscopy
BE	Binding Energy
BES	Balloon-Expandable Stent
BMS	Bare Metal Stent
BUPA	11-(2-bromoisobutyrate)-undecyl-1-phosphonic acid
C_1P	Methylphosphonic acid
$C_{10}P$	Decylphosphonic acid
$C_{12}P$	Dodecylphosphonic acid
CAD	Coronary Artery Disease
CE	Conformité Européenne
CH	Conventionnal Heating
CPE	Constant Phase Element
CRP	Controlled Radical Polymerization
CV	Cyclic Voltammerty
CVD	Cardiovascular Disease
DES	Drug-Eluting Stent
DIP_2	(Dodecylimino)dimethylene bisphosphonic acid
DMAEMA	2-(Dimethylamino)ethyl methacrylate
E	Potential
E_{corr}	Corrosion Potential
EC	Electrochemical
EIS	Electrochemical Impedance Spectroscopy
FB	Feedback
FDA	Food and Drug Administration
HEP_2	1-Hydroxyethylidene-1,1-diphosphonic acid
HMTETA	1,1,4,7,10,10-hexamethyltriethylene
HT	Hydrothermally Treated
ICP-OES	Optical Emission Spectroscopy coupled with Inductively Coupled Plasma
IE	Inhibition Efficiency
ISR	In-Stent Restenosis
j	Current density

j_{corr}	Corrosion current density
k_{ct}	Apparent charge transfer rate constant
LST	Late-Stent Thromobosis
LSV	Linear Sweep Voltammetry
M_{d}	Martensite Deformation Temperature
M_{f}	Martensite Finish Temperature
MI	Myocardial Infarction
MIH	Magnetic Induction Heating
MIP_2	(Methylimino)dimethylene bisphosphonic acid
MPC	2-Methacryloyloxyethyl Phosphorylcholine
M_{s}	Martensite start temperature
MW	Molecular Weight
MWD	Molecular Weight Distribution
NiTi	Nitinol
OCP	Open-Circuit Potential
PM-IRRAS	Polarization Modulation-Infrared Reflection-Absorption Spectroscopy
Q_{dl}	Double layer CPE
Q_{ox}	Oxide layer CPE
R_{ct}	Charge transfer resistance
R_{el}	Electrolyte resistance
R_{ox}	Oxide layer resistance
ROS	Reactive Oxygen Species
RP	Radical Polymerization
RT	Room Temperature
SAM	Self-Assembled Monolayer
SCE	Saturated Calomel Electrode
SECM	Scanning Electrochemical Microscopy
SES	Self-Expanding Stent
SI-ATRP	Surface-Initiated ATRP
SMCs	Smooth Muscle Cells
T	Temperature
TFCA	Thin Fibrous Cap Atheromas
THF	Tetrahydrofuran
UME	Ultramicroelectrode
WCA	Water Contact Angle
XPS	X-Ray Photoelectrons Spectroscopy
σ	Stress

Table of content

General introduction	3
Chapter 1	5
Nitinol drug-eluting stents to face coronary artery disease	
Chapter 2	41
Improving Nitinol biomedical properties: aim, strategies & experimental section	
Chapter 3	65
Hydrothermal reinforcement of Nitinol oxide layer: a first barrier against surface corrosion	
Chapter 4	57
Electroassisted functionalization of Nitinol surface, a powerful strategy for polymer coating through controlled radical surface initiation	
Chapter 5	79
Electrografting of organophosphonic mixed monolayer for SI-ATRP of 2-methacryloyloxyethyl phosphorylcholine	
Chapter 6	95
Evaluation Nitinol behavior in physiological conditions: a step toward biomedical applications	
Chapter 7	103
Elaboration of bisphosphonic acids coatings on Nitinol: an alternative to mixed monolayers	
Chapter 8	115
General conclusions & perspectives	
Appendices	121

General introduction

Although the strategies presented in the present work can be used to tune various materials with a broad field of applications, it was mainly elaborated within the context of cardiovascular applications. Indeed, cardiovascular diseases are nowadays the leading cause of mortality worldwide with ~45% of deaths by non-communicable disease, affecting in average 40% of men and 49% of women.

Among the existing solutions to face coronary artery disease, the use of metallic drug eluting stents has been proven to be of interest for the long-term treatment of obstructed vessels. To ensure their efficient deployment and prevent them from recoil, current stents are manufactured using shape memory alloys, such as Nitinol made of nickel and titanium. However, the implementation of such material in the human body can still be hampered by the nickel inclusions present at the surface, making it sensitive to pitting corrosion and leading therefore to the release of carcinogenic Ni^{2+} ions.

The present work is thus devoted to the improvement of NiTi properties through the multi-step elaboration of a biocompatible organic coating on its surface with the purpose of increasing its corrosion resistance, its biocompatibility, as well as its hydrophilicity to prevent the adhesion of fat and proteins on its surface. With this purpose, the discussion has been structured in eight sections.

The **first chapter** briefly introduces the problematic of cardiovascular diseases, the existing medical treatments and their limitations, as well as some key surface modification processes that can be used as a starting point for the successful tuning of Nitinol surface properties.

The **second chapter** focuses on the characterization of Nitinol native oxide composition and its electrochemical behaviour, as well as on the effect of its hydrothermal treatment used as a first surface reinforcement.

The elaboration of a protective and hydrophilic coating is then prepared by electrochemistry and surface-initiated atom transfer radical polymerization. The grafting efficiencies as well as the resulting surface properties are studied in **chapters 4 and 5**. The coating resulting from the optimal modification conditions is then submitted to simulated human blood plasma and to endothelial cells growth to ensure its efficiency in physiological conditions (**chapter 6**).

An alternative monolayer is also studied in **chapter 7**. Such monolayers are prepared with bisphosphonic acid derivatives, and their efficiency is compared to the conventional monophosphonic derivatives.

Chapter 1

Nitinol drug-eluting stents to face coronary artery disease

1.1 Coronary artery disease	7
1.1.1. A worldwide cause of death	7
1.1.2. From plaque inflammation to atherosclerosis	8
1.1.3. Angioplasty: a first step for the treatment of obstructed arteries	10
1.2 Stents	11
1.2.1. From bare metal to drug eluting stent.....	11
1.2.2. Balloon vs self-expanding stent: pros and cons.....	12
1.2.3. Metallic stents or bioresorbable scaffolds?	14
1.3 Nitinol: a promising shape memory alloy	14
1.3.1. Outstanding thermomechanical properties.....	15
1.3.2. A suitable material for biomedical applications?	17
1.3.3. Nickel toxicity and carcinogenesis.....	18
1.3.4. Tackle with alteration of Nitinol: a challenging problem.....	20
1.4 How to improve Nitinol corrosion resistance?	23
1.4.1. Self-assembly of organophosphonic derivatives	24
1.4.2. Elaboration of polymer brushes by SI-ATRP	26
References	28

1.1 Coronary artery disease

1.1.1. A worldwide cause of death

Cardiovascular disease (CVD) is the leading cause of morbidity and mortality worldwide,^{1,2} and in Belgium.³ It includes both diseases of the heart or of the blood vessels (*e.g.* heart attack) and vascular diseases of the brain (*e.g.* stroke).⁴ Among the different types of CVD, many are the consequence of atherosclerosis. It is the case of coronary artery disease (CAD - also known as ischaemic heart disease), cerebrovascular disease, or peripheral vascular disease.^{4,5} Other CVD, such as congenital heart disease, rheumatic heart disease, heart valve disease, or cardiac arrhythmias are less common than CAD, but remains of concern.⁴

CVD is the cause of over 17.3 million (~ 31 %) and 3.9 million (~ 45 %) deaths a year worldwide and in Europe, respectively.^{4,6} Among the CVDs, CAD is the leading cause of mortality with respectively 862 000 and 877 000 deaths (~ 20% of all deaths) for European men and women (Figure 1.1).^{6,7} However, since 1987, cardiovascular mortality have been declining in high-income countries (47% for men and 44% for women in Hainaut)³ thanks to therapeutic progress and especially to primary prevention measures, but have highly increased in low- and middle-income countries.^{4,5,8,9}

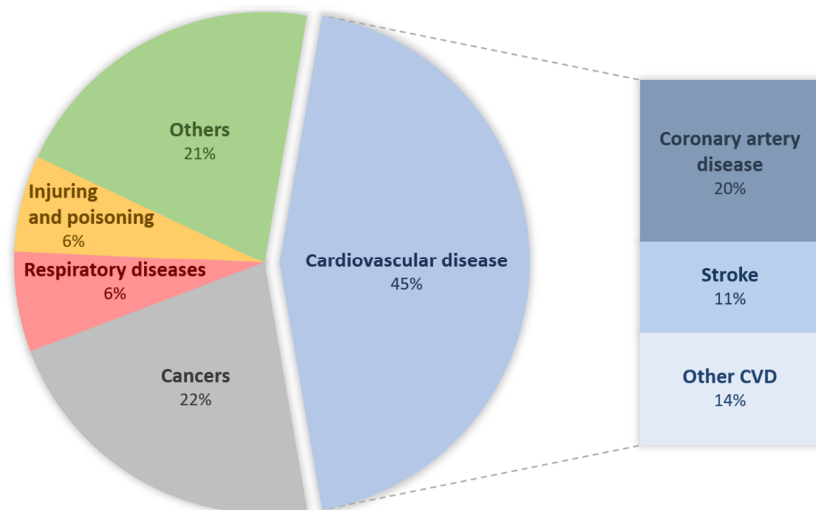


Figure 1.1. Deaths by cause in Europe (based on 2017 European Cardiovascular Disease Statistics and World Health Organization Mortality Database).^{6,7}

The latest statistics about the causes of death in Belgium, European Union and Europe all indicate a prevalence of CAD mortality with respectively 7.5, 12.7 and 19.7 % of all mortality causes (Table 1.1).

Table 1.1. Total number of deaths by cause, latest available year (based on 2017 European Cardiovascular Disease Statistics and World Health Organization Mortality Database).^{6,7}

	All causes	Coronary artery disease	Stroke	Other CVDs
Belgium	109 334	8 227	6 985	16 102
European Union	4 970 751	632 928	426 043	789 503
Europe	8 846 296	1 739 435	988 573	1 212 657

1.1.2. From plaque inflammation to atherosclerosis

Coronary artery disease is mainly due to atherosclerosis. The development of atheroma plaques, particularly thin fibrous cap atheroma (TFCA),¹⁰ in the coronary artery wall induces insufficient oxygen supply to the cardiac muscle. The resulting symptoms vary according to the degree of occlusion of the coronary arteries, ranging from healthy vessel to myocardial infarction or stable angina.^{11,12} This non-linear process presents 7 categories of lesions: (a) intimal thickening; (b) intimal xanthoma; (c) pathological intimal thickening; (d) fibrous cap atheroma; (e) thin fibrous cap atheroma; (f) calcified nodule; and (g) fibrocalcific lesions (Figure 1.2).^{11,13,14}

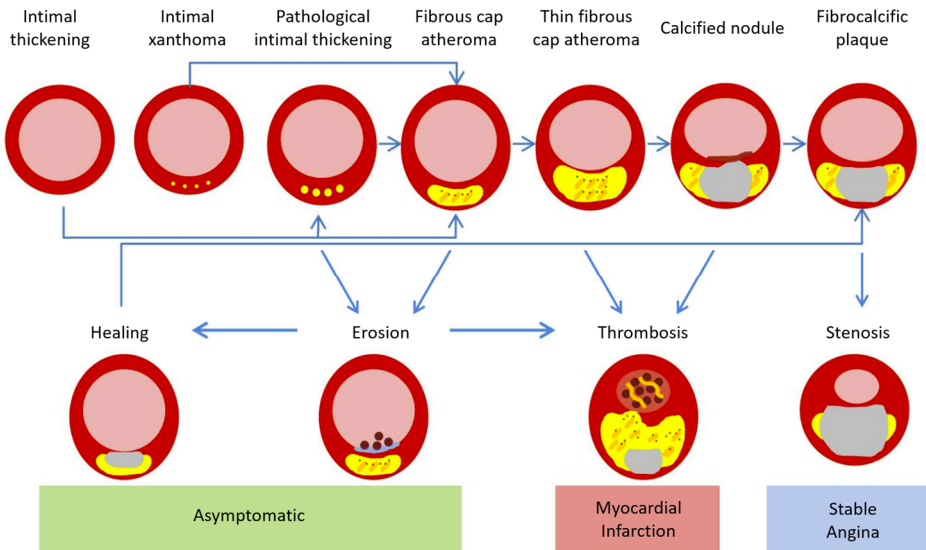


Figure 1.2. Progression of atherosclerotic lesions leading to myocardial infarction or stable angina.¹⁴

The initial phase of lesion formation can start either from intimal thickening or from intimal xanthoma.^{11,13,14} Intimal thickening (type I lesion) is the first described vascular change and consists in accumulation of smooth muscle cells (SMCs) in the intima in absence of lipid and macrophage foam cells. Intimal xanthoma (also known as fatty streak – type II lesion) results from luminal accumulation of foam

cells interspersed within SMCs. This lesion appears without any necrotic core or fibrous cap and has been proven to be a reversible process with the possibility of regression in humans.^{13,15}

The first progressive lesion is known as pathological intimal thickening (type III lesion) and directly results from intimal thickening. This lesion corresponds to aggregation of SMCs in a proteoglycan/collagen matrix, areas of extracellular lipid accumulation without necrosis and accumulation of macrophages on the luminal of the plaque. In case of acellular necrotic core apparition, this lesion evolves into fibrous cap atheroma (type IV lesion). This well-formed necrotic core is made up of cellular debris and is covered by a thick fibrous cap consisting in SMCs in the same proteoglycan/collagen matrix. Pathological intimal thickening and fibrous cap are both the starting point of plaque erosion, *i.e.* an acute thrombus rich in SMCs and proteoglycan matrix in direct contact with the intima, but with no structural defect beyond the endothelial injury. Atherosclerosis erosion can thus lead to either asymptomatic healing or evolve into lumen thrombosis and myocardial infarction.^{11,13,14,16}

Fibrous cap atheroma may evolve into thin fibrous cap atheroma following infiltration of macrophages and lymphocyte inside the lesion. It is mainly made up of type I collagen and is characterized by either an absence of (or only a few) SMCs. Eruptive dense nodular calcification areas may appear within thin fibrous cap atheroma. This phenomenon is generally associated with a narrowing of the lumen. Thin fibrous cap atheroma and calcified nodule can rupture and lead to lesion thrombosis and subsequent myocardial infarction.^{11,13,14}

The final stage of atherosclerosis process, called fibrocalcific plaque, corresponds to the formation of a collagen-rich plaque with large areas of calcification, few inflammatory cells, and a potential necrotic core. Such lesions rarely cause thrombosis, but can cause chronic ischemic symptoms, high stenosis and stable angina due to a further lumen narrowing.^{11,13,14}

However, all these plaques are not necessarily responsible for the symptomatology, as some them can break without causing chest pain, but they remain markers of the severity of atherosclerotic disease in the patient's vascular tree, and thus indirectly risk factors for developing ischemic heart disease.^{11,12} The coronary revascularization treatment is therefore reserved to lesions having a clinical translation (angina or myocardial infarction) and obstructing by more than 70% the luminal diameter of the coronary artery. This treatment is either endovascular or chemurgical depending on the lesion type. In the other many cases, the standard treatment is percutaneous angioplasty which involves restoring a satisfactory coronary diameter, by balloon swelling and/or stent placement, by introducing an arterial guide

(radial or femoral), under fluoroscopy and by means of injection of contrast medium.¹⁷

1.1.3. Angioplasty: a first step for the treatment of obstructed arteries

The first treatment of coronary artery disease was introduced in 1967 by René Favaloro: the aortocoronary bypass first based on the use of a free saphenous vein autograft interposed end-to-end to the transected ends of the artery after its excision (Figure 1.3a), and later to the standard end-to-side interposition (Figure 1.3b). Although it was a noticeable advance in cardiology, this technique required open-heart surgery, and was thus invasive and risky.^{18–20}

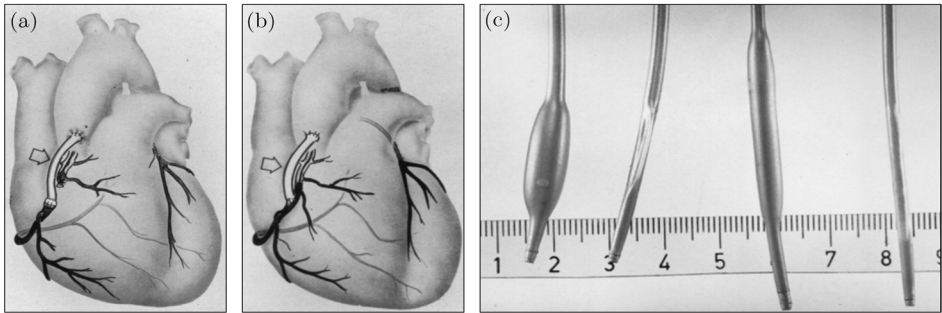


Figure 1.3. First advances in coronary artery disease treatment: end-to-end (a) and end-to-side (b) aortocoronary bypass,¹⁸ and double-lumen catheters assembled by Grüntzig (c) after and before (right) inflation.²⁰

In 1977, Grüntzig tested a revolutionary alternative to the aortocoronary bypass, *i.e.* the first coronary angioplasty based on the peripheral angioplasty performed by Dotter in 1964. Grüntzig procedure relies upon the use of a double-lumen balloon catheter: the first one used for balloon inflation and the second one to measure distal pressure (Figure 1.3c).^{21–23} This technique was the starting point of several improvements in cardiovascular treatments: Simpson *et al.* first included the introduction of over-the-wire technology to support the balloon and helps its guiding in 1982,²⁴ whereas Bonzel *et al.* created exchangeable angioplasty systems which allowed the independent and rapid movement of the guide wire and balloon in 1986.²²

However, coronary balloon dilatation quickly exhibited limitations, *i.e.* arterial dissection due to the inflation and a rapid reocclusion of treated vessels. In this context, Jacques Puel and Ulrich Stigwart simultaneously implanted the first coronary stents in a human in 1986 in France and Switzerland, respectively. Such revolutionary medical procedure, called stenting, relies on the use of a tubular metallic endoprosthesis, *i.e.* a stent, that can be inserted into the lumen of obstructed vessels and arteries to keep them open and prevent from the formation of a new obstruction.²⁵

1.2 Stents

1.2.1. From bare metal to drug eluting stent

Since 1986, the use of coronary bare metal stent (BMS) highly improved the treatment of CAD through a safer, more efficient and surgery-free procedure. Stent implantation present the advantages of sealing dissected tissues/plaques and avoid elastic recoil.^{22,26} However, BMSs have been proven to lead to in-stent restenosis (ISR), myocardial infarction and angina due to SMCs migration and proliferation. Early studies reported a stent thrombosis rate as high as 20% during the six first months of follow-up, with required revascularization.²⁷⁻³⁰

Attempts to improve BMS performances have been achieved through design variations (*e.g.* tubular stents, coil, ring or mesh), thinner struts, use of different materials (*e.g.* cobalt, chromium, platinum, or various alloys), or elaboration of inorganic coatings (*e.g.* silicon carbide or titanium-nitride-oxide).^{22,30} Despite some of these stents exhibit better radio-opacity, deliverability and conformability or even lower rates of restenosis, in-stent thrombosis remains of concern with rate ~ 15% within the 6 months follow-up.³⁰⁻³⁴

To face those problems, research focused on the elaboration of a stent as a platform for antiproliferative drug delivery to prevent ISR, called drug-eluting stent (DES).²³ These consist in a metallic stent platform covered by a polymer coating in which is inserted a drug, generally an antiproliferative (*e.g.* Sirolimus or Paclitaxel) or immunosuppressive agent to prevent the accumulation of anti-inflammatory cells, the neointima hyperplasia and the thrombus formation.^{23,26} However, despite they were reported to have low rates ISR and to improve vessel revascularization, the first-generation DES, based on a stainless steel platform, were also proven to increase rates of myocardial infarction and cardiac death caused by late-stent thrombosis (LST) during long-term follow-up.³⁵⁻³⁸

Next-generation DES were developed to overcome the problem of LST by accelerating vessel healing, and presented several improvement compared to DES, *e.g.* strut thickness, deliverability and flexibility.³⁹ These DESs also used new polymer coatings as well as new drugs derived from the previously used sirolimus, including everolimus and zotarolimus (Figure 1.4). Such molecules are used to cause cell-cycle arrest of proliferating SMCs.^{22,23,26,40}

In this context different stents (design and or material), polymers and drugs are currently being investigated to reduce the risk of ISR and major adverse cardiac events mainly due to stent malapposition and to the struts thickness.⁴¹ Many progress still have to be done, and the improvement of DES for the treatment of cardiovascular disease remains of concern.

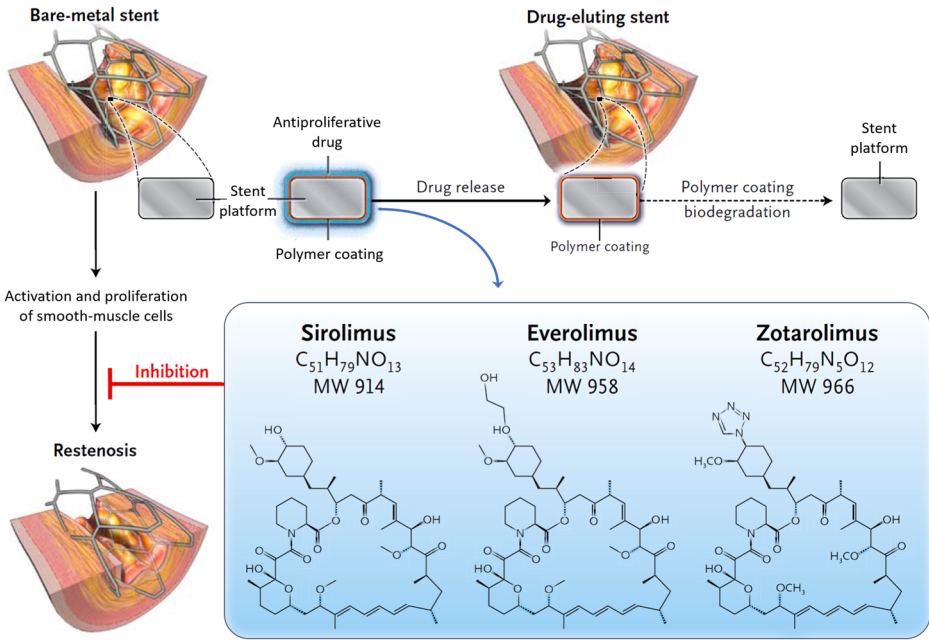


Figure 1.4. Schematic representation of drug-eluting stents mode of action for the inhibition of restenosis (adapted from Stefanini *et al.*).²⁶

1.2.2. Balloon vs self-expanding stent: pros and cons

Depending on how the deployment is effected and on the mechanical properties, there are two main types of stents: balloon-expandable stents (BES), mounted on a balloon angioplasty catheter that is inflated for its deployment, or self-expanding stent (SES) stents, constrained by a sheath that is progressively removed after the device delivery (Figure 1.5).^{17,22,42}

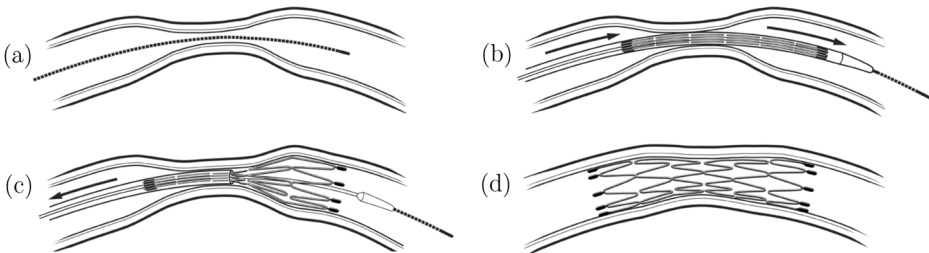


Figure 1.5. Steps involved in self-expanding stent deployment: insertion of a steerable wire (a), delivery of the undeployed stent (b), distal deployment of the stent (c), and ideal apposition (d).⁴³

Developed and used by Sigwart *et al.* in 1986,²⁵ SES were first outclassed by BES in the field of coronary artery diseases due to its slightly worse apposition precision, but they nevertheless used nowadays for myocardial infarction as they

recently showed a lower rate of strut malapposition than SES at 3 days after percutaneous coronary intervention.^{42,44}

SES and BES differ in many respects, as summarized in Table 1.1. The main difference comes from the fact that SES becomes part of the anatomy and act in harmony with the vessels whereas BES imply changes of their geometry.⁴²

Table 1.2. Comparison of balloon- and self-expanding stents (based on Duerig *et al.*).⁴²

	Balloon-expandable	Self-expanding
<u>Manufacturing</u>	Manufactured in the crimped state	Manufactured slightly over the vessel diameter
<u>Delivery</u>	Expanded to the vessel diameter by inflating a balloon (\Rightarrow Plastic deformation)	Crimped to a smaller diameter and deployment by constraint removal
<u>Use</u>	Dominant in the much larger coronary arena	Suited to superficial locations (<i>e.g.</i> carotid and femoral arteries)
<u>Radial strength</u>	\equiv describes the external pressure that a stent is able to withstand without incurring clinically significant damage Can collapse under a critical external pressure	No strength limitation and elastically recover
<u>Radial stiffness</u>	\equiv how much the diameter of a stent is reduced by the application of external pressure (<i>neither an advantage nor a disadvantage</i>) Stiffer (up to 3x) for identical stent design. \Rightarrow Force the vessel to the shape of the stent	Low stiffness and high radial compliance \Rightarrow Adapt their shape to that of the vessel
<u>Acute recoil</u>	\equiv immediate reduction in diameter observed upon deflation of a balloon Recoils after balloon deflation	Assist balloon inflation and no recoil
<u>Hyperplasia</u>	Indicative of a constriction of the vessel	Not necessarily indicative of a problem
<u>Location</u>	Remain near the lumen	Scaffold the vessel wall
<u>Delivery</u>	Dictated by the balloon profile	Dictated by the strut dimensions
<u>Placement accuracy</u>	The “gold standard” for placement accuracy	Nearly as accurate as BX systems
<u>Direct stenting</u>	No pre-dilation of the vessel required	Pre- or post-dilatation of calcified lesions required

1.2.3. Metallic stents or bioresorbable scaffolds?

The latest development in the stent world relies on the use of bioresorbable scaffolds (BRS) that are designed to replace permanent rigid metal material in the diseased vessel by providing transient mechanical support, followed by complete biodegradation over several years. The concept of BRS was developed over the last decade and trials are still required to assess their long-term clinical benefits. The expected advantages of BRS *vs.* permanent DES include restoration of vessel anatomy/functionality, reduction of thrombogenic risk, and potential elimination reduction of in-scaffold neoatherosclerosis risk.^{23,30,45} These devices are made out of a polymeric (*e.g.* polylactic acid or salicylic acid)⁴⁶⁻⁴⁹ or metallic (*e.g.* magnesium or zinc-alloys)⁵⁰⁻⁵³ degradable base. So far, only five BRS have received the Conformité Européenne (CE) approval mark, and only one is approved in the USA by the Food and Drug Administration (FDA).^{22,23,30}

Despite they were reported to have non-inferiority results to DES at one-year follow-up compared, concerns regarding early-scaffold thrombosis, higher subacute thrombosis and risks of myocardial infarction merged among BRS. The underlying causes are not fully known yet, but several are suspected: (a) malapposition and scaffold discontinuity; (b) unfavourable bioresorption ; (c) lower radial strength and required thicker/wider struts (up to 165 μm compared to $\sim 80\text{-}90 \mu\text{m}$); (d) device underexpansion or (e) loss of scaffold integrity during the late resorption phase.^{22,54-56}

Although promising, the use of BRS has raised some concerns on the rate of scaffold-thrombosis and their long-term efficiency and clinical outcomes are still to be investigated and compared to DES. Advancements are still required to further improve BRS post-apposition behaviour, and metallic DES remains the current high standard for the treatment of coronary artery disease.^{22,23} Among the currently used materials, nitinol appears to be the most promising combination of DES and SES, and is already commercialized by many international companies such as Stentys (France),⁵⁷ Boston Scientific (BENELUX),⁵⁸ Cordis (Switzerland),⁵⁹ medicut (Germany)⁶⁰ or Norman Noble (USA).⁶¹

1.3 Nitinol: a promising shape memory alloy

Nitinol (NiTi) is a nearly equiatomic nickel titanium alloy made of nickel and titanium which have been intensively investigated since its discovery by Buehler in the early 1960s at the **N**aval **O**rdnance **L**aboratory.⁶² The explosive interest for NiTi at the beginning of the century arises from its outstanding properties. Indeed, this nearly equiatomic alloy composed of nickel and titanium, presents highly desirable

intrinsic properties including heat, impact and corrosion resistance, high fatigue strength, super-elasticity close to that of bone⁶³ and shape memory.^{64–68}

1.3.1. Outstanding thermomechanical properties

The thermomechanical properties of Nitinol rely on a reversible solid-state phase transformation between two temperature dependent stable crystal phases. At low temperatures (*i.e.* below the transition temperature), Nitinol assumes a monoclinic B19' structure (martensite - Figure 1.6a), whereas at high temperature (*i.e.* above the transition temperature), it assumes a centred cubic B2 crystal lattice (austenite - Figure 1.6b).

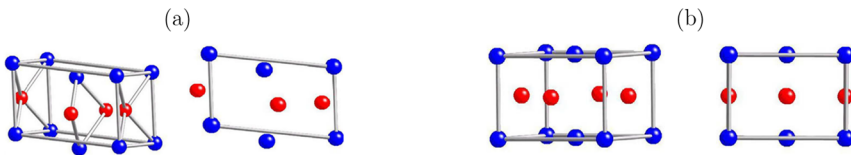


Figure 1.6. Representation of stable crystallographic structures of NiTi (blue = Ti, red = Ni): martensite (a) and austenite (b).⁶⁹

The reversible transformation between those phases, known as martensitic transformation, is done via an instantaneous cooperative movement of the atoms over short distances and without diffusion phenomenon,⁷⁰ and is characterized by four transition temperatures: the martensite and austenite start/finish temperatures (M_s/M_f and A_s/A_f , respectively).^{66,70} In most compositions, A_s temperature value is comprised between 25°C and 30°C. The phase transformation between those temperatures during a stress is done following a hysteresis behaviour (Figure 1.7) and is dependent on the composition and/or the processing of the material.

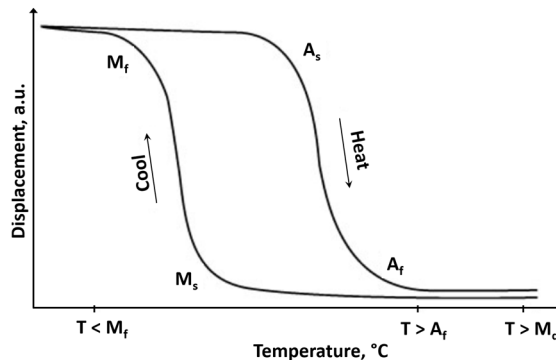


Figure 1.7. Schematic displacement–temperature curve under constant tensile force for Nitinol (adapted from Robertson *et al.*).⁷¹

The structures involved in the martensitic transformation thus lead to particular properties in the material, such as pseudoplasticity, superelasticity or even shape memory (that is, the ability to return to its original shape after deformation,

if the material is subjected to suitable thermomechanical conditions).^{72,73} Nitinol can thus exhibit different mechanical behaviours depending of the temperature (*i.e.* $T < M_f$, $T > A_f$, and $T > M_d$) (Figure 1.8). Below M_f (Figure 1.8a), the material exhibits its martensite structure and can undergo a limited deformation. The so-formed deformation is not fully recovered when the stress is removed.

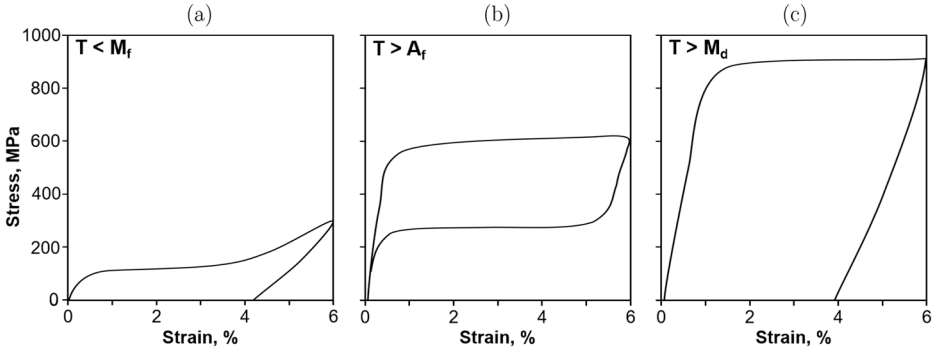


Figure 1.8. Stress-strain curves at different temperatures: below M_f (a), above A_f (b), and above M_d (c).⁷¹

This deformation, although of plastic appearance, can nevertheless be reversible at higher temperature (**pseudoplasticity**): during a rise in temperature, the stability between the crystalline phases of the inverse Nitinol, and the material exhibits its austenite phase. The strain begins to recover upon heating the deformed martensite above A_s with a complete shape recovery of the strain at A_f (Figure 1.9a). The transition from M_s to M_f or A_s to A_f is characterized by a two-phase mixture of austenite and martensite (Figure 1.9b).

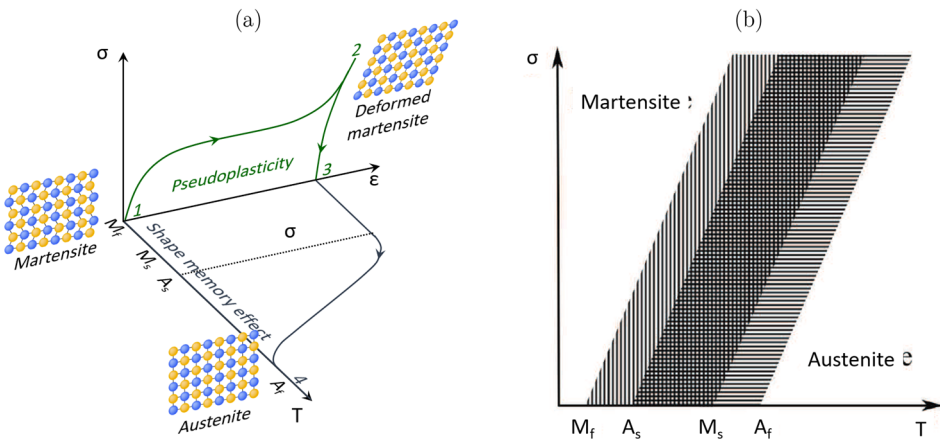


Figure 1.9. Schematic representation of the effects of pseudoplasticity (a/1-3) and shape memory (a/1-4) of Nitinol (adapted from Follador M. *et al.*⁷³ and Branco M. *et al.*⁷⁴), and martensite/austenite stability domains as function of the temperature T and of the stress σ (b).⁶⁶

If a similar stress is applied above A_f (Figure 1.8b), the material exhibits superelastic properties, *i.e.* the stress induced transformation is followed by a strain recovery upon removal of the applied stress due to the concomitant transformation back to the austenite phase. However, upon the critical value of M_d (Figure 1.18c), Nitinol deforms following a plastic behaviour and no more martensitic transformation is involved.⁷¹

In addition, Nitinol also exhibits a closer similarity to biological tissue mechanical response than other metals such as steels (Figure 1.10): the material undergoes a linear deformation proportionally to the applied stress, followed by a plateau and especially a return to a state close to the initial one upon the release of the strain whereas for conventional materials with limited elasticity the deformation is and irreversible.^{63,75}

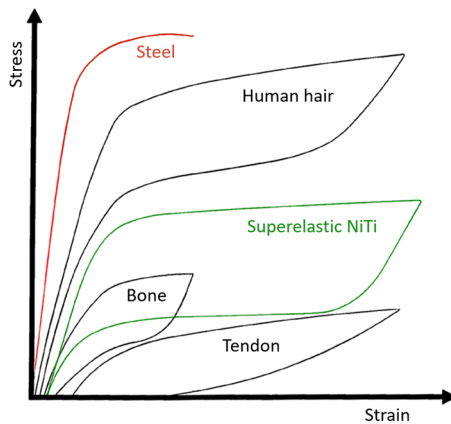


Figure 1.10. Stress-strain diagram of stainless steel and Nitinol compared to human bones, hair and tendon.⁷⁶

1.3.2. A suitable material for biomedical applications?

As a consequence of those properties, NiTi turned to be an “household” word in the biomedical field into which it is used in a wide range of applications such as self-expanding stents, drills, surgical endoscopic instruments, tubing, atrial septal occlusion devices, orthodontic wires, orthopaedic staples and plates.^{77–80}

Nitinol corrosion resistance mainly results from the presence of a stable native TiO_2 passivating top-layer in most environments and thermodynamically stable in a large pH range, as illustrated by titanium-water potential-pH diagram (Figure 1.11a).^{81,82}

TiO_2 oxide layer is thus an efficient barrier against dissolution and reduce the release of toxic Ni^{2+} ions.^{81,82} However, this layer is very thin, and Nitinol presents

also several nickel inclusions making it sensitive to pitting corrosion,⁸³⁻⁸⁵ an issue to take into consideration as the Ni^{2+} ions potentially formed during corrosion in some conditions (Figure 1.11b) may lead to allergenic or inflammatory reactions, breathing problems or even various cancers (such as lung, kidney or liver).⁸⁶⁻⁸⁸

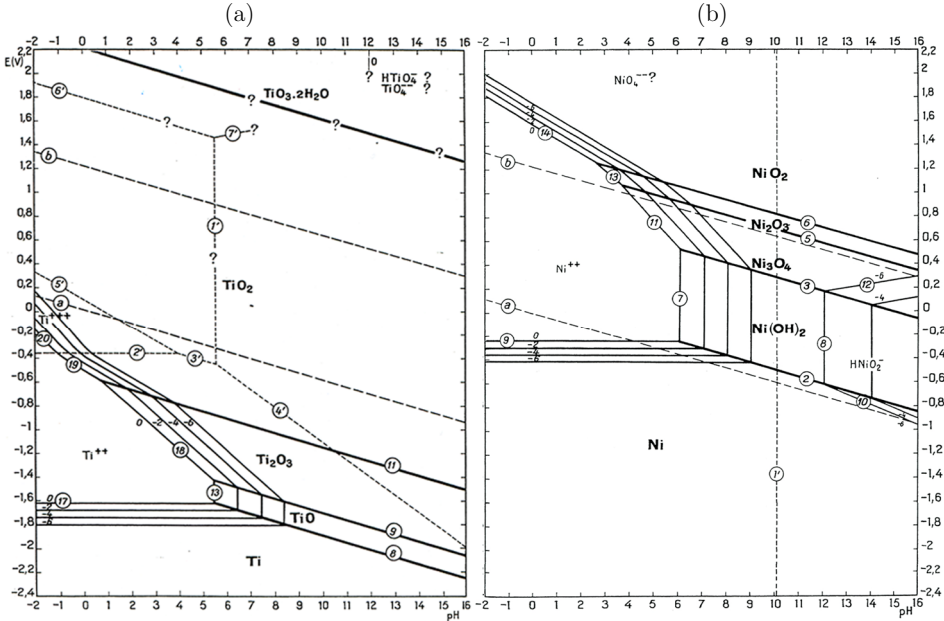


Figure 1.11. Potential-pH diagram for the systems titanium/water (a) and nickel/water (b) at 25°C.⁸⁹

However, this protective film may not be efficient enough if exposed to a highly corrosive environment, where corrosion may induce the release of Ni^{2+} .⁹⁰ Numerous studies on the exposure of treated Nitinol (with reinforced oxide layer) in biological media such as saliva or blood have shown that the main corrosion residues are TiO_2 , and that Ni^{2+} concentrations are too low to affect the body.⁹¹ Nevertheless, those effects have not yet been precisely determined and Nitinol biocompatibility is still controversial today and NiTi devices still need to be treated to enhance its surface protection and implant-safe conditions.⁹⁰⁻⁹²

1.3.3. Nickel toxicity and carcinogenesis

As mentioned previously, nickel and its compounds are known to have toxic and carcinogen effects on the human body. Even if those effects are not completely clear nowadays, nickel adverse effects are mainly due to: (a) the alteration of core histone and subsequent silencing of cell cycle control genes; (b) the substitution of metallic ions in metal-enzyme complexes; (3) the inhibition of enzymes and Ca^{2+} channels; but most of all (4) to genetic/epigenetic alterations of DNA; and (5) the induction of oxidative stress.⁹³⁻⁹⁹

1.3.3.1. Genetic and epigenetic alterations

Nickel exposure can lead to genetic and epigenetic alteration that lead to carcinogenesis. On one hand, the most common genetic modifications are: (a) chromosomal aberrations that affect the copy number of genes and alter genetic loci; and (b) DNA damage and subsequent gene mutation that can promote carcinogenesis. On the other hand, epigenetic modifications mainly relies on: (a) microRNA alteration - repression of tumor-suppressing microRNAs and overexpression of oncogenic microRNAs; (b) histone alteration by acetylation and methylation hypomethylation is a hallmark trait of cancer cells; and (c) DNA methylation – hypermethylation in the promoter region turns off tumor-suppressor genes whereas DNA hypomethylation is a hallmark trait of cancer cells.^{99,100}

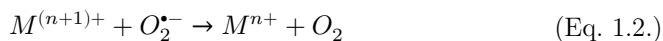
1.3.3.2. Oxidative stress

Nickel compounds are known to cause DNA damage through the promotion of oxidative stress and the generation of reactive oxygen species (ROS, *e.g.* OH^\bullet , $O_2^{\bullet-}$ or H_2O_2). At low level, ROS act as signalling molecules in many physiological processes, and are rapidly removed from to body by defence mechanisms. However, at high levels, ROS can lead to DNA, protein and/or enzyme damages, thus leading to deregulation of metabolic and signalling pathways, to damages in diverse cell locations or even to potential cyto- and genotoxic effects.^{86,95,96,100} Among the mechanisms of metal-mediated free radical generation, those radicals are mostly generated via Fenton-type and Haber-Weiss-type reactions.

In the Fenton-type reaction, the ionized transition metal is oxidized by surrounding H_2O_2 molecules (produced, for instance, by the peroxisomes) to generate OH^\bullet radicals (Eq. 1.1.).^{95,96}



In the Haber-Weiss-type reaction, the oxidized metal ions are reduced by superoxide molecules (Eq. 1.1.). Those molecules result either from the consumption of oxygen by phagocytes or are produced by several oxidases. The so-formed oxidized metal ions can then undergo a Fenton-type reaction and produce more OH^\bullet radicals.^{95,97}



In addition, OH^\bullet radicals can also result from the complexation of Ni^{2+} ions with various proteins. The so-formed complex is followed by their deregulation, thus altering their ability to reduce H_2O_2 .^{94,98}

1.3.4. Tackle with alteration of Nitinol: a challenging problem

Even with the presence of a passivation layer, its breakdown can result in localized forms of corrosion in presence of specific aggressive species and thus lead to various amount of metal degradation. Such corrosion process (Figure 1.12) is composed of at least two partial reactions:¹⁰¹

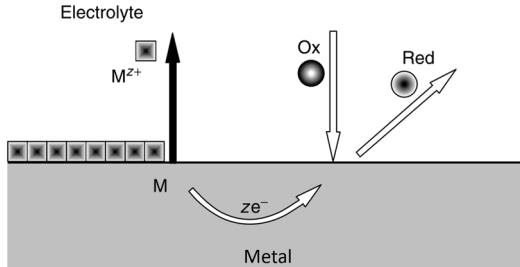


Figure 1.12. Schematic representation of corrosion process at the metal-electrolyte interface.¹⁰¹

(a) Anodic dissolution of the metal (mainly nickel):



(b) Reduction of the oxidizing agent



The reduction reaction highly depends on the presence of oxidizing species and from the pH. In neutral aerobic media, such as blood plasma, (Eq. 1.4.) thus becomes:



In biomedical applications, the corrosion is not only influenced by (electro)chemical processes, but also by mechanical ones. Different corrosion modes are possible (Figure 1.13), *e.g.* for NiTi biomedical applications: (a) uniform corrosion; (b) pitting corrosion; (c) crevice corrosion; (d) erosion corrosion; and (e) fretting corrosion.^{82,102}

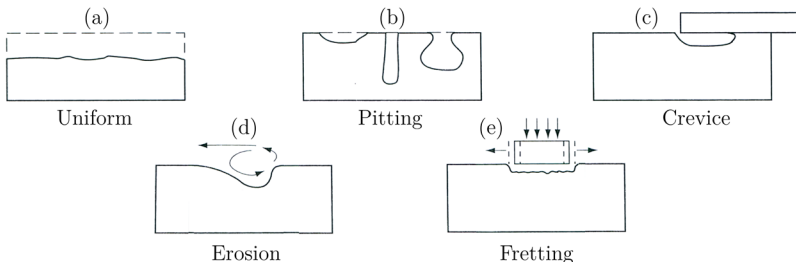


Figure 1.13. Schematic representation of different forms of corrosion (adapted from D.A. Jones).¹⁰²

1.3.4.1. Uniform corrosion

Uniform corrosion happens if the metal presents a homogeneous composition. The corrosive environment can thus equally access all parts of the metal surface, and the dissolution and reduction reactions thus evenly distributed on the surface and present similar kinetics (Figure 1.14). The distance between those reaction spots is infinitesimally short, and the locations of both reactions continuously and randomly shift across the surface.

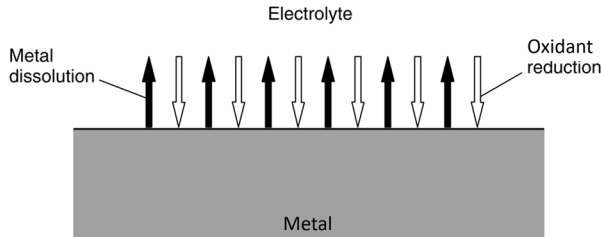


Figure 1.14. Schematic representation of uniform corrosion.¹⁰¹

Uniform corrosion is the most encountered, predictable and less damaging case. However, local regions of corrosion usually appear and lead to localized failure of the passivating layer (*e.g.* pitting or crevice corrosions).^{77,101–104}

1.3.4.2. Pitting corrosion

Pitting corrosion results from localized breakdown of the material due to surface heterogeneities, second-phase inclusions and/or impurities. It is characterized by a large ratio of the cathode area (in contact with the electrolyte) to anode area (occluded region), thus increasing the corrosion rate in those regions. Most alloys are susceptible of pitting corrosion, *e.g.* stainless steels, iron-base, nickel-base, aluminium-base, and titanium-base alloys. In presence of a very protective passive layer, pits are usually initiated at pre-existing surface defects or as a consequence of local damages. Once initiated (Figure 1.15a), pits can either repassivate if the occluded region is cleared from corrosion products (Figure 1.15b), or grow within various shapes (Figure 1.15c-f) depending on initiation/propagation mechanisms.^{82,102,104}

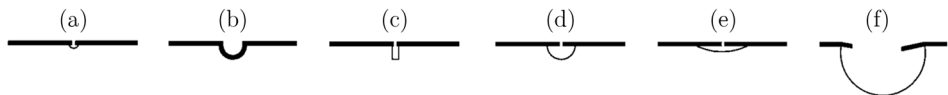


Figure 1.15. Schematic representation of shapes of pit evolution: (a) initiation, (b) repassivation or (c-f) growth/propagation.¹⁰⁴

All halides and some other anions are known to act aggressively against passivated metals.¹⁰⁵ In the particular case of biomedical applications, the material is exposed to physiological medium containing corrosive Cl^- ions which are known to lead to high passivity breakdown. However, NiTi has been reported to have a good

corrosion resistance in such media as TiO_2 is only susceptible of breakdown under high anodic potentials that are practically never encountered.^{82,103} However, if a breakdown occur on the passivating oxide layer, its repassivation is known to be slow and difficult.^{77,102-104}

1.3.4.3. Crevice corrosion

Crevice corrosion occurs between metallic surfaces with very narrow interstices (typically smaller than 100 μm) where mass transport is limited, thus increasing the concentration in aggressive species that can lead to the breakdown of the surface (e.g. overlapping metals, joints, inert deposits, or poorly adhering coatings). This corrosion is governed by the crevice geometry, *i.e.* its width and/or depth.^{82,106,107}

Once the metal is exposed to the environment, the metallic ions concentration will increase close to the surface whereas the oxygen concentration will progressively decrease, especially in the crevice. At early stages, the OH^- ions can counter the lowering in pH resulting from the metal ions release, and the subsequent hydrolysis of the metal-chloride salts (Figure 1.16a). After the oxygen from the occluded area is consumed, the metal continually dissolves in the crevice, thus accumulating metal ions and decreasing the local pH by hydrolysis (Figure 1.16b). At sufficiency low pH, the passivating layer is destroyed, and the corrosion can propagate into the metal.^{106,107}

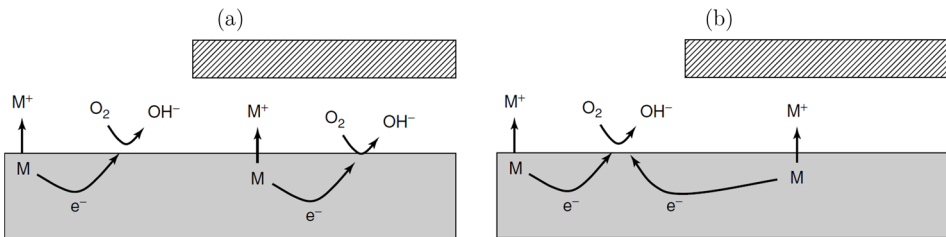


Figure 1.16. Schematic representation of crevice corrosion at early (a) and advanced (b) stage.¹⁰⁶

Nitinol is known to be highly susceptible to crevice corrosion in chloride containing environments such as physiological media. Furthermore, Trepanier *et al.* also proved that Nitinol stents are even more susceptible to this mode of corrosion due to the overlapping of its wires.^{103,108}

1.3.4.4. Erosion-corrosion

Erosion is a concern in a high flow fluid that can physically damage the passivating layer, expose the underlying metal and accelerate its corrosion.¹⁰² When the flowing substances are chemically inert, erosion is a pure mechanical process,

whereas in the case of corrosive substances, such as blood plasma, a conjoint erosion-corrosion process occur (it is generally difficult to determine the contribution of erosion and corrosion separately).^{109,110}

Mechanism of erosion-corrosion depends on: (1) flow velocity and geometry; (2) environmental conditions such as pH or presence of oxygen; and (3) the nature of the metal/alloy, *i.e.* its chemical composition, its hardness, the presence of passivating layer, *etc.*¹⁰⁹

Among various alloying elements, nickel and titanium are known to form a tighter structure once alloyed, thus improving the material corrosion resistance.¹⁰²

1.3.4.5. Fretting corrosion

Fretting corrosion is provided by repeated vibrating and load movements between two materials in contact. This motion abrades the material surface, thus exposing the underlying metal and forming oxide debris that can increase the abrasive phenomenon.^{102,109} Fretting corrosion phenomenon can be decreased by: (1) using appropriate lubricant; (2) increasing the hardness of the material; (3) preventing from the loads movements; or (4) using a combination of materials that are less susceptible to slipping movements.¹⁰⁹

In the case of *in vivo* stents, Nitinol passivating layer can be damaged by fretting corrosion resulting from rubbing phenomenon, and even though subsequent repassivation of the surface occurs, the regeneration of TiO₂ layer in *in vivo* media is slow and corrosion products may be found in some adjacent tissues.^{82,103,108,111} In 2006, Trepanier *et al.* demonstrated the impact of fretting corrosion on overlapped NiTi struts in physiological media, and noted a decrease of about 300 mV in pitting potential.^{103,108}

1.4 How to improve Nitinol corrosion resistance?

In recent years, a great attention has been paid to improve Nitinol corrosion resistance by surface modification processes such as plasma treatment,¹¹²⁻¹¹⁴ chemical vapor deposition,^{115,116} hydrothermal reinforcement of the oxide layer,^{117,118} using organic self-assembled monolayers (SAMs)¹¹⁹⁻¹²¹ and surface initiation of polymers.^{118,122,123} Combining these last two options is very attractive to modify interfacial properties of metals and metal alloys such as Nitinol. Indeed, the highly ordered molecular assemblies of SAMs confer a reinforcement of the metal surface corrosion resistance as well as facilitate the introduction of initiating polymerization groups, while the polymer coating will bring new functionalities and physico-chemical surface properties (*i.e.* wettability, protein adsorption resistance, increase of the biocompatibility and/or of the bioactivity).

1.4.1. Self-assembly of organophosphonic derivatives

Over the last decades, many groups have reported the self-assembled monolayers (SAMs) preparation on metals (*e.g.* gold,^{124–128} steel,^{129,130} titanium,^{128,131–133} nickel,^{133–135} iron,^{136,137} or aluminium^{138–140}) and alloy (*e.g.* Phynox,¹⁴¹ Nitinol,^{118–121} or some aluminium alloys^{142–144}) surfaces through a classical approach consisting in immersing the metal into a reactive solution of surfactants in order to form an homogenous organic coating.

SAMs are thermodynamically favoured ordered arrangement (“self-assembled”) of organic molecules on the surface of inorganic or inorganic solid, with a thickness of one molecule (“monolayers”). Organic molecules used in this purpose comprise: (a) an anchoring group, with characteristic affinity to the surface; (b) a spacer (typically an alkane chain) which plays a stabilizing role thanks to intermolecular interactions; and most of the time (c) a tail group which can include a chemical reactive moiety for post-functionalization purpose.^{145–147}

Depending on its nature, various organic modifiers can be used to derivatize a solid substrates, including: (a) thiols – commonly used for the modification of noble metals, and proven to be less effective in modifying metal oxides;^{148–150} (b) silanes – efficient in the modification of oxides, but sensitive to moisture and to self-condensation into Si-O-Si bonds thus leading to multilayers;^{150–152} (c) carboxylic acids – suitable for oxides derivatization, but weak bonding to the surface;^{150,153,154} and (d) phosphonic acid – less prone to self-condensation (Figure 1.17).^{145,146,150,155}

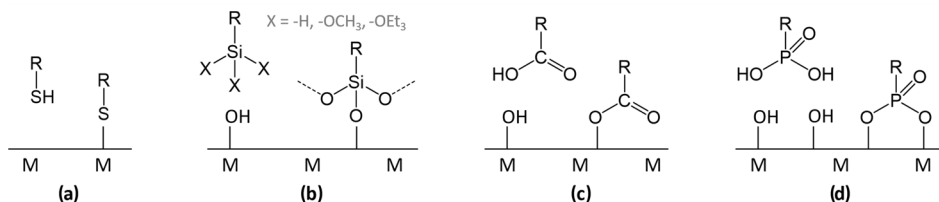


Figure 1.17. Schematic representation of common anchoring group used for the preparation of self-assembled monolayers: (a) thiol, (b) silane, (c) carboxylic acid, and (d) phosphonic acid derivatives.

Among the various useable surfactants, phosphonic acid derivatives have been shown to robustly graft on metal oxide surfaces through hydrolysis resistant M-O-P bonds.^{128,131,156–158} Organophosphorus derivatives contain a tetracoordinate phosphorous atom bound to a double-bonded oxygen and two hydroxyl groups (Figure 1.17d) and are thus able to bind to an oxide surface in a mono-, bi- or tridentate fashion with potential additional hydrogen bonds. In addition to the number of formed M-O-P bonds, phosphonic acids can graft in either a bridging (each oxygen binds to a different metal atom), or chelating (two or three oxygen bound the same

metal atom) way (Figure 1.18). However, it is still difficult to identify the preferential binding modes among all those possibilities nowadays.^{146,155,159}

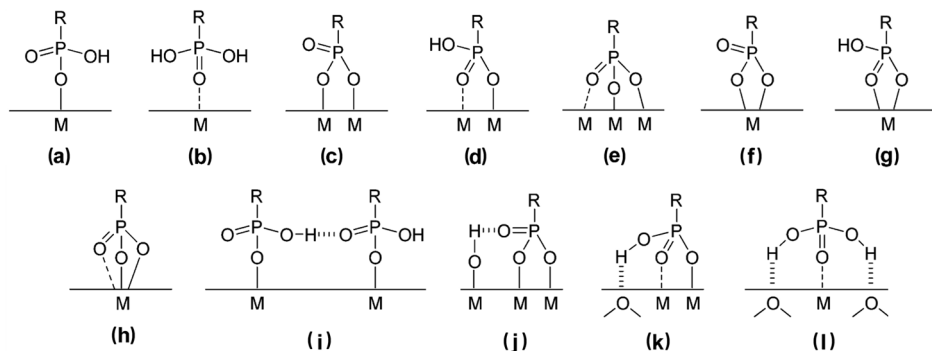


Figure 1.18. Possible binding modes of phosphonic acid to a metal oxide surface: (a and b) monodentate, (c-d) bridging bidentate, (e) bridging tridentate, (f-g) chelating bidentate, (h) chelating tridentate, and (i-l) possible additional hydrogen bonding interactions.¹⁵⁵

Phosphonic-made SAMs can be formed in two ways depending on the Lewis acidic nature of the substrate. In the case of Lewis acidic oxides (Figure 1.19a-d), the grafting occurs by coordination of the phosphoryl group to a Lewis acidic site (which increase its electrophilicity), followed by a heterocondensation reaction(s) with surrounding hydroxyl group(s), thus leading to bi- and tridentate structures. In the case of weak Lewis acidic oxides (Figure 1.19e-h), heterocondensation takes place without any coordination between the phosphoryl group and the surface.^{146,155,160}

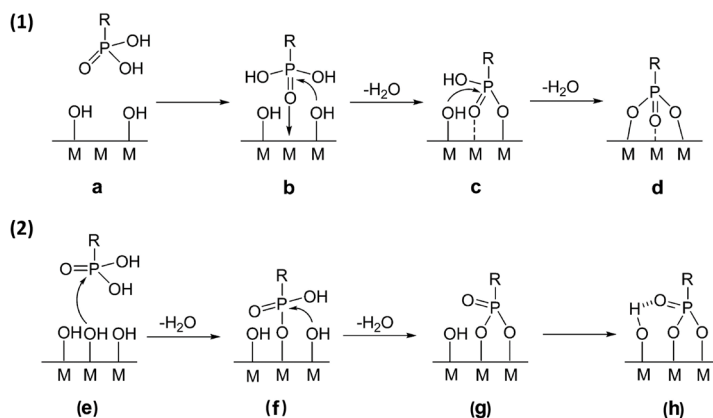


Figure 1.19. (1) Mechanism of phosphonic acid attachment to Lewis acid metal oxides: (a) initial stage, (b) coordination of the phosphoryl oxygen to a surface Lewis acid site and heterocondensation, (c) additional heterocondensation, and (d) tridentate binding state. (2) Mechanism of phosphonic acid attachment to poorly Lewis acid metal oxides: (e) heterocondensation with a hydroxyl group, (f) second heterocondensation, (g) bidentate binding state, and (h) additional hydrogen bonding.¹⁵⁵

Over the last decade, the elaboration of organophosphorus SAMs have been intensively investigated on derivatives differing in length, *e.g.* octadecyl-, decyl-, dodecyl-, or hexadecylphosphonic acids,^{120,122,161–163} as well as in the nature of their tail group, *e.g.* a carboxylic group or an amine.^{122,164,165}

The elaboration of SAMs is a very convenient approach to introduce initiating functionalities with the purpose of promoting polymerization from the metal surfaces. The functionalization of Nitinol with polymerization initiating species will be further discussed in chapter 4 and 5.

1.4.2. Elaboration of polymer brushes by SI-ATRP

Controlled radical polymerization (CRP), introduced by Szwarc in 1956,¹⁶⁶ is a versatile method based on a dynamic equilibrium between growing radicals and dormant species that is commonly exploited for the preparation of well-defined polymers with potentially complex architectures, precise control of molecular weight (MW) and molecular weight distribution (MWD), polymer composition, and functionality. Unlike in classical radical polymerizations, a steady-state low concentration in radicals is established by balancing the rates of activation and deactivation, thus decreasing the amount of reactive species in the solution and preventing irreversible chain termination reactions.^{167,168}

1.4.2.1. Why controlled radical polymerization?

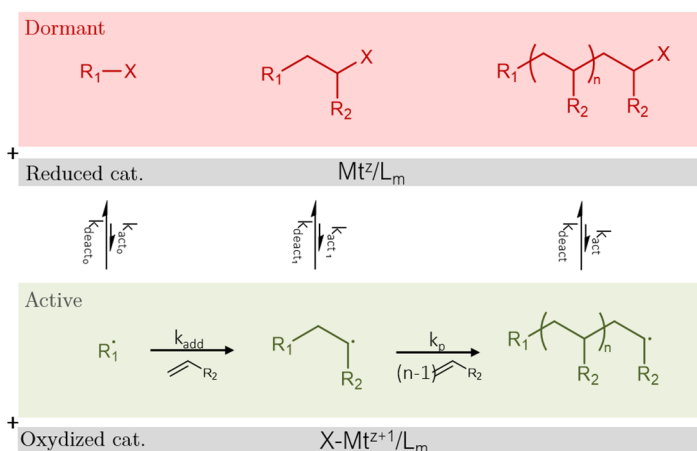
Even if both CRP and classical radical polymerization (RP) are based on similar radical mechanism and can be applied to similar kind of monomers, they still present several important differences. In 2007, Braunecker and Matyjaszewski described those differences and their impact on the polymerization process:¹⁶⁹ (1) The participation of dormant species in CRP extend the lifetime of growing chains from around 1s in RP to more than 1h. However, the polymerization rate is often slower in CRP; (2) Radical initiation is faster in CRP than in RP, which lead to instantaneous growth of all chains; (3) In CRP, the proportion of dead chains is lower than 10% instead of 100% in RP; and (4) In RP, termination reactions usually occur between long chains and generate new chains, whereas in CRP all chains growth simultaneously and termination rate decrease with time. Together, those features make CRP a valuable tool for the design and elaboration of complex polymeric architectures.

1.4.2.2. ATRP: mechanism & features

Among the most famous CRPs, atom transfer radical polymerization (ATRP) is an attractive process developed in 1995 simultaneously by Matyjaszewski¹⁷⁰ and Sawamoto¹⁷¹. It is commonly used worldwide due to the simple experimental setup,

its application to a broad range of monomers and solvents, and the commercial availability of initiators and catalysts. It is especially used for the preparation polymer coatings in the purpose of biomedical applications.^{167,172–174}

Mechanistically, ATRP is based on a reversible halogen transfer from a dormant specie (R_1-X) to a ligand-stabilized transition metal complex (Mt^z/L_m). The polymerization thus results from the homolytic cleavage of the alkyl-halogen bond and to formation of propagating radicals (R_1^\bullet) through the oxidation of the metal complex ($X-Mt^{z+1}/L_m$) (Scheme 1.1). The so formed radicals can initiate the polymerization by addition to the double bond of monomers or react with the oxidized metal complex to regenerate its dormant form. After the addition of a few monomers, the growing radical reacts reversibly with the oxidized metal complexes to re-form the corresponding dormant species and regenerate the activating complex, completing the catalytic cycle.^{167,168,174}



Scheme 1.1. General mechanism of ATRP (based on Matyjaszewski *et al.*¹⁶⁷).

1.4.2.3. Surface initiated ATRP: a grafting from approach

The elaboration of polymer films on materials can be achieved following “grafting from”, “grafting-onto” or “grafting-through” approaches (Figure 1.20).

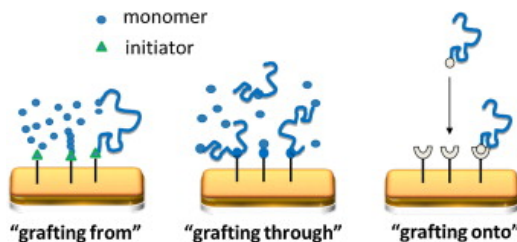


Figure 1.20. Schematic representation of the elaboration of polymer coatings on surfaces following “grafting from”, “grafting through” and “grafting onto” approaches.¹⁷⁵

In the “grafting-onto” approach, the polymer is grafted to the surface of the material whereas in the “grafting from” and “grafting-through” approaches, the polymerization is performed directly onto the material after its surface functionalization by the initiator, or a monomer unit, respectively.^{168,175}

The grafting from approach includes surface initiated ATRP (SI-ATRP - Figure 1.21) which is widely used to graft polymer from various substrates geometries (flat surfaces, nanoparticles, etc) and compositions (metals, alloys, oxides, polymers, etc) and form polymeric brushes. The efficiency of SI-ATRP relies on the uniform presence of polymerization on the surface, either as an inherent part of the material, or via an additional surface functionalization reaction (*e.g.* self-assembled monolayers).^{168,176}

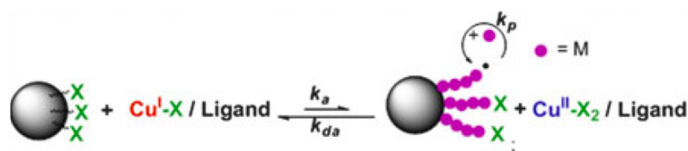


Figure 1.21. Schematic representation of “grafting from” approach used to elaborate polymer brushes on a nanoparticle by SI-ATRP.¹⁶⁸

The architecture and the properties of the polymeric brush can easily be modulated and adapted to the specific geometry of the material. This ability to control this chain topology (linear, branched, hyperbranched, and crosslinked chains) and/or composition is a major tool for the preparation of hybrid materials.

So far, Jacques *et al.* are the only ones to prepare polymer coatings on Nitinol by SI-ATRP: in their work, they assess the polymerization of 2-hydroxyethyl methacrylate initiated from Nitinol surface derivatized by diazonium salts.¹²³ The present work will focus on SI-ATRP of 2-(dimethylamino)ethyl methacrylate and 2-methacryloyloxyethyl phosphorylcholine on SAMs-covered Nitinol, which will be further discussed in chapters 4 and 5.

References

- (1) Murray, C. J. L.; Vos, T.; Lozano, R.; Naghavi, M.; Flaxman, A. D.; Michaud, C.; Ezzati, M.; Shibuya, K.; Salomon, J. A.; Abdalla, S.; et al. Disability-Adjusted Life Years (DALYs) for 291 Diseases and Injuries in 21 Regions, 1990-2010: A Systematic Analysis for the Global Burden of Disease Study 2010. *Lancet* **2012**, *380* (9859), 2197–2223.
- (2) Hunter, D. J.; Reddy, K. S. Noncommunicable Diseases. *N. Engl. J. Med.* **2013**, *369* (14), 1336–1343.
- (3) Observatoire de la Santé du Hainaut. Tableau de Bord de La Santé 2016. *Santé en Hainaut* **2016**, *12*.
- (4) World Health Organization; World Heart Federation; World Stroke Organization.

- Global Atlas on Cardiovascular Disease Prevention and Control*; Mendis, S., Pusha, P., Norrving, B., Eds.; 2011.
- (5) Sanchis-Gomar, F.; Perez-Quilis, C.; Leischik, R.; Lucia, A. Epidemiology of Coronary Heart Disease and Acute Coronary Syndrome. *Ann. Transl. Med.* **2016**, *4* (13), 256–256.
 - (6) World Health Organization. WHO Mortality Database <http://apps.who.int/healthinfo/statistics/mortality/whodpms/> (accessed May 22, 2018).
 - (7) Wilkins, E.; Wilson, L.; Wickramasinghe, K.; Bhatnagar, P.; Leal, J.; Luengo-Fernandez, R.; Burns, R.; Rayner, M.; Townsend, N. *European Cardiovascular Disease Statistics 2017*; Brussels, 2017.
 - (8) Benjamin, E. J.; Blaha, M. J.; Chiuve, S. E.; Cushman, M.; Das, S. R.; Deo, R.; De Ferranti, S. D.; Floyd, J.; Fornage, M.; Gillespie, C.; et al. *Heart Disease and Stroke Statistics'2017 Update: A Report from the American Heart Association*; 2017; Vol. 135.
 - (9) Yang, Q.; Cogswell, M. E.; Dana Flanders, W.; Hong, Y.; Zhang, Z.; Loustalot, F.; Gillespie, C.; Merritt, R.; Hu, F. B. Trends in Cardiovascular Health Metrics and Associations with All-Cause and CVD Mortality among Us Adults. *JAMA - J. Am. Med. Assoc.* **2012**, *307* (12), 1273–1283.
 - (10) Virmani, R.; Burke, A. P.; Willerson, J. T.; Farb, A.; Narula, J.; Kolodgie, F. D. The Pathology of Vulnerable Plaque. *Vulnerable Atheroscler. Plaque Strateg. Diagnosis Manag.* **2007**, *47* (8), 19–36.
 - (11) Sakakura, K.; Nakano, M.; Otsuka, F.; Ladich, E.; Kolodgie, F. D.; Virmani, R. Pathophysiology of Atherosclerosis Plaque Progression. *Heart Lung Circ.* **2013**, *22* (6), 399–411.
 - (12) Arbab-Zadeh, A.; Fuster, V. The Myth of the “Vulnerable Plaque”: Transitioning from a Focus on Individual Lesions to Atherosclerotic Disease Burden for Coronary Artery Disease Risk Assessment. *J. Am. Coll. Cardiol.* **2015**, *65* (8), 846–855.
 - (13) Virmani, R.; Virmani, R.; Kolodgie, F. D.; Kolodgie, F. D.; Burke, A. P.; Burke, A. P.; Farb, A.; Farb, A.; Schwartz, S. M.; Schwartz, S. M.; et al. Lessons From Sudden Coronary Death. *Arter. Thromb Biol* **2000**, 1262–1275.
 - (14) Sandfort, V.; Lima, J. A. C.; Bluemke, D. A. Noninvasive Imaging of Atherosclerotic Plaque Progression: Status of Coronary Computed Tomography Angiography. *Circ. Cardiovasc. Imaging* **2015**, *8* (7), 1–14.
 - (15) Guerrero, G.; Alauzun, J. G.; Granier, M.; Laurencin, D.; Mutin, P. H. Phosphonate Coupling Molecules for the Control of Surface/Interface Properties and the Synthesis of Nanomaterials. *Dalt. Trans.* **2013**, *42* (35), 12569.
 - (16) Schaar, J. A.; Muller, J. E.; Falk, E.; Virmani, R.; Fuster, V.; Serruys, P. W.; Colombo, A.; Stefanadis, C.; Casscells, S. W.; Moreno, P. R.; et al. Terminology for High-Risk and Vulnerable Coronary Artery Plaques. *Eur. Heart J.* **2004**, *25* (12), 1077–1082.
 - (17) Silvain, J.; Cayla, G.; Collet, J.-P.; Fargeot, C.; Montalescot, G. Stents Coronaires: 30 Ans de Progrès Médical. *médecine/sciences* **2014**, *30* (3), 303–310.
 - (18) Effler, D. B.; Favalaro, R. G.; Groves, L. K. Coronary Artery Surgery Utilizing Saphenous Vein Graft Techniques. Clinical Experience with 224 Operation. *J.*

- Thorac. Cardiovasc. Surg.* **1970**, *59* (1), 147–154.
- (19) Mueller, R. L.; Rosengart, T. K.; Isom, O. W. The History of Surgery for Ischemic Heart Disease. *Ann. Thorac. Surg.* **1997**, *63* (3), 869–878.
- (20) Barton, M.; Grüntzig, J.; Husmann, M.; Rösch, J. Balloon Angioplasty - The Legacy of Andreas Grüntzig, M.D. (1939-1985). *Front. Cardiovasc. Med.* **2014**, *1* (December), 1–25.
- (21) Grüntzig, A. TRANSLUMINAL DILATATION OF CORONARY-ARTERY STENOSIS. *Lancet* **1978**, *311* (8058), 263.
- (22) Byrne, R. A.; Stone, G. W.; Ormiston, J.; Kastrati, A. Coronary Balloon Angioplasty, Stents, and Scaffolds. *Lancet* **2017**, *390* (10096), 781–792.
- (23) McKavanagh, P.; Zawadowski, G.; Ahmed, N.; Kutryk, M. The Evolution of Coronary Stents. *Expert Rev. Cardiovasc. Ther.* **2018**, *16* (3), 219–228.
- (24) Simpson, J. B.; Baim, D. S.; Robert, E. W.; Harrison, D. C. A New Catheter System for Coronary Angioplasty. *Am. J. Cardiol.* **1982**, *49* (5), 1216–1222.
- (25) Sigwart, U.; Puel, J.; Mirkovitch, V.; Joffe, F.; Kappenberger, L. Intravascular Stents to Prevent Occlusion and Re-Stenosis after Transluminal Angioplasty. *N. Engl. J. Med.* **1987**, *316* (12), 701–706.
- (26) Stefanini, G. G.; Holmes, D. R. Drug-Eluting Coronary-Artery Stents. *N. Engl. J. Med.* **2013**, *368* (3), 254–265.
- (27) Serruys, P. W.; Strauss, B. H.; Beatt, K. J.; Bertrand, M. E.; Puel, J.; Rickards, A. F.; Meier, B.; Goy, J.-J.; Vogt, P.; Kappenberger, L.; et al. Angiographic Follow-up after Placement of a Self-Expanding Coronary-Artery Stent. *N. Engl. J. Med.* **1991**, *324* (1), 13–17.
- (28) Chen, M. S.; John, J. M.; Chew, D. P.; Lee, D. S.; Ellis, S. G.; Bhatt, D. L. Bare Metal Stent Restenosis Is Not a Benign Clinical Entity. *Am. Heart J.* **2006**, *151* (6), 1260–1264.
- (29) Doyle, B.; Rihal, C. S.; O'Sullivan, C. J.; Lennon, R. J.; Wiste, H. J.; Bell, M.; Bresnahan, J.; Holmes, D. R. Outcomes of Stent Thrombosis and Restenosis during Extended Follow-up of Patients Treated with Bare-Metal Coronary Stents. *Circulation* **2007**, *116* (21), 2391–2398.
- (30) Ho, M.-Y.; Chen, C.-C.; Wang, C.-Y.; Chang, S.-H.; Hsieh, M.-J.; Lee, C.-H.; Wu, V.; Hsieh, I.-C. The Development of Coronary Artery Stents: From Bare-Metal to Bio-Resorbable Types. *Metals (Basel)*. **2016**, *6* (7), 168.
- (31) Kastrati, A.; Mehilli, J.; Dirschinger, J.; Dotzer, F.; Schuhlen, H.; Neumann, F.-J.; Fleckenstein, M.; Pfafferott, C.; Seyfarth, M.; Schomig, A. Intracoronary Stenting and Angiographic Results: Strut Thickness Effect on Restenosis Outcome (ISAR-STEREO) Trial. *Circulation* **2001**, *103* (23), 2816–2821.
- (32) Morice, M.-C.; Serruys, P. W.; Sousa, J. E.; Fajadet, J.; Ban Hayashi, E.; Perin, M.; Colombo, A.; Schuler, G.; Barragan, P.; Guagliumi, G.; et al. A Randomized Comparison of a Sirolimus-Eluting Stent with a Standard Stent for Coronary Revascularization. *N. Engl. J. Med.* **2002**, *346* (23), 1773–1780.
- (33) Kereiakes, D. J.; Cox, D. A.; Hermiller, J. B.; Midei, M. G.; Bachinsky, W. B.; Nukta, E. D.; Leon, M. B.; Fink, S.; Marin, L.; Lansky, A. J. Usefulness of a Cobalt Chromium Coronary Stent Alloy. *Am. J. Cardiol.* **2003**, *92* (4), 463–466.
- (34) Sketch, M. H.; Ball, M.; Rutherford, B.; Popma, J. J.; Russell, C.; Kereiakes, D. J.

- Evaluation of the Medtronic (Driver) Cobalt-Chromium Alloy Coronary Stent System. *Am. J. Cardiol.* **2005**, *95* (1), 8–12.
- (35) Moses, J. W.; Leon, M. B.; Popma, J. J.; Fitzgerald, P. J.; Holmes, D. R.; O’Shaughnessy, C.; Caputo, R. P.; Kereiakes, D. J.; Williams, D. O.; Teirstein, P. S.; et al. Sirolimus-Eluting Stents versus Standard Stents in Patients with Stenosis in a Native Coronary Artery. *N. Engl. J. Med.* **2003**, *349* (14), 1315–1323.
- (36) Grube, E.; Silber, S.; Hauptmann, K. E.; Mueller, R.; Buellesfeld, L.; Gerckens, U.; Russell, M. E. Six- and Twelve-Month Results from a Randomized, Double-Blind Trial on a Slow-Release Paclitaxel-Eluting Stent for de Novo Coronary Lesions. *Circulation* **2003**, *107* (1), 38–42.
- (37) Schampaert, E.; Cohen, E. A.; Schlüter, M.; Reeves, F.; Traboulsi, M.; Title, L. M.; Kuntz, R. E.; Popma, J. J. The Canadian Study of the Sirolimus-Eluting Stent in the Treatment of Patients with Long de Novo Lesions in Small Native Coronary Arteries (C-SIRIUS). *J. Am. Coll. Cardiol.* **2004**, *43* (6), 1110–1115.
- (38) Camenzind, E.; Steg, P. G.; Wijns, W. Stent Thrombosis Late After Implantation of First-Generation Drug-Eluting Stents. *Circulation* **2007**, *115* (11), 1440–1455.
- (39) Jensen, L. O.; Thayssen, P.; Christiansen, E. H.; Maeng, M.; Ravkilde, J.; Hansen, K. N.; Hansen, H. S.; Krusell, L.; Kaltoft, A.; Tilsted, H. H.; et al. Safety and Efficacy of Everolimus- versus Sirolimus-Eluting Stents 5-Year Results from SORT OUT IV. *J. Am. Coll. Cardiol.* **2016**, *67* (7), 751–762.
- (40) Bharadwaj, P.; Chadha, D. S. Drug Eluting Stents: To Evolve or Dissolve? *Med. J. Armed Forces India* **2016**, *72* (4), 367–372.
- (41) O’Brien, B.; Zafar, H.; Ibrahim, A.; Zafar, J.; Sharif, F. Coronary Stent Materials and Coatings: A Technology and Performance Update. *Ann. Biomed. Eng.* **2016**, *44* (2), 523–535.
- (42) Duerig, T. W.; Wholey, M. A Comparison of Balloon- and Self-Expanding Stents. *Minim. Invasive Ther. Allied Technol.* **2002**, *11* (4), 173–178.
- (43) Levy, E. I.; Chaturvedi, S. Perforator Stroke Following Intracranial Stenting: A Sacrifice for the Greater Good? *Neurology* **2006**, *66* (12), 1803–1804.
- (44) Van Geuns, R. J.; Tamburino, C.; Fajadet, J.; Vrolix, M.; Witzenbichler, B.; Eeckhout, E.; Spaulding, C.; Reczuch, K.; La Manna, A.; Spaargaren, R.; et al. Self-Expanding versus Balloon-Expandable Stents in Acute Myocardial Infarction: Results from the APPPOSITION II Study: Self-Expanding Stents in ST-Segment Elevation Myocardial Infarction. *JACC Cardiovasc. Interv.* **2012**, *5* (12), 1209–1219.
- (45) Gogas, B. D. Bioresorbable Scaffolds for Percutaneous Coronary Interventions. *Glob. Cardiol. Sci. Pract.* **2014**, *2014* (4), 55.
- (46) Bünger, C. M.; Grabow, N.; Sternberg, K.; Goosmann, M.; Schmitz, K.-P.; Kreutzer, H. J.; Ince, H.; Kische, S.; Nienaber, C. a; Martin, D. P.; et al. A Biodegradable Stent Based on Poly(L-Lactide) and Poly(4-Hydroxybutyrate) for Peripheral Vascular Application: Preliminary Experience in the Pig. *J. Endovasc. Ther.* **2007**, *14*, 725–733.
- (47) Jabara, R.; Chronds, N.; Robinson, K. Novel Bioabsorbable Salicylate-Based Polymer as a Drug-Eluting Stent Coating. *Catheter. Cardiovasc. Interv.* **2008**, *72* (2), 186–194.
- (48) Gonzalo, N.; Macaya, C. Absorbable Stent: Focus on Clinical Applications and

- Benefits. *Vasc. Health Risk Manag.* **2012**, *8* (1), 125–132.
- (49) Naseem, R.; Zhao, L.; Liu, Y.; Silberschmidt, V. V. Experimental and Computational Studies of Poly-L-Lactic Acid for Cardiovascular Applications: Recent Progress. *Mech. Adv. Mater. Mod. Process.* **2017**, *3* (1), 13.
- (50) Demir, A. G.; Previtali, B.; Ge, Q.; Vedani, M.; Wu, W.; Migliavacca, F.; Petrini, L.; Biffi, C. A.; Bestetti, M. Biodegradable Magnesium Coronary Stents: Material, Design and Fabrication. *Int. J. Comput. Integr. Manuf.* **2014**, *27* (10), 936–945.
- (51) Mostaed, E.; Sikora-Jasinska, M.; Mostaed, A.; Loffredo, S.; Demir, A. G.; Previtali, B.; Mantovani, D.; Beanland, R.; Vedani, M. Novel Zn-Based Alloys for Biodegradable Stent Applications: Design, Development and in Vitro Degradation. *J. Mech. Behav. Biomed. Mater.* **2016**, *60*, 581–602.
- (52) Katarivas Levy, G.; Goldman, J.; Aghion, E. The Prospects of Zinc as a Structural Material for Biodegradable Implants—A Review Paper. *Metals (Basel)*. **2017**, *7* (10), 402.
- (53) Mao, L.; Shen, L.; Chen, J.; Zhang, X.; Kwak, M.; Wu, Y.; Fan, R.; Zhang, L.; Pei, J.; Yuan, G.; et al. A Promising Biodegradable Magnesium Alloy Suitable for Clinical Vascular Stent Application. *Sci. Rep.* **2017**, *7* (April), 1–12.
- (54) Sotomi, Y.; Suwannasom, P.; Serruys, P.; Onuma, Y. Possible Mechanical Causes of Scaffold Thrombosis: Insights from Case Reports with Intracoronary Imaging. *EuroIntervention* **2017**, *12* (14), 1747–1756.
- (55) Kerkmeijer, L. S.; Tenekecioglu, E.; Wykrzykowska, J. J. Stent Thrombosis in Patients with Drug - - Eluting Stents and Bioresorbable Vascular Scaffolds: The Feared Complication. **2018**.
- (56) Indolfi, C.; De Rosa, S.; Colombo, A. Bioresorbable Vascular Scaffolds — Basic Concepts and Clinical Outcome. *Nat. Rev. Cardiol.* **2016**, *13* (12), 719–729.
- (57) Stentys. Products <http://www.stentys.com/products/> (accessed Jul 30, 2018).
- (58) Boston Scientific. Epic™ Vascular Self-Expanding Stent System <http://www.bostonscientific.com/en-US/products/stents--vascular/Epic-Vascular-Self-Expanding-Stent-System.html> (accessed Jul 30, 2018).
- (59) Cordis. Self-Expanding Stents <https://emea.cordis.com/emea/endovascular/lower-extremity-solutions/intervene/self-expanding-stents.html> (accessed Jul 30, 2018).
- (60) medicut. Medizinprodukte <http://www.medicut.de/de/medizinprodukte.html> (accessed Jul 30, 2018).
- (61) Norman Noble. Vascular medical devices implants <http://nnoble.com/applications/medical-devices-implants/vascular> (accessed Jul 30, 2018).
- (62) Buehler, W. J.; Gilfrich, J. V.; Wiley, R. C. Effect of Low-Temperature Phase Changes on the Mechanical Properties of Alloys near Composition TiNi. *J. Appl. Phys.* **1963**, *34* (5), 1475–1477.
- (63) Shabalovskaya, S. A. Surface, Corrosion and Biocompatibility Aspects of Nitinol as an Implant Material. *Biomed. Mater. Eng.* **2002**, *12* (1), 69–109.
- (64) Elahinia, M. H.; Hashemi, M.; Tabesh, M.; Bhaduri, S. B. Manufacturing and Processing of NiTi Implants: A Review. *Prog. Mater. Sci.* **2012**, *57* (5), 911–946.
- (65) Duerig, T.; Pelton, A.; Stöckel, D. An Overview of Nitinol Medical Applications. *Mater. Sci. Eng. A* **1999**, *273–275*, 149–160.

-
- (66) Centre d'Animation Régional en Matériaux Avancés (C.A.R.M.A.). *Alliages à Mémoire de Forme*, 2001.
- (67) Mantovani, D. Shape Memory Alloys: Properties and Biomedical Applications. *JOM* **2000**, *52* (10), 36–44.
- (68) Mohd Jani, J.; Leary, M.; Subic, A.; Gibson, M. A. A Review of Shape Memory Alloy Research, Applications and Opportunities. *Mater. Des.* **2014**, *56*, 1078–1113.
- (69) Guda Vishnu, K.; Strachan, A. Phase Stability and Transformations in NiTi from Density Functional Theory Calculations. *Acta Mater.* **2010**, *58* (3), 745–752.
- (70) Kusy, R. P.; Whitley, J. Q. Thermal and Mechanical Characteristics of Stainless Steel, Titanium-Molybdenum, and Nickel-Titanium Archwires. *Am. J. Orthod. Dentofac. Orthop.* **2007**, *131* (2), 229–237.
- (71) Robertson, S. W.; Pelton, A. R.; Ritchie, R. O. Mechanical Fatigue and Fracture of Nitinol. *Int. Mater. Rev.* **2012**, *57* (1), 1–37.
- (72) Machado, L. G.; Savi, M. A. Medical Applications of Shape Memory Alloys. *Brazilian J. Med. Biol. Res.* **2003**, *36* (6), 683–691.
- (73) Follador, M.; Cianchetti, M.; Arienti, A.; Laschi, C. A General Method for the Design and Fabrication of Shape Memory Alloy Active Spring Actuators. *Smart Mater. Struct.* **2012**, *21* (11), 115029.
- (74) Branco, M. M.; Kelly, J. M.; Guerreiro, L. M. An Algorithm to Simulate the One-Dimensional Superelastic Cyclic Behavior of NiTi Strings, for Civil Engineering Applications. *Eng. Struct.* **2011**, *33* (12), 3737–3747.
- (75) Khalil-Allafi, J.; Amin-Ahmadi, B.; Zare, M. Biocompatibility and Corrosion Behavior of the Shape Memory NiTi Alloy in the Physiological Environments Simulated with Body Fluids for Medical Applications. *Mater. Sci. Eng. C* **2010**, *30* (8), 1112–1117.
- (76) Fonte, M. Osteosynthetic Shape Memory Material Intramedullary Bone Stent and Method for Treating a Bone Fracture Using the Same. US20130123785 A1, 2013.
- (77) Duerig, T. W.; Melton, K. N.; Stöckel, D. *Engineering Aspects of Shape Memory Alloys*, Butterworth.; London, 1990.
- (78) Airoldi, G.; Riva, G.; Vanelli, M. Superelasticity and Shape Memory Effect in NiTi Orthodontic Wires. *J. Phys. IV* **1995**, *05* (C8), 1205–1210.
- (79) Laster, Z.; MacBean, A. D.; Ayliffe, P. R.; Newlands, L. C. Fixation of a Frontozygomatic Fracture with a Shape-Memory Staple. *Br. J. Oral Maxillofac. Surg.* **2001**, *39* (4), 324–325.
- (80) Luebke, N.; Brantley, W.; Alapati, S.; Mitchell, J.; Lausten, L.; Daehn, G. Bending Fatigue Study of Nickel-Titanium Gates Glidden Drills. *J. Endod.* **2005**, *31* (7), 523–525.
- (81) Shabalovskaya, S. A.; Rondelli, G. C.; Undisz, A. L.; Andereg, J. W.; Burleigh, T. D.; Rettenmayr, M. E. The Electrochemical Characteristics of Native Nitinol Surfaces. *Biomaterials* **2009**, *30* (22), 3662–3671.
- (82) Virtanen, S. Degradation of Titanium and Its Alloys. In *Degradation of Implant Materials*; Eliaz, N., Ed.; Springer, 2012.
- (83) Shabalovskaya, S. A.; Tian, H.; Andereg, J. W.; Schryvers, D. U.; Carroll, W. U.; Van Humbeek, J. The Influence of Surface Oxides on the Distribution and Release of Nickel from Nitinol Wires. *Biomaterials* **2009**, *30* (4), 468–477.

- (84) Figueira, N.; Silva, T. M.; Carmezim, M. J.; Fernandes, J. C. S. Corrosion Behaviour of NiTi Alloy. *Electrochim. Acta* **2009**, *54* (3), 921–926.
- (85) Milošev, I.; Kapun, B. The Corrosion Resistance of Nitinol Alloy in Simulated Physiological Solutions: Part 1: The Effect of Surface Preparation. *Mater. Sci. Eng. C* **2012**, *32* (5), 1087–1096.
- (86) Lü, X.; Bao, X.; Huang, Y.; Qu, Y.; Lu, H.; Lu, Z. Mechanisms of Cytotoxicity of Nickel Ions Based on Gene Expression Profiles. *Biomaterials* **2009**, *30* (2), 141–148.
- (87) Lee, J.; Son, Y.; Pratheeshkumar, P.; Shi, X. Oxidative Stress and Metal Carcinogenesis. *Free Radic. Biol. Med.* **2012**, *53* (4), 742–757.
- (88) Jin, S.; Zhang, Y.; Wang, Q.; Zhang, D.; Zhang, S. Influence of TiN Coating on the Biocompatibility of Medical NiTi Alloy. *Colloids Surfaces. B Biointerfaces* **2013**, *101*, 343–349.
- (89) Pourbaix, M. *Atlas of Electrochemical Equilibria in Aqueous Solutions*, Pergam Press Ltd., 1974.
- (90) Auricchio, F.; Boatti, E.; Conti, M. SMA Biomedical Applications. In *Shape Memory Alloy Engineering: For Aerospace, Structural and Biomedical Applications*; Elsevier Ltd, 2014; pp 307–341.
- (91) Es-Souni, M.; Es-Souni, M.; Fischer-Brandies, H. Assessing the Biocompatibility of NiTi Shape Memory Alloys Used for Medical Applications. *Anal. Bioanal. Chem.* **2005**, *381* (3), 557–567.
- (92) Barras, C. D. J.; Myers, K. A. Nitinol – Its Use in Vascular Surgery and Other Applications. *Eur. J. Vasc. Endovasc. Surg.* **2000**, *19* (6), 564–569.
- (93) Denkhaus, E.; Salmikow, K. Nickel Essentiality, Toxicity, and Carcinogenicity. *Crit. Rev. Oncol. Hematol.* **2002**, *42* (1), 35–56.
- (94) Kasprzak, K. S.; Sunderman, F. W.; Salmikow, K. Nickel Carcinogenesis. *Mutat. Res. - Fundam. Mol. Mech. Mutagen.* **2003**, *533* (1–2), 67–97.
- (95) Leonard, S. S.; Harris, G. K.; Shi, X. Serial Review : Redox-Active Metal Ions , Reactive Oxygen Species , and Apoptosis. *Free Radic. Biol. Med.* **2004**, *37* (12), 1921–1942.
- (96) Schrader, M.; Fahimi, H. D. Peroxisomes and Oxidative Stress. *Biochim. Biophys. Acta* **2006**, *1763*, 1755–1766.
- (97) Nishino, T.; Okamoto, K.; Eger, B. T.; Pai, E. F.; Nishino, T. Mammalian Xanthine Oxidoreductase - Mechanism of Transition from Xanthine Dehydrogenase to Xanthine Oxidase. *FEBS J.* **2008**, *275* (13), 3278–3289.
- (98) Li, Y.; Zamble, D. B. Nickel Homeostasis and Nickel Regulation: An Overview. *Chem. Rev.* **2009**, *109* (10), 4617–4643.
- (99) Brocato, J.; Costa, M. Nickel Toxicity and Carcinogenesis. In *The Biological Chemistry of Nickel*; Zamble, D., Rowinska-Zyrek, M., Kozłowski, H., Eds.; The Royal Society of Chemistry, 2017.
- (100) Soleimani, E.; Moghadam, R. H.; Ranjbar, A. Occupational Exposure to Chemicals and Oxidative Toxic Stress. *Toxicol. Environ. Health Sci.* **2015**, *7* (1), 1–24.
- (101) Feser, R. Uniform Corrosion of Metals in Acid, Neutral and Alkaline Electrolytes. In *Encyclopedia of Electrochemistry, Volume 4 - Corrosion and Oxide Films*; Stratmann, M., Frankel, G. S., Eds.; Wiley-VCH, 2003.
- (102) Jones, D. A. *Principles and Prevention of Corrosion*, 2nd Ed.; Prentice Hall, 1996.

-
- (103) Eiselstein, L. E. Corrosion of Shape Memory and Superelastic Alloys. In *Uhlig's Corrosion Handbook*; Winston Revie, R., Ed.; Wiley, 2011.
- (104) Stansbury, E. E.; Buchanan, R. A. *Fundamentals of Electrochemical Corrosion*; ASTM International, 2000.
- (105) Strehblow, H.-H. Pitting Corrosion. In *Corrosion and Oxide Films*; Stratmann, M., Frankel, G. S., Eds.; Wiley-VCH, 2003.
- (106) Kelly, R. G. Crevice Corrosion. In *Corrosion and Oxide Films*; Stratmann, M., Frankel, G. S., Eds.; Wiley-VCH, 2003.
- (107) Stansbury, E. E.; Buchanan, R. A. Localized Corrosion. In *Fundamentals of Electrochemical Corrosion*; ASM International, 2000.
- (108) Trépanier, C.; Gong, X. Y.; Ditter, T.; Pelton, A.; Neely, Y.; Grishaber, R. Effect of Wear and Crevice on the Corrosion Resistance of Overlapped Stents. *Proc. Int. Conf. Shape Mem. Superelastic Technol.* **2008**, 265–276.
- (109) Groysman, A. *Corrosion for Everybody*; Springer Netherlands: Dordrecht, 2010.
- (110) Groysman, A. *Corrosion Problems and Solutions in Old Refining and Petrochemical Industry*; 2017.
- (111) Schroeder, V. Evolution of the Passive Film on Mechanically Damaged Nitinol. *J. Biomed. Mater. Res. - Part A* **2009**, *90* (1), 1–17.
- (112) Yang, J.; Wang, J.; Tong, S. Surface Properties of Bio-Implant Nitinol Modified by ECR Cold Plasma. *Mater. Sci. Technol.* **2004**, *20* (November), 1427–1431.
- (113) Shen, Y.; Wang, G.; Chen, L.; Li, H.; Yu, P.; Bai, M.; Zhang, Q.; Lee, J.; Yu, Q. Investigation of Surface Endothelialization on Biomedical Nitinol (NiTi) Alloy: Effects of Surface Micropatterning Combined with Plasma Nanocoatings. *Acta Biomater.* **2009**, *5* (9), 3593–3604.
- (114) Siu, H. T.; Man, H. C. Fabrication of Bioactive Titania Coating on Nitinol by Plasma Electrolytic Oxidation. *Appl. Surf. Sci.* **2013**, *274*, 181–187.
- (115) Lahann, J.; Klee, D.; Thelen, H.; Bienert, H.; Vorwerk, D.; Höcker, H. Improvement of Haemocompatibility of Metallic Stents by Polymer Coating. *J. Mater. Sci. Mater. Med.* **1999**, *10* (7), 443–448.
- (116) Catledge, S. A.; Thomas, V.; Vohra, Y. K. Effect of Surface Oxides and Intermetallics on Nanostructured Diamond Coating of Nitinol. *Curr. Nanosci.* **2006**, *2* (1), 9–12.
- (117) Pérez, L. M.; Gracia-Villa, L.; Puértolas, J. A.; Arruebo, M.; Irusta, S.; Santamaría, J. Effect of Nitinol Surface Treatments on Its Physico-Chemical Properties. *J. Biomed. Mater. Res. B. Appl. Biomater.* **2009**, *91* (1), 337–347.
- (118) Devillers, S.; Barthélémy, B.; Delhalle, J.; Mekhalif, Z. Induction Heating Vs Conventional Heating for the Hydrothermal Treatment of Nitinol and Its Subsequent 2-(Methacryloyloxy)Ethyl 2-(Trimethylammonio)Ethyl Phosphate Coating by Surface-Initiated Atom Transfer Radical Polymerization. *ACS Appl. Mater. Interfaces* **2011**, *3* (10), 4059–4066.
- (119) Quiñones, R.; Gawalt, E. S. Study of the Formation of Self-Assembled Monolayers on Nitinol. *Langmuir* **2007**, *23* (20), 10123–10130.
- (120) Petrovic, Z.; Katic, J.; Metikos-Hukovic, M.; Dadafarin, H.; Omanovic, S. Modification of a Nitinol Surface by Phosphonate Self-Assembled Monolayers. *J. Electrochem. Soc.* **2011**, *158* (10), F159–F165.

- (121) Maho, A.; Kanoufi, F.; Combellas, C.; Delhalle, J.; Mekhalif, Z. Electrochemical Investigation of Nitinol/Tantalum Hybrid Surfaces Modified by Alkylphosphonic Self-Assembled Monolayers. *Electrochim. Acta* **2014**, *116*, 78–88.
- (122) Quiñones, R.; Gawalt, E. S. Polystyrene Formation on Monolayer-Modified Nitinol Effectively Controls Corrosion. *Langmuir* **2008**, *24* (19), 10858–10864.
- (123) Jacques, A.; Barthélémy, B.; Delhalle, J.; Mekhalif, Z. Nitinol Modified by In Situ Generated Diazonium from Its Nitro Precursor for the SI-ATRP of 2-Hydroxyethyl Methacrylate. *J. Electrochem. Soc.* **2015**, *162* (10), G94–G102.
- (124) Dilimon, V. S.; Rajalingam, S.; Delhalle, J.; Mekhalif, Z. Self-Assembly Mechanism of Thiol, Dithiol, Dithiocarboxylic Acid, Disulfide and Diselenide on Gold: An Electrochemical Impedance Study. *Phys. Chem. Chem. Phys.* **2013**, *15* (39), 16648.
- (125) Guo, Q.; Li, F. Self-Assembled Alkanethiol Monolayers on Gold Surfaces: Resolving the Complex Structure at the Interface by STM. *Phys. Chem. Chem. Phys.* **2014**, *16*, 19074–19090.
- (126) Velachi, V.; Bhandary, D.; Singh, J. K.; Cordeiro, M. N. D. S. Structure of Mixed Self-Assembled Monolayers on Gold Nanoparticles at Three Different Arrangements. *J. Phys. Chem. C* **2015**, *119* (6), 3199–3209.
- (127) Patel, D. A.; Weller, A. M.; Chevalier, R. B.; Karos, C. A.; Landis, E. C. Ordering and Defects in Self-Assembled Monolayers on Nanoporous Gold. *Appl. Surf. Sci.* **2016**, *387*, 503–512.
- (128) Mani, G.; Johnson, D. M.; Marton, D.; Dougherty, V. L.; Feldman, M. D.; Patel, D.; Ayon, A. A.; Agrawal, C. M. Stability of Self-Assembled Monolayers on Titanium and Gold. *Langmuir* **2008**, *24* (13), 6774–6784.
- (129) Meth, S.; Savchenko, N.; Viva, F. A.; Starosvetsky, D.; Groysman, A.; Sukenik, C. N. Siloxane-Based Thin Films for Corrosion Protection of Stainless Steel in Chloride Media. *J. Appl. Electrochem.* **2011**, *41* (8), 885–890.
- (130) Roy, F.; Et Taouil, A.; Lallemand, F.; Melot, J.-M.; Roizard, X.; Heintz, O.; Moutarlier, V.; Hihn, J.-Y. Influence of Modification Time and High Frequency Ultrasound Irradiation on Self-Assembling of Alkylphosphonic Acids on Stainless Steel: Electrochemical and Spectroscopic Studies. *Ultrason. Sonochem.* **2016**, *28*, 269–275.
- (131) Marcinko, S.; Fadeev, A. Y. Hydrolytic Stability of Organic Monolayers Supported on TiO₂ and ZrO₂. *Langmuir* **2004**, *20* (3), 2270–2273.
- (132) Paz, Y. Self-Assembled Monolayers and Titanium Dioxide: From Surface Patterning to Potential Applications. *Beilstein J. Nanotechnol.* **2011**, *2*, 845–861.
- (133) Jacques, A.; Barthélémy, B.; Delhalle, J.; Mekhalif, Z. 1-Pyrrolyl-10-Decylammoniumphosphonate Monolayer: A Molecular Nanolink between Electropolymerized Pyrrole Films and Nickel or Titanium Surfaces. *Electrochim. Acta* **2015**, *170*, 218–228.
- (134) Quiñones, R.; Raman, A.; Gawalt, E. S. Functionalization of Nickel Oxide Using Alkylphosphonic Acid Self-Assembled Monolayers. *Thin Solid Films* **2008**, *516* (23), 8774–8781.
- (135) Devillers, S.; Lemineur, J. F.; Dilimon, V. S.; Barthélémy, B.; Delhalle, J.; Mekhalif, Z. Polyelectrolyte Multilayer Deposition on Nickel Modified with Self-Assembled Monolayers of Organophosphonic Acids for Biomaterials: Electrochemical and

- Spectroscopic Evaluation. *J. Phys. Chem. C* **2012**, *116* (36), 19252–19261.
- (136) Mohapatra, S.; Pramanik, P. Synthesis and Stability of Functionalized Iron Oxide Nanoparticles Using Organophosphorus Coupling Agents. *Colloids Surfaces A Physicochem. Eng. Asp.* **2009**, *339* (1–3), 35–42.
- (137) Paszternák, A.; Felhósi, I.; Pászti, Z.; Kuzmann, E.; Vértes, A.; Kálmán, E.; Nyikos, L. Surface Analytical Characterization of Passive Iron Surface Modified by Alkyl-Phosphonic Acid Layers. *Electrochim. Acta* **2010**, *55* (3), 804–812.
- (138) Maxisch, M.; Thissen, P.; Giza, M.; Grundmeier, G. Interface Chemistry and Molecular Interactions of Phosphonic Acid Self-Assembled Monolayers on Oxyhydroxide-Covered Aluminum in Humid Environments. *Langmuir* **2011**, *27* (10), 6042–6048.
- (139) Hauffman, T.; Hubin, A.; Terryn, H. Study of the Self-Assembling of n-Octylphosphonic Acid Layers on Aluminum Oxide from Ethanolic Solutions. *Surf. Interface Anal.* **2013**, *45* (10), 1435–1440.
- (140) Nyman, M.; Sandberg, O.; Martínez Hardigree, J. F.; Kola, S.; Katz, H. E.; Österbacka, R. Voltage Dependent Displacement Current as a Tool to Measure the Vacuum Level Shift Caused by Self-Assembled Monolayers on Aluminum Oxide. *Appl. Phys. Lett.* **2013**, *103* (24).
- (141) Barthélémy, B.; Kanoufi, F.; Combellas, C.; Delhalle, J.; Mekhalif, Z. Phynox Improved Corrosion Resistance with MPC Initiated from Mixed Monolayers of Phosphonic Acids. *J. Electrochem. Soc.* **2014**, *161* (12), C1–C6.
- (142) Silva, D. P. B.; Neves, R. S.; Motheo, A. J. Electrochemical Behaviour of the AA2024 Aluminium Alloy Modified with Self-Assembled Monolayers/Polyaniline Double Films. *Mol. Cryst. Liq. Cryst.* **2010**, *521* (1), 179–186.
- (143) Transactions, E. C. S.; Society, T. E. Corrosion Protection of Aluminum Alloys by Methoxy-Silanes(SAM)/Polyaniline Double Films Daiane P. B. Silva. **2012**, *43* (1), 57–64.
- (144) Telegdi, J.; Luciano, G.; Mahanty, S.; Abohalkuma, T. Inhibition of Aluminum Alloy Corrosion in Electrolytes by Self-Assembled Fluorophosphonic Acid Molecular Layer. *Mater. Corros.* **2016**, *67* (10), 1027–1033.
- (145) Queffelec, C.; Petit, M.; Janvier, P.; Knight, D. A.; Bujoli, B. Surface Modification Using Phosphonic Acids and Esters. *Chem. Rev.* **2012**, *112* (7), 3777–3807.
- (146) Paniagua, S. A.; Giordano, A. J.; Smith, O. L.; Barlow, S.; Li, H.; Armstrong, N. R.; Pemberton, J. E.; Brédas, J. L.; Ginger, D.; Marder, S. R. Phosphonic Acids for Interfacial Engineering of Transparent Conductive Oxides. *Chem. Rev.* **2016**, *116* (12), 7117–7158.
- (147) Tamura, M.; Nakagawa, Y.; Tomishige, K. Self-Assembled Materials for Catalysis. In *Comprehensive Supramolecular Chemistry II*; Elsevier, 2017; Vol. 2, pp 329–349.
- (148) Love, J. C.; Estroff, L. A.; Kriebel, J. K.; Nuzzo, R. G.; Whitesides, G. M. *Self-Assembled Monolayers of Thiolates on Metals as a Form of Nanotechnology*; 2005; Vol. 105.
- (149) Maho, A.; Denayer, J.; Delhalle, J.; Mekhalif, Z. Electro-Assisted Assembly of Aliphatic Thiol, Dithiol and Dithiocarboxylic Acid Monolayers on Copper. *Electrochim. Acta* **2011**, *56*, 3954–3962.
- (150) Trino, L. D.; Bronze-Uhle, E. S.; George, A.; Mathew, M. T.; Lisboa-Filho, P. N.

- Surface Physicochemical and Structural Analysis of Functionalized Titanium Dioxide Films. *Colloids Surfaces A Physicochem. Eng. Asp.* **2018**, *546* (March), 168–178.
- (151) Mutin, P. H.; Guerrero, G.; Vioux, A. Hybrid Materials from Organophosphorus Coupling Molecules. *J. Mater. Chem.* **2005**, *15* (35–36), 3761–3768.
- (152) Nanda, D.; Varshney, P.; Satapathy, M.; Mohapatra, S. S.; Kumar, A. Self-Assembled Monolayer of Functionalized Silica Microparticles for Self-Cleaning Applications. *Colloids Surfaces A Physicochem. Eng. Asp.* **2017**, *529* (June), 231–238.
- (153) Nilsing, M.; Persson, P.; Ojamäe, L. Anchor Group Influence on Molecule-Metal Oxide Interfaces: Periodic Hybrid DFT Study of Pyridine Bound to TiO₂ via Carboxylic and Phosphonic Acid. *Chem. Phys. Lett.* **2005**, *415* (4–6), 375–380.
- (154) Luschtinetz, R.; Gemming, S.; Seifert, G. Anchoring Functional Molecules on TiO₂ Surfaces: A Comparison between the Carboxylic and the Phosphonic Acid Group. *Eur. Phys. J. Plus* **2011**, *126* (10), 1–13.
- (155) Hotchkiss, P. J.; Jones, S. C.; Paniagua, S. A.; Sharma, A.; Kippelen, B.; Armstrong, N. R.; Marder, S. R. The Modification of Indium Tin Oxide with Phosphonic Acids: Mechanism of Binding, Tuning of Surface Properties, and Potential for Use in Organic Electronic Applications. *Acc. Chem. Res.* **2012**, *45* (3), 337–346.
- (156) Bhure, R.; Mahapatro, A.; Bonner, C.; Abdel-Fattah, T. M. In Vitro Stability Study of Organophosphonic Self Assembled Monolayers (SAMs) on Cobalt Chromium (Co-Cr) Alloy. *Mater. Sci. Eng. C* **2013**, *33* (4), 2050–2058.
- (157) Mahapatro, A.; Matos Negrón, T. D.; Nguyen, A. Spectroscopic Evaluations of Interfacial Oxidative Stability of Phosphonic Nanocoatings on Magnesium. *J. Spectrosc.* **2015**, *2015*, 1–8.
- (158) Guerrero, G.; Alauzun, J. G.; Granier, M.; Laurencin, D.; Mutin, P. H. Phosphonate Coupling Molecules for the Control of Surface/Interface Properties and the Synthesis of Nanomaterials. *Dalt. Trans.* **2013**, *42* (35), 12569.
- (159) Brodard-Severac, F.; Guerrero, G.; Maquet, J.; Florian, P.; Gervais, C.; Mutin, P. H. High-Field ¹⁷O MAS NMR Investigation of Phosphonic Acid Monolayers on Titania. *Chem. Mater.* **2008**, *20* (16), 5191–5196.
- (160) Guerrero, G.; Mutin, P. H.; Vioux, A. Anchoring of Phosphonate and Phosphinate Coupling Molecules on Titania Particles. *Chem. Mater.* **2001**, *13* (11), 4367–4373.
- (161) Zorn, G.; Adadi, R.; Brener, R.; Yakovlev, V. A.; Gotman, I.; Gutmanas, E. Y.; Sukenik, C. N. Tailoring the Surface of NiTi Alloy Using PIRAC Nitriding Followed by Anodization and Phosphonate Monolayer Deposition. *Chem. Mater.* **2008**, *20* (16), 5368–5374.
- (162) Maho, A.; Kanoufi, F.; Combellas, C.; Delhalle, J.; Mekhalif, Z. Electrochemical Investigation of Nitinol/Tantalum Hybrid Surfaces Modified by Alkylphosphonic Self-Assembled Monolayers. *Electrochim. Acta* **2014**, *116*, 78–88.
- (163) Vanhooland, A.; Devillers, S.; Issakova, T.; Michaux, C.; Delhalle, J.; Mekhalif, Z. Electroassisted Auto-Assembly of Alkylphosphonic Acids Monolayers on Nitinol. *J. Electrochem. Soc.* **2016**, *163* (10), G173–G177.
- (164) Devillers, S.; Barthélémy, B.; Fery, I.; Delhalle, J.; Mekhalif, Z. Functionalization of Nitinol Surface toward a Versatile Platform for Post-Grafting Chemical Reactions.

- Electrochim. Acta* **2011**, *56* (24), 8129–8137.
- (165) Quiñones, R.; Garretson, S.; Behnke, G.; Fagan, J. W.; Mueller, K. T.; Agarwal, S.; Gupta, R. K. Fabrication of Phosphonic Acid Films on Nitinol Nanoparticles by Dynamic Covalent Assembly. *Thin Solid Films* **2017**, *642* (September), 195–206.
- (166) Szwarc, M. ‘Living’ Polymers. *Nature* **1956**, *178* (4543), 1168–1169.
- (167) Matyjaszewski, K.; Tsarevsky, N. V. Macromolecular Engineering by Atom Transfer Radical Polymerization. *J. Am. Chem. Soc.* **2014**, *136* (18), 6513–6533.
- (168) Khabibullin, A.; Mastan, E.; Matyjaszewski, K.; Zhu, S. Surface-Initiated Atom Transfer Radical Polymerization. In *Controlled Radical Polymerization at and from Solid Surfaces*; Vana, P., Ed.; Springer, 2016.
- (169) Braunecker, W. a.; Matyjaszewski, K. Controlled/Living Radical Polymerization: Features, Developments, and Perspectives. *Prog. Polym. Sci.* **2007**, *32*, 93–146.
- (170) Wang, J. S.; Matyjaszewski, K. Controlled/“Living” Radical Polymerization. Atom Transfer Radical Polymerization in the Presence of Transition-Metal Complexes. *J. Am. Chem. Soc.* **1995**, *117* (20), 5614–5615.
- (171) Kato, M.; Kamigaito, M.; Sawamoto, M.; Higashimura, T. Polymerization of Methyl Methacrylate with the Carbon Tetrachloride/Dichlorotris-(Triphenylphosphine)Ruthenium(II)/Methylaluminum Bis(2,6-Di-Tert-Butylphenoxide) Initiating System: Possibility of Living Radical Polymerization. *Macromolecules* **1995**, *28* (5), 1721–1723.
- (172) Xu, F. J.; Neoh, K. G.; Kang, E. T. Bioactive Surfaces and Biomaterials via Atom Transfer Radical Polymerization. *Prog. Polym. Sci.* **2009**, *34* (8), 719–761.
- (173) He, W.; Jiang, H.; Zhang, L.; Cheng, Z.; Zhu, X. Atom Transfer Radical Polymerization of Hydrophilic Monomers and Its Applications. *Polym. Chem.* **2013**, *4* (10), 2919–2938.
- (174) Matyjaszewski, K. Advanced Materials by Atom Transfer Radical Polymerization. *Adv. Mater.* **2018**, *30* (23), 1–22.
- (175) Bousquet, A.; Awada, H.; Hiorns, R. C.; Dagron-Lartigau, C.; Billon, L. Conjugated-Polymer Grafting on Inorganic and Organic Substrates: A New Trend in Organic Electronic Materials. *Prog. Polym. Sci.* **2014**, *39* (11), 1847–1877.
- (176) Hui, C. M.; Pietrasik, J.; Schmitt, M.; Mahoney, C.; Choi, J.; Bockstaller, M. R.; Matyjaszewski, K. Surface-Initiated Polymerization as an Enabling Tool for Multifunctional (Nano-)Engineered Hybrid Materials. *Chem. Mater.* **2013**, *26*, 745–762.

Chapter 2

Improving Nitinol biomedical properties: aim, strategies
& experimental section

2.1 Aim	43
2.2 Strategies	43
2.2.1. SI-ATRP of DMAEMA: a proof of concept	43
2.2.2. SI-ATRP of MPC: a further step towards biomedical	45
2.2.3. Use of bisphosphonic acids: an alternative to mixed SAMs	45
2.3 Experimental section	46
2.3.1. Pre-treatment of Nitinol plates.....	46
2.3.2. Substrates characterization.....	46
References	49

2.1 Aim

The overall objectives of the thesis rely upon the controlled synthesis of a biocompatible and hydrophilic polymer coating on Nitinol substrates, optimized for biomedical applications, especially for the preparation of cardiovascular stents. Such coating is considered and optimized to: (1) prevent Nitinol corrosion in physiological medium and avoid the release of cytotoxic Ni^{2+} ions; (2) improve its biocompatibility and decrease the risks of rejection; (3) allow to endothelialisation of the material; (4) prevent from restenosis; and (5) incorporate specific drugs.

2.2 Strategies

The scientific strategies elaborated to successfully reach those objectives are presented in three pathways (Figure 2.2): the thermally- and electro-assisted grafting of SI-ATRP initiating layer on Nitinol and its subsequent polymerization of a model monomer as a proof of concept (Chapter 4); the elaboration of a biocompatible film on mixed initiating monolayers (Chapter 5) and its biological effects (Chapter 6); and the grafting of bisphosphonic acid derivatives as an alternative to mixed SAMs (Chapter 7). All these treatments have been performed on priorly hydrothermally treated Nitinol, which is used as a first reinforcement procedure (Chapter 3).

2.2.1. SI-ATRP of DMAEMA: a proof of concept

This part is devoted to the elaboration of monomolecular SI-ATRP initiating layer made of 11-(2-bromoisobutyrate)-undecyl-1-phosphonic acid (BUPA, Figure 2.1a) in mild conditions to prevent its degradation. This molecule is selected for a double purpose: it will act as SI-ATRP initiator as it is bearing a bromoisobutyrate group commonly used in ATRPs and is also expected to improve Nitinol corrosion resistance by forming organized layers.

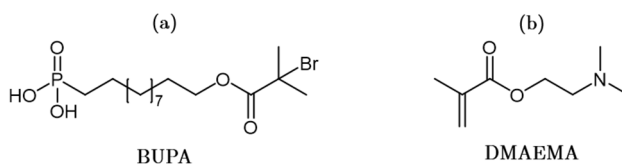


Figure 2.1. Chemical structures of 11-(2-bromoisobutyrate)-undecyl-1-phosphonic acid (a) and 2-(dimethylamino)ethyl methacrylate (b).

In this respect and considering the long modification times usually required to obtain densely formed monolayers, two processes, *i.e.* the electro- and thermally-assisted self-assembling of BUPA, are selected and compared to the classical immersion process on Nitinol surfaces initially hydrothermally treated.

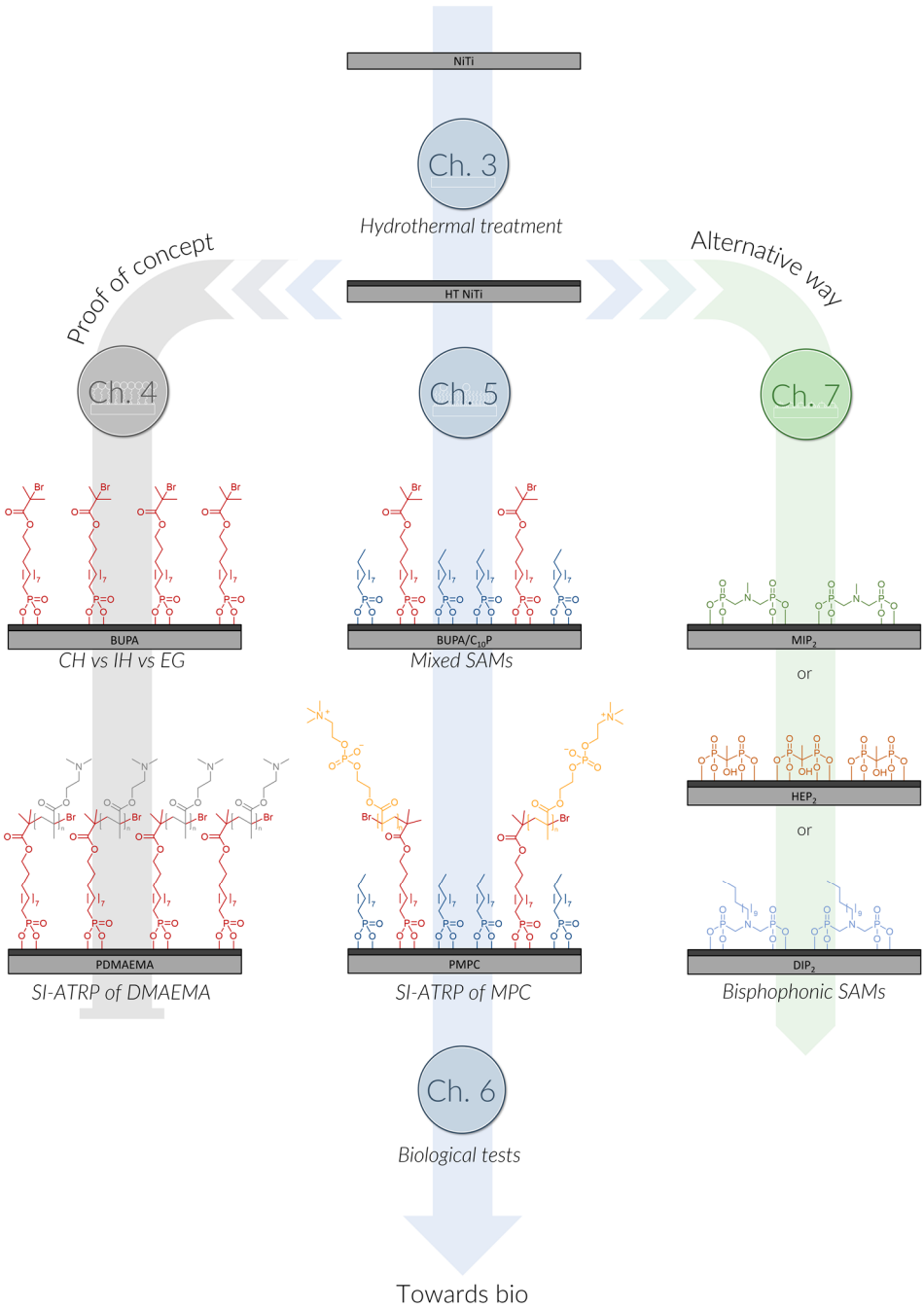


Figure 2.2. Schematic representation of the Nitinol surface modification strategies assessed in this work

The so-formed BUPA-covered Nitinol substrates are then used for SI-ATRP of 2-(dimethylamino)ethyl methacrylate (DMAEMA, Figure 2.1b) as a test monomer to ensure the quality and the usability of the initiation layer.

2.2.2. SI-ATRP of MPC: a further step towards biomedical

The ATRP initiating group worn by BUPA being bulky, the use of such molecule may lead to the formation of disordered and less protective layer. In order to improve the inhibiting behaviour of the initiating layer, this part focuses on the use of mixed monolayers resulting from the co-adsorption of two organophosphonic acid derivatives differing in length. In this respect, 1-decylphosphonic acid ($C_{10}P$, Figure 2.3a) has been selected as a spacer that can intercalate into the BUPA layer to increase its density and its protective effects. The influence of various BUPA/ $C_{10}P$ ratios are assessed and compared.

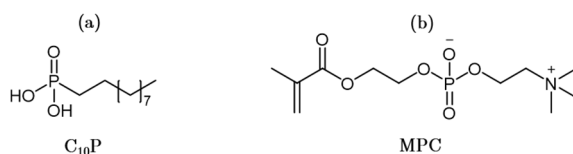


Figure 2.3. Chemical structures of 11-decylphosphonic acid (a) and 2-methacryloyloxyethyl phosphorylcholine (b).

The best condition among the so-formed layers is then used to initiate the surface polymerization of a biocompatible monomer, 2-methacryloyloxyethyl phosphorylcholine (MPC, Figure 2.3b). This poly-MPC (PMPC) coating is then finally submitted to corrosion tests in blood plasma simulated fluid and to endothelial cells growth.

2.2.3. Use of bisphosphonic acids: an alternative to mixed SAMs

This section investigates the grafting of short tail mono- and bisphosphonic acid derivatives as an alternative to mixed monolayers. For this purpose, surface modifications based on bisphosphonic acid derivatives have been assessed and compared to a monophosphonic acid derivative. Five molecules have been selected: methylphosphonic acid (Figure 2.4a) (methylimino)dimethylene-bisphosphonic acid (Figure 2.4b) and 1-hydroxyethylidene-1,1-diphosphonic acid (Figure 2.4c)

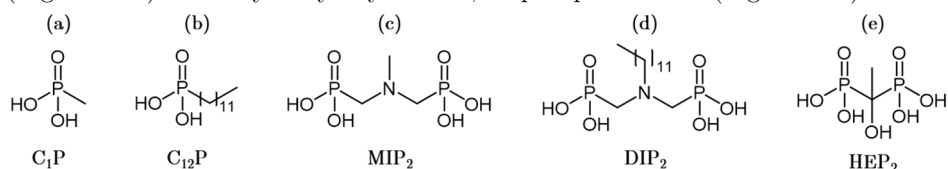


Figure 2.4. Chemical structures of methylphosphonic acid (a), dodecylphosphonic acid (b), (methylimino)dimethylene-bisphosphonic acid (c), (dodecylimino)dimethylene-bisphosphonic acid (d), and 1-hydroxyethylidene-1,1-diphosphonic acid (e).

2.3 Experimental section

2.3.1. Pre-treatment of Nitinol plates

Nitinol (Ni 56% / Ti 44%) rectangular-shaped plates (20 mm × 10 mm × 0.3 mm), purchased from AMF, are mechanically polished (Buehler Ecomet 300 instrument) down to 0.1 μm roughness on silicon carbide papers using diamond pastes (9 μm) (Struers), a mixture of colloidal silica (Buehler MasterMet™ 2) and H₂O₂ (Acros Organics, 35 wt.% solution in water).

Nitinol substrates are cleaned in denatured ethanol under ultrasonication for 15 min, blown dried with nitrogen and stored under nitrogen. Such samples are referred to as Bare in the sequel, whereas the samples submitted to a 1 h treatment in boiling water are called HT.

2.3.2. Substrates characterization

The modified substrates are characterized by X-ray photoelectron spectroscopy (XPS), polarization modulation-infrared reflection-absorption spectroscopy (PM-IRRAS), static water contact angle measurements (WCA), cyclic voltammetry (CV), linear sweep (LSV) voltammetry, scanning electrochemical microscopy (SECM) and electrochemical impedance spectroscopy (EIS). To assess the reproducibility of experiments, all analyses are performed in triplicate. In the case of XPS characterizations, each sample is analyzed at three different locations.

XPS spectra are recorded on a Thermo Scientific K-Alpha spectrometer with a monochromatized X-ray K_α radiation (1486.6 eV), the photoelectrons are collected at 0° with respect to the surface normal and detected with a hemispherical analyzer. The X-ray source spot size on the sample is 200 μm. The analyzer is operated with 200 eV and 50 eV as pass energy for the survey and the high-resolution core levels spectra, respectively. The core levels binding energy (BE) are calibrated with respect to the C1s BE set at 285.0 eV. Spectra are analyzed using a linear combination of Gaussian and Lorentzian curves in a 70/30 ratio. The peak areas are measured on core levels spectra. Quantitative XPS analyses are carried out by calculating the relevant abundance ratios on the basis of the core levels spectra and taking into account the corresponding Scofield sensitivity factors:¹ C1s 1.000, O1s 2.930, P2p 1.920, N1s 1.800, Ti2p 7.910 and Ni2p 22.180. Thickness of the formed coatings are estimated from the collected XPS data.

The **thickness** of a first material (*i.e.* SAM) deposited on a bulk material (*i.e.* NiTi) can be obtained from the relative attenuation of this bulk material (here limited to Ti), by the formula:

$$\frac{I_{Ti}}{I_{Ti,0}} = \exp\left(-\frac{d_{SAM}}{\lambda_{Ti,SAM}} \sin \theta\right) \quad (\text{Eq. 2.1.})$$

where $I_{Ti}/I_{Ti,0}$ is the ratio of the bulk element peak intensities (modified/bare surface), d_{SAM} the coating thickness, $\lambda_{Ti,SAM}$ the bulk Ti photoelectrons mean free path through the SAM layer, and θ the takeoff angle (here $\theta=90^\circ$).

Depth profile analyses of the oxidized layers are performed by sputtering an area of 1 mm * 1 mm using an Ar⁺ ion beam with an energy of 0.5 or 2 keV. The depth profiles results from the combination of 20 levels of 1 s sputtering followed by 10 levels of 5 s sputtering.

PM-IRRAS data are collected to assess the presence of the organic layer on Nitinol surfaces. They are recorded on a Bruker PMA37 equipped with a liquid nitrogen cooled mercury-cadmium-telluride (MCT) detector and a germanium crystal. All presented spectra are the average of 1024 scans at a resolution of 4 cm⁻¹.

Static water contact angles are measured using a DIGIDROP (GBX Surface Technology) goniometer at room temperature and ambient atmosphere, with a syringe to deliver 2 μ L milli-Q water droplets.

Voltammetry measurements (CV and LSV) are carried out on a Princeton Applied Research, Potentiostat/Galvanostat Model Versastat 3-LC using a three-electrodes electrochemical cell with a controlled analysis spot surface (0.28 cm²) on the sample. Nitinol substrates (bare or modified) are used as working electrode, a platinum foil as counter electrode and a saturated calomel electrode (SCE) as reference. The corrosion inhibition efficiency can be determined by the formula:

$$IE = \frac{j_{corr,0} - j_{corr}}{j_{corr,0}} 100 \quad (\text{Eq. 2.2.})$$

where $j_{corr,0}$ and j_{corr} are the corrosion current densities of bare and modified NiTi substrates, respectively.

Cyclic voltammograms are recorded from -0.10 to +0.65 V at a scan rate of 20 mV s⁻¹ in 0.1 M NaOH linear sweep voltammograms are recorded from 200 mV below OCP (measured for 1 h) to + 1.0 V at a scan rate of 1 mV/s in 0.5 M NaCl. The blocking factor of the coatings on NiTi (Table 2) are determined from the obtained anodic area (a_{an}) by the formula:

$$BF = \frac{a_{an,0} - a_{an}}{a_{an,0}} 100 \quad (\text{Eq. 2.3.})$$

where $a_{an,0}$ and a_{an} are the area of the anodic peaks for the first cycle of bare and modified NiTi substrates, respectively.

EIS measurements are carried out in the frequency range of 10 kHz to 0.1 Hz at an amplitude of 10 mV peak to peak. The obtained EIS data are presented in Nyquist representation and are fitted to the electrical equivalent circuit shown in Figure 2.5, where R_{el} , R_{ct} and R_{ox} are the resistances of the electrolyte, of charge transfer and of the oxide layer, respectively, and where Q_{dl} and Q_{ox} are the constant phase element (CPE) of the electrochemical double layer and of the oxide.

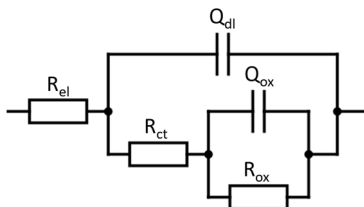


Figure 2.5. Electrical equivalent circuit used for the modeling of Nitinol.

The impedance of CPE, used to replace the capacitance element in non-ideal cases, is defined as:

$$Z_{CPE} = \frac{1}{Q(j\omega)^n} \quad (\text{Eq. 2.4.})$$

where Q is a frequency-independent parameter of the CPE. Deviation of the exponent n from ideal value $n=1$ indicates the presence of inhomogeneity at the solid/electrolyte interface caused by roughness.²

SECM is used in feedback (FB) mode on a CHI 900B Potentiostat (CH Instruments) using a three-electrodes cell with a commercial Ag|AgCl reference electrode (CHI111, CH Instruments), a platinum foil as counter electrode and a 10 μm diameter platinum microdisc ultramicroelectrode (UME) with an estimated RG ratio of 8 as the working electrode. The sample is fixed to the bottom of the cell at open circuit. Analyses in the FB mode are performed in a 1 mM FcMeOH/0.1M KNO_3 aqueous solution according the following procedure: the UME is polarized at 0.40 V *vs* Ag-AgCl to allow for the mass-transfer controlled oxidation of FcMeOH into ferriceniummethanol (FcMeOH^+) and is moved down to the substrate at a rate of $1\mu\text{m s}^{-1}$. The approach curve is recorded until a sharp change of the currents occurs at the tip, as the result of a contact between the sample and the UME. The UME is then withdrawn by 3 μm and the imaging measurement is performed on a $500 \times 500 \mu\text{m}^2$ area at a scan rate of $25 \mu\text{m s}^{-1}$.

The amount of released nickel after immersion in physiological media is determined by ICP-OES using a Optima 8000 spectrometer (Perkin Elmer)

The optimized molecular geometries of BUPA, C_{10}P , C_1P , HEP_2 and MIP_2 were obtained by the molecular editor Avogadro using the molecular mechanics force field MMFF94.

References

- (1) *Handbook of X-Ray Photoelectron Spectroscopy*; Chastain, J., Ed.; Perkin Elmer Corporation: USA, 1992.
- (2) Lukács, Z. Evaluation of Model and Dispersion Parameters and Their Effects on the Formation of Constant-Phase Elements in Equivalent Circuits. *J. Electroanal. Chem.* **1999**, *464* (1), 68–75.

Chapter 3

Hydrothermal reinforcement of Nitinol oxide layer: a first barrier against
surface corrosion

3.1	Introduction	53
3.2	Composition of native and hydrothermally treated Nitinol surfaces	53
	3.2.1. Impact of the hydrothermal treatment on NiTi oxide composition ..	54
	3.2.2. Samples ageing and oxides stability	58
3.3	Electrochemical behaviour of bare and hydrothermally treated Nitinol	60
3.4	Conclusions	62
	References	62

3.1 Introduction

Although it is a nearly equiatomic binary alloy, NiTi native oxide layer is mainly made of TiO_2 as its formation from Ti is thermodynamically more favorable than that of NiO with respective free energy of formation (ΔG) values of -888.8 and -211.7 kJ mol^{-1} .^{1,2} However, Nitinol corrosion remains of concern due to some nickel inclusions present at the surface. Within the purpose of improving its corrosion resistance, several NiTi surface modification have been studied during the last two decades, *e.g.* exposure to air, wet and dry heat treatments, or (electro)chemical modification.²⁻⁹

From the early 2000's, several teams intensively investigated the corrosion resistance of Nitinol native oxide as well as the impact of those processes on NiTi oxide thickness and corrosion resistance. Among them, it was demonstrated that wet and dry heat treatment on polished substrates are beneficial in a large range of temperatures and improve nitinol corrosion resistance by increasing its oxide layer thickness and decreasing the amount of nickel in the outer layer.^{7,9,10} This phenomenon is almost exclusively related to the increase in the thickness of TiO_2 resulting from the inward diffusion of O atoms and outward migration of Ni atoms eased by the temperatures.^{7,10} During hydrothermal treatment, Ni atoms can diffuse outward the oxide layer towards both the its external surface, thus being released from the material, or towards the oxide/metal interface, thus forming an underlying Ni-rich layer.⁷⁻¹⁰ Despite it has been proven that the passive layer tends to increase with the temperature, Bellini *et al.* recently demonstrated the partial loss of shape memory and superplastic properties of NiTi above 400°C.¹¹ The hydrothermal treatment of NiTi in boiling water for 1h remains of interest due to its less aggressive conditions.

The aim of the present chapter is to describe not only the impact of hydrothermal treatment over the thickness of Nitinol oxide layer, but also the changes in its composition and its stability over time (up to 9 weeks) once exposed to air. The second part is devoted to the assessment of the electrochemical characteristics of both oxides by cyclic voltammetry, linear sweep voltammetry and electrochemical impedance spectroscopy.

3.2 Composition of native and hydrothermally treated Nitinol surfaces

The compositions of the native (Bare) and the hydrothermally treated (HT) NiTi oxide layers can be determined through the shape of Ti2p and Ni2p_{3/2} (Figure 3.1b) XPS core spectra which result from the combination of peaks at different

oxidation states. In the case of Ti2p (Figure 3.1a), those peaks, at energies of 454.0 eV (460.2 eV), 455.5 eV (461.3 eV), 456.9 eV (462.9 eV) and 458.6 eV (464.7 eV) corresponds respectively to Ti atoms at oxidation state 0, II, III or IV,¹² whereas in the case of Ni2p_{3/2}, the peaks at energies of 852.4 eV, 856.0 eV and 859.9 eV corresponds respectively to Ni atoms at oxidation state 0 and I or to nickel plasmons.¹³

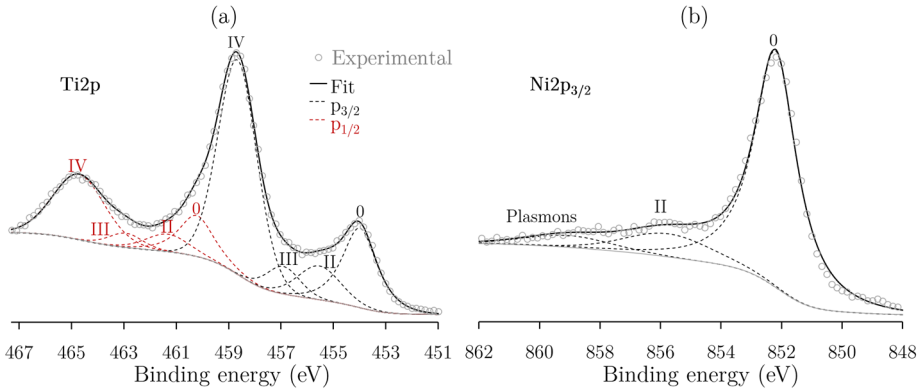


Figure 3.1. Representative XPS core spectra for Ti2p (a) and Ni2p_{3/2} (b) components obtained for Bare-NiTi and HT-NiTi.

3.2.1. Impact of the hydrothermal treatment on NiTi oxide composition

First of all, SEM images indicate that the morphology of Nitinol is not affected by the hydrothermal treatment (Figure 3.2).

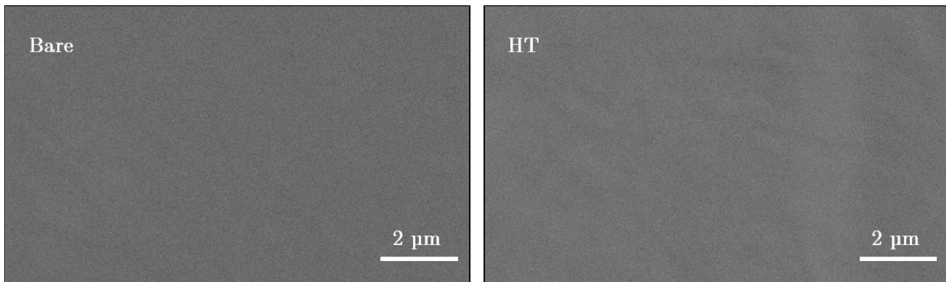


Figure 3.2. SEM images for Bare-NiTi and HT-NiTi (obtained in secondary electron imaging mode).

The atomic ratios obtained from the XPS measurements of Bare-NiTi showed that the sample surface is covered by a thin oxide layer through which the metallic substrate is detectable. This passive layer is mainly composed of titanium oxides (especially TiO₂ - Table 3.1) and is relatively depleted in Ni. As expected, the hydrothermal treatment of NiTi increases its oxide thickness and decreases the amount of Ni on the surface as depicted by O/NiTi and Ni/NiTi ratios (Table 3.1) and this oxide mainly results from the oxidation of Ti (0, II and III) to Ti (IV).

The water contact angles measurements made on both materials point out to an increased hydrophilicity of HT-NiTi compared to Bare-NiTi with values of 32.0° and 57.0° , respectively. This phenomenon attests the hydroxylation of the surface which will be an asset for the grafting of phosphonic acid derivatives.

Table 3.1. XPS atomic ratios for Bare-NiTi and HT-NiTi before etching.

	O/NiTi	Ni/NiTi	Ti ⁴⁺ /Ti	Ti ³⁺ /Ti	Ti ²⁺ /Ti	Ti ⁰ /Ti
Bare	1.33 ± 0.02	0.42 ± 0.01	0.61 ± 0.03	0.07 ± 0.01	0.06 ± 0.01	0.27 ± 0.01
HT	2.64 ± 0.04	0.06 ± 0.01	0.91 ± 0.01	0.02 ± 0.00	0.02 ± 0.00	0.05 ± 0.01

The impact of the hydrothermal treatment on the oxide layer depth can be assessed by etching the surface with Ar⁺ ions and characterized the inner layers.

On the obtained depth profile for Bare-NiTi (Figure 3.3), it is seen that some carbon contaminations are present on the surface but are quickly removed. The oxygen concentration progressively decreases to reach a minimum value close to 0% around 30 s of sputtering. The titanium concentration exhibits a minimum area (down to 24%) between 10 s and 20 s of sputtering, which is also the region where the nickel concentration reaches a maximum (up to 64%) and where the oxide has almost disappeared. This suggest the presence of a nickel-enriched layer under the passive layer. Nickel and titanium then progressively reach steady-state values of respectively 60% and 31%, due to a preferential sputtering of Ti. This phenomenon, already noticed in the literature,^{3,10} is due to difference between Ni and Ti sputter yield, *i.e.* the number of atom ejected from the material per striking argon ion, with respective values of 1.098 and 0.469 at 500 eV (values determined online by a sputter yield calculator¹⁴ based on the work of Matsunami *et al.*¹⁵).

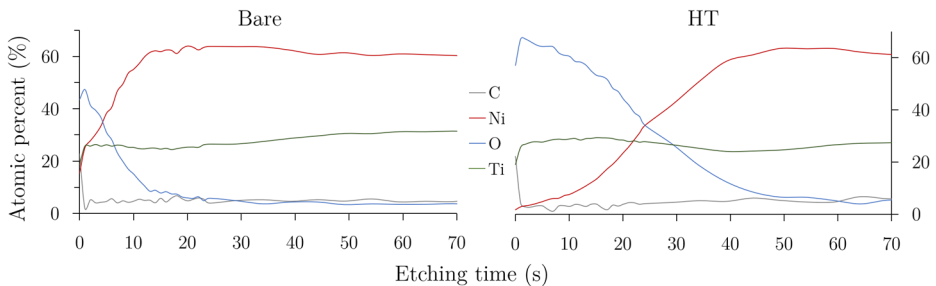


Figure 3.3. Depth profile of Bare-NiTi and HT-NiTi sputtered by Ar ions at 0.5 keV on an area of 1 mm².

After the hydrothermal treatment (HT-NiTi), the amount of O on the surface increase from 47% to 67%, whereas the amount of Ni decreases from 15% to 3% (Figure 3.3), as expected. On the corresponding depth profile, it is seen that the oxygen is detected until ~ 50 s of etching, whereas Ni only starts to be significantly

detected after ~ 20 s. This corresponds to an increased thickness of the oxide layer, which is depleted in Ni. A nickel-enriched layer can nevertheless still be noticed, but deeper in the material, between 40 s and 60 s of sputtering, with a maximum value of 63%.

The discrimination between oxidized and metallic Ni and Ti atoms can be further investigated on the 3D evolution of O1s, Ti2p and Ni2p_{3/2} spectrum with the etching time (Figure 3.4). Such representation confirms the major presence of Ti⁰, as well as a very low amount of Ni within the oxide layer for the shortest etching times. This observation is amplified for HT-NiTi, as expected. However, the low amount of Ni at the surface does not allow the discrimination of the oxidized and metallic components.

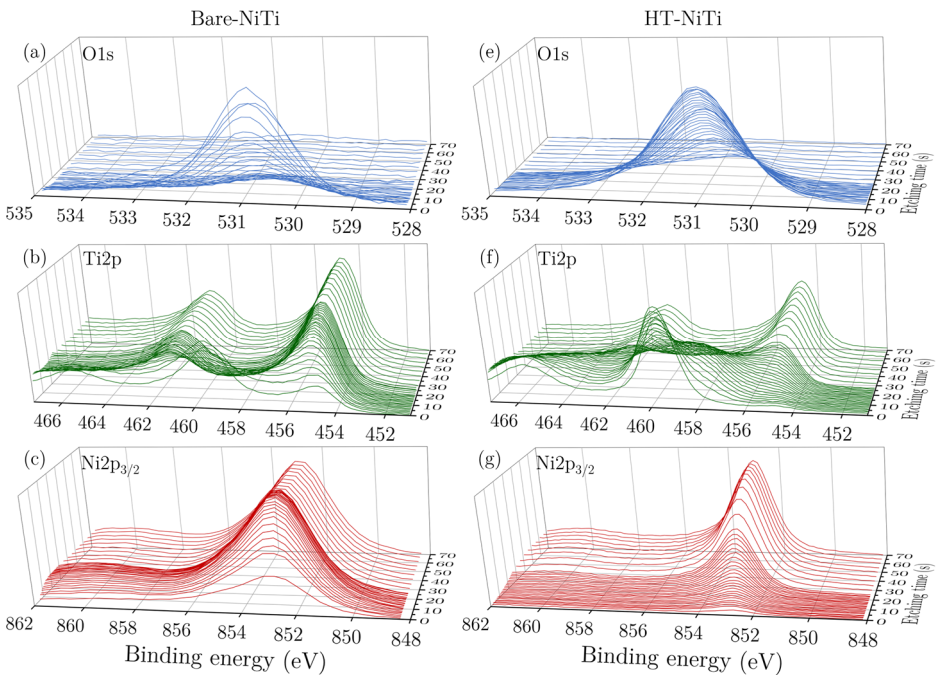


Figure 3.4. Depth evolution of oxygen (a, e), titanium (b, f) and nickel (c, g) for Bare-NiTi (a-c) and HT-NiTi (e-g) sputtered by Ar ions at 0.5 keV on an area of 1 mm².

In 1994, Viefhaus *et al.* presented a methodology based on Auger Electron Spectroscopy depth profiles to determine the location of the interface between the oxidized and the non-oxidized areas. They stated that the composition broadening at an interface obeys an error function characterized by a standard deviation σ , and thus the position of this interface corresponds to the duration of sputter time for the decrease of the signal from 84% to 16% of its constant height, as schematized on Figure 3.5.¹⁶

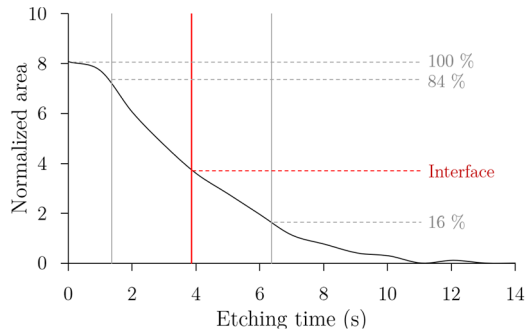


Figure 3.5. Schematic representation of the method used to determine the interface position and error limits (based on Viehhaus *et al.*).¹⁶

Transposed to the XPS spectra from Figure 3.4, this methodology can be used on Bare-NiTi and HT-NiTi surfaces to determine the oxide/metal interface, the composition of the oxide layer in Ti (IV, III and II), as well as the depth of the nickel-containing layer (Figure 3.6).

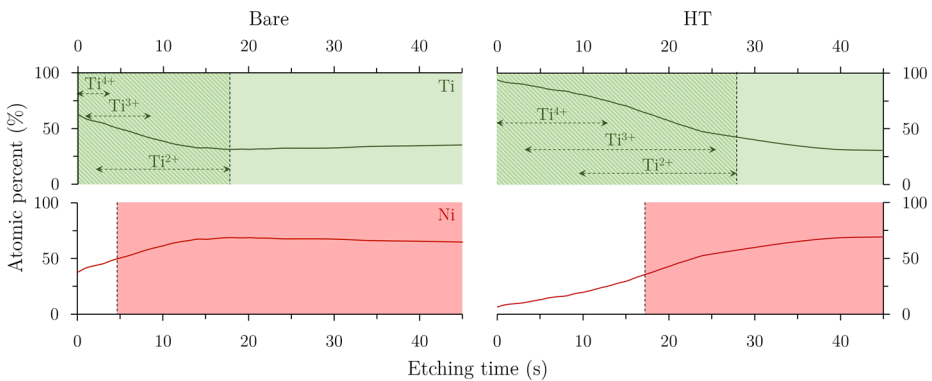


Figure 3.6. Approximated surface composition of Bare-NiTi and HT-NiTi (based on XPS depth profiles).

As expected, the external surface of Bare-NiTi is mainly composed of titanium oxides, especially TiO_2 (Table 3.1), and the oxide/metal interface is reached after approximately 18 s of etching, whereas the nickel-containing area is reached after 5 s. The deeper oxide layer is mainly composed of lower oxidized Ti atoms (*i.e.* III and II), which corresponds to Ti_2O_3 and TiO , respectively.

After hydrothermal treatment (HT-NiTi), the oxide thickness is increased and its composition is enriched in TiO_2 at the surface, in Ti_2O_3 in the bulk but depleted in nickel. The oxide/metal interface is reached after 28 s of etching, which is almost twice longer as for Bare-NiTi, whereas the nickel containing area is only reached after 17 s. Those results are in line with the mechanism proposed in the literature, *i.e.* the outward diffusion of Ni and the inward diffusion of O, and are confirmed by the atomic ratios (Table 3.1).

3.2.2. Samples ageing and oxides stability

This section focuses on the stability of Bare-NiTi and HT-NiTi in atmospheric conditions. In this context, the evolution of XPS atomic ratios for Bare-NiTi and HT-NiTi aged for up to 9 days are presented in Table 3.2 and Table 3.3, respectively. Despite a small increase of O/NiTi and Ni/NiTi ratios and an increase of Ti⁴⁺/Ti within the first day, attributed to the oxygen diffusion, Bare-NiTi does not seem to be affected by the exposure time, and thus quickly reaches its stable conformation. The same tendency can be seen for HT-NiTi but with a stabilization appearing after 2 days of ageing.

Table 3.2. XPS atomic ratios for Bare-NiTi aged from 0 (D₀) to 9 days (D₉).

	O/NiTi	Ni/NiTi	Ti ⁴⁺ /Ti	Ti ³⁺ /Ti	Ti ²⁺ /Ti	Ti ⁰ /Ti
D ₀	1.33 ± 0.02	0.42 ± 0.01	0.61 ± 0.03	0.07 ± 0.01	0.06 ± 0.01	0.27 ± 0.01
D ₁	1.55 ± 0.03	0.36 ± 0.02	0.70 ± 0.01	0.05 ± 0.02	0.05 ± 0.02	0.20 ± 0.03
D ₂	1.52 ± 0.05	0.34 ± 0.01	0.67 ± 0.02	0.05 ± 0.00	0.05 ± 0.02	0.21 ± 0.05
D ₃	1.54 ± 0.02	0.32 ± 0.01	0.72 ± 0.01	0.05 ± 0.01	0.04 ± 0.01	0.20 ± 0.04
D ₉	1.82 ± 0.03	0.34 ± 0.03	0.73 ± 0.01	0.06 ± 0.01	0.06 ± 0.02	0.13 ± 0.01

Table 3.3. XPS atomic ratios for HT-NiTi aged from 0 (D₀) to 9 days (D₉).

	O/NiTi	Ni/NiTi	Ti ⁴⁺ /Ti	Ti ³⁺ /Ti	Ti ²⁺ /Ti	Ti ⁰ /Ti
D ₀	2.60 ± 0.04	0.10 ± 0.01	0.89 ± 0.01	0.02 ± 0.00	0.02 ± 0.00	0.05 ± 0.01
D ₁	2.64 ± 0.02	0.05 ± 0.02	0.91 ± 0.02	0.02 ± 0.00	0.02 ± 0.02	0.07 ± 0.02
D ₂	2.74 ± 0.03	0.06 ± 0.01	0.92 ± 0.03	0.02 ± 0.01	0.02 ± 0.01	0.05 ± 0.01
D ₃	2.73 ± 0.03	0.05 ± 0.01	0.92 ± 0.01	0.03 ± 0.01	0.01 ± 0.00	0.04 ± 0.01
D ₉	2.75 ± 0.03	0.07 ± 0.03	0.88 ± 0.04	0.02 ± 0.01	0.02 ± 0.01	0.04 ± 0.01

The oxide/metal interface, the beginning on the Ni-containing layer as well as the oxidation states of Ti atoms in the oxide layer for aged Bare-NiTi and HT-NiTi have been determined following the methodology presented above (Figure 3.7).

The composition profiles obtained for aged Bare-NiTi confirms the stability of its oxide over time with the oxide/metal interface detected at ~ 18 s for all substrates. As previously presented, this oxide layer remains mainly composed of TiO₂ and depleted in nickel. However, a Ni-containing layer limit is still detected deeper in the material surface until 2 days of exposure, in a range of 5 s to 7 s of etching and remains stable afterwards. In contrast, the composition profiles of aged HT-NiTi point out to diffusion of O and Ni until 3 days of exposure. Indeed, the oxide/metal interface is detected after 43 s of etching instead of the initial value of 28 s and the required etching time to detect the Ni-containing layer falls down to ~ 26 s instead of 17 s. Even if HT-NiTi seems to be sensitive to the atmospheric exposure in the

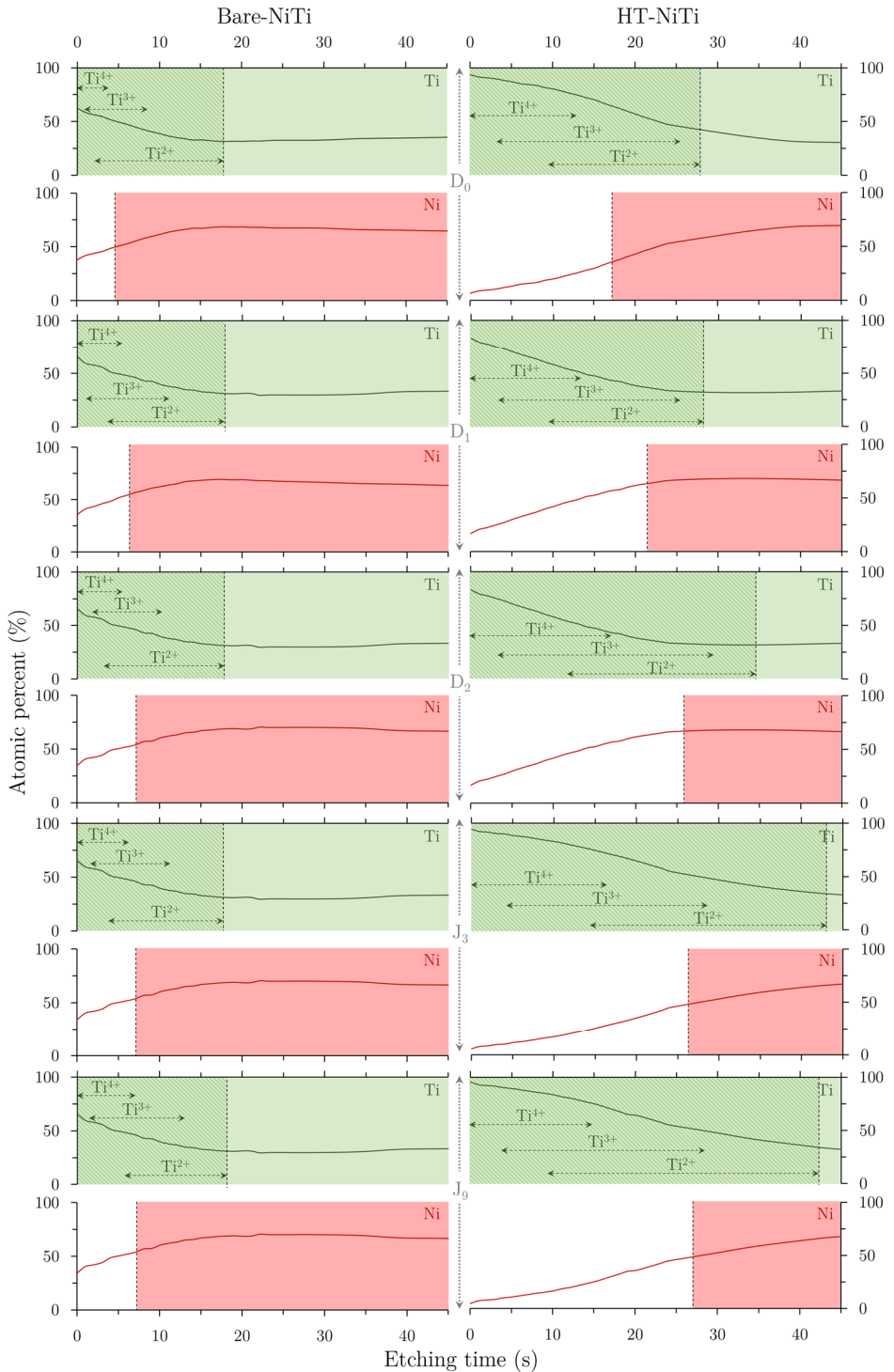


Figure 3.7. Approximated surface composition of aged Bare-NiTi and HT-NiTi (based on XPS depth profiles).

studied range of time, the evolution of its composition is beneficial for its passivation and the reduction of nickel in its outer surface.

3.3 Electrochemical behaviour of bare and hydrothermally treated Nitinol

Electrochemical evaluation of HT-NiTl is compared to Bare-NiTl on the basis of four methods, *i.e.* cyclic voltammetry (Figure 3.8), scanning electrochemical microscopy (Figure 3.9), linear sweep voltammetry and electrochemical impedance spectroscopy (Figure 3.10).

Cyclic voltammetry (CV) (Figure 3.8) confirms the reinforcement of the TiO_2 external layer. For Bare-NiTl, the first cycle (Figure 3.8a) reveals two anodic peaks at 200 and 500 mV *vs* SCE, respectively assigned to Ti^{n+} and Ni^{2+} oxidations but only one cathodic peak assigned to Ni^{3+} reduction. On the second cycle (Figure 3.8b), only nickel oxidation and reduction peaks are still present due to the irreversible passivation of the electrode via the titanium oxide layer. For HT-NiTl, only the oxidation peak of Ti^{n+} can be observed on the first cycle and no more Ni reactions, even during the second cycle.

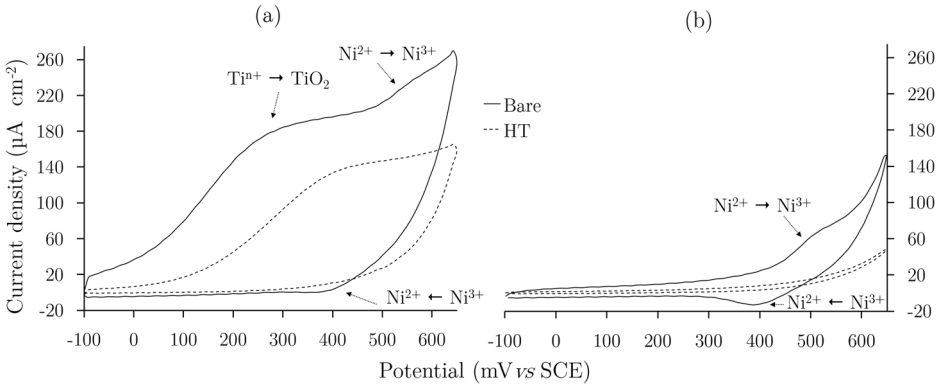


Figure 3.8. Representative first (a) and second (b) cycles of the voltammograms for Bare-NiTl and HT-NiTl in 0.1 M NaOH at a scan rate of 20 mV s⁻¹.

Those observations, as well as a blocking factor of 46.4% (Table 3.4) confirm the efficiency of the hydrothermal treatment on the reinforcement of TiO_2 oxide layer and on the prevention of Ni^{x+} release.

Table 3.4. Values of E_{corr} , j_{corr} , IE, BF and k_{ct} for Bare-NiTl and HT-NiTl.

	BF (%)	k_{ct} ($\mu\text{m s}^{-1}$)	IE (%)	R_{ox} ($\text{k}\Omega \text{cm}^{-2}$)	R_{ct} ($\text{M}\Omega \text{cm}^{-2}$)
Bare-NiTl	-	16.0 ± 1.3	-	94.3 ± 7.5	130.0 ± 1.2
HT-NiTl	46.4 ± 11.0	10.8 ± 1.1	88.1 ± 2.6	$2\,900.0 \pm 231.8$	707.0 ± 7.1

SECM is used to assess the charge transfer process occurring at Bare-NiTi and HT-NiTi electrodes during the reduction of FcMeOH^+ . Figure 3.9 shows the normalized approach curves in feedback (FB) mode. The curves are fitted on general analytical expressions given for first-order heterogenous finite kinetics^{17,18} at the sample surface with respect to the FcMeOH^+ generated at the tip surface. The apparent charge transfer rate constants (k_{ct} - Table 3.4) attest the regeneration rate of FcMeOH by HT-NiTi is lower than the one of Bare-NiTi. The obtained values of k_{ct} are in line with the results presented for CV. Indeed, the hydrothermal passivation of NiTi leads to the formation of a more protective oxide layer, as attested by a k_{ct} down from 16.0 to 10.8 $\mu\text{m s}^{-1}$.

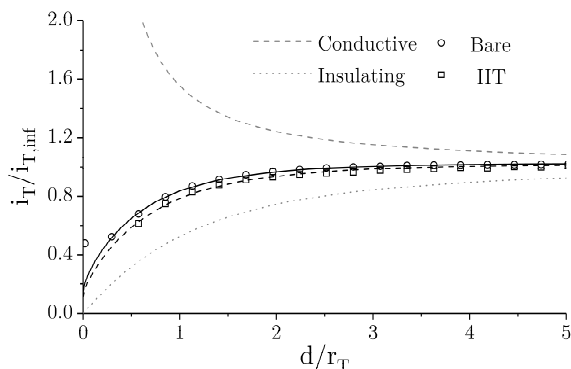


Figure 3.9. Representative normalized SECM FB approach curves for Bare-NiTi ($k_{\text{ct}}=15.3$) and HT-NiTi ($k_{\text{ct}}=11.2$) in 1 mM FcMeOH / 0.1 M KNO_3 . The tip was set at 0.4 V vs Ag|AgCl and moved at a scan rate of 1 $\mu\text{m s}^{-1}$. The symbols correspond to the experimental curves and the solid lines to the SECM theory.^{17,18}

The LSV results point out to the impact of the oxide layer reinforcement on the corrosion resistance of HT-NiTi, as shown in Figure 3.10 and Table 3.4. The hydrothermal treatment decreases the corrosion current densities with an inhibition efficiency (IE) of 88.1% comparatively to Bare-NiTi.

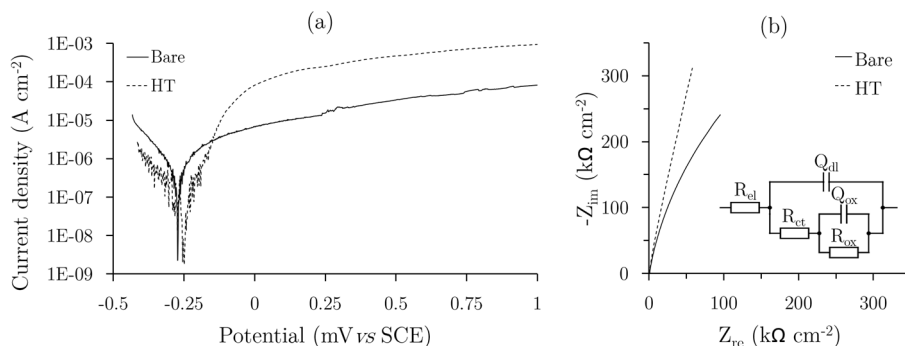


Figure 3.10. Representative polarization curves (a) and impedance spectra (b) of Bare-NiTi and HT-NiTi in 0.5 M NaCl at a scan rate of 1 mV s^{-1} .

This results from the increased resistances of the oxide layer (R_{ox}) and of charge transfer (R_{ct}) from respectively $94.3 \text{ k}\Omega \text{ cm}^{-2}$ and $130.0 \text{ k}\Omega \text{ cm}^{-2}$ to $2\,900.0$ and $\text{k}\Omega \text{ cm}^{-2}$ and $707.0 \text{ k}\Omega \text{ cm}^{-2}$ as attested by the EIS measurements (Figure 3.10 and Table 3.4).

3.4 Conclusions

The corrosion resistance of Nitinol has been improved by hydrothermal treatment, *i.e.* by boiling it in water during 1 h. It has been proven that the composition of such substrate was chemically reinforced in TiO_2 and depleted of Ni, which should decrease the risks of corrosion and prevent from the release of Ni^{2+} .

The impact of the treatment on the electrochemical behavior of Nitinol has been assessed by different methods (CV, LSV, EIS and SECM) which all pointed out the increased passivity of the oxide layer and its corrosion resistance.

However, even if the process is of interest to reinforce Nitinol corrosion resistance, the application of such Nitinol surfaces is still controversial and requires further surface modifications, *e.g.* the elaboration of protective organic coatings which will be developed in the following chapters.

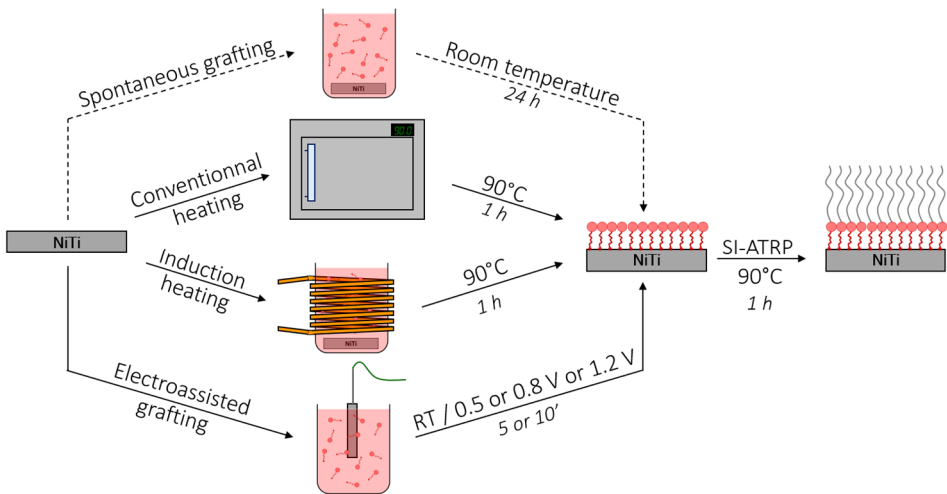
References

- (1) Haynes, W. M.; Lide, D. R.; Bruno, T. J. *CRC Handbook of Chemistry and Physics*, 2016.
- (2) Shabalovskaya, S. A.; Rondelli, G. C.; Undisz, A. L.; Anderegg, J. W.; Burleigh, T. D.; Rettenmayr, M. E. The Electrochemical Characteristics of Native Nitinol Surfaces. *Biomaterials* **2009**, *30* (22), 3662–3671.
- (3) Firstov, G. ; Vitchev, R. ; Kumar, H.; Blanpain, B.; Van Humbeeck, J. Surface Oxidation of NiTi Shape Memory Alloy. *Biomaterials* **2002**, *23* (24), 4863–4871.
- (4) Shabalovskaya, S. A.; Tian, H.; Anderegg, J. W.; Schryvers, D. U.; Carroll, W. U.; Van Humbeeck, J. The Influence of Surface Oxides on the Distribution and Release of Nickel from Nitinol Wires. *Biomaterials* **2009**, *30* (4), 468–477.
- (5) Simka, W.; Kaczmarek, M.; Baron-Wiecheć, A.; Nawrat, G.; Marciniak, J.; Źak, J. Electropolishing and Passivation of NiTi Shape Memory Alloy. *Electrochim. Acta* **2010**, *55* (7), 2437–2441.
- (6) Milošev, I.; Kapun, B. The Corrosion Resistance of Nitinol Alloy in Simulated Physiological Solutions Part 1: The Effect of Surface Preparation. *Mater. Sci. Eng. C* **2012**, *32* (5), 1087–1096.
- (7) Milošev, I.; Kapun, B. The Corrosion Resistance of Nitinol Alloy in Simulated Physiological Solutions Part 2: The Effect of Surface Treatment. *Mater. Sci. Eng. C* **2012**, *32* (5), 1068–1077.
- (8) Undisz, A.; Schrepel, F.; Wesch, W.; Rettenmayr, M. Mechanism of Oxide Layer Growth during Annealing of NiTi. *J. Biomed. Mater. Res. - Part A* **2012**, *100 A* (7),

- 1743–1750.
- (9) Ohtsu, N.; Sakamoto, K.; Hirano, Y.; Yamane, M. XPS Analysis of a Heat-Treated NiTi Surface for Elucidating Ni Segregation Phenomena. *Surf. Interface Anal.* **2016**, *48* (7), 488–492.
 - (10) Shabalovskaya, S.; Anderegg, J.; Van Humbeeck, J. Critical Overview of Nitinol Surfaces and Their Modifications for Medical Applications. *Acta Biomater.* **2008**, *4* (3), 447–467.
 - (11) Bellini, H.; Moyano, J.; Gil, J.; Puigdollers, A. Comparison of the Superelasticity of Different Nickel–titanium Orthodontic Archwires and the Loss of Their Properties by Heat Treatment. *J. Mater. Sci. Mater. Med.* **2016**, *27* (10).
 - (12) Biesinger, M. C.; Lau, L. W. M.; Gerson, A. R.; Smart, R. S. C. Resolving Surface Chemical States in XPS Analysis of First Row Transition Metals, Oxides and Hydroxides: Sc, Ti, V, Cu and Zn. *Appl. Surf. Sci.* **2010**, *257* (3), 887–898.
 - (13) Biesinger, M. C.; Payne, B. P.; Grosvenor, A. P.; Lau, L. W. M.; Gerson, A. R.; Smart, R. S. C. Resolving Surface Chemical States in XPS Analysis of First Row Transition Metals, Oxides and Hydroxides: Cr, Mn, Fe, Co and Ni. *Appl. Surf. Sci.* **2011**, *257* (7), 2717–2730.
 - (14) Schmid, M. A Simple Sputter Yield Calculator <https://www.iap.tuwien.ac.at/www/surface/sputteryield> (accessed Sep 1, 2018).
 - (15) N. Matsunami, Y. Yamamura, Y. Itikawa, N. Itoh, Y. Kazumata, S. Miyagawa, K. Morita, R. Shimizu, H. T. Energy Dependence of the Yields of Ion-Induced Sputtering of Monatomic Solids. *Rep. IPPJ-AM-32*. 1983, p 301.
 - (16) Viefhaus, H.; Hennesen, K.; Lucas, M.; Müller-Lorenz, E. M.; Grabke, H. J. Ion Sputter Rates and Yields for Iron-, Chromium- and Aluminium Oxide Layers. *Surf. Interface Anal.* **1994**, *21* (9), 665–672.
 - (17) Wei, C.; Bard, A. J.; Mirkin, M. V. Scanning Electrochemical Microscopy. 31. Application of SECM to the Study of Charge Transfer Processes at the Liquid/Liquid Interface. *J. Phys. Chem.* **1995**, *99* (43), 16033–16042.
 - (18) Cannes, C.; Kanoufi, F.; Bard, A. J. Cyclic Voltammetry and Scanning Electrochemical Microscopy of Ferrocenemethanol at Monolayer and Bilayer-Modified Gold Electrodes. *J. Electroanal. Chem.* **2003**, *547* (1), 83–91.

Chapter 4

Electroassisted functionalization of Nitinol surface, a powerful strategy for polymer coating through controlled radical surface initiation



4.1	Introduction	67
4.2	Experimental section	68
4.2.1.	Thermally assisted grafting of BUPA monolayers on NiTi	68
4.2.2.	Electroassisted grafting of BUPA monolayers on NiTi	69
4.2.3.	SI-ATRP of DMAEMA	69
4.3	Elaboration of SI-ATRP initiating monolayer	69
4.3.1.	Thermally assisted grafting of BUPA monolayers on NiTi	69
4.3.2.	Electroassisted grafting of BUPA monolayers on NiTi	72
4.4	SI-ATRP of DMAEMA on BUPA-covered NiTi	74
4.5	Conclusions	77
	References	77

4.1 Introduction

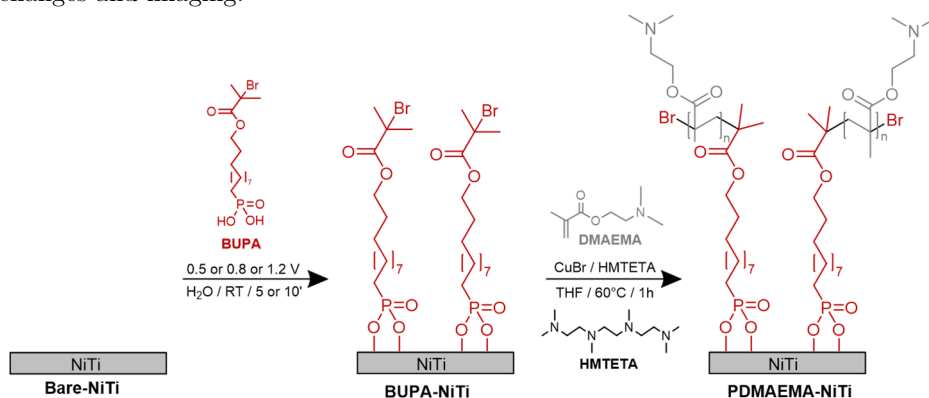
The elaboration of SAMs is a very convenient approach to introduce initiating functionalities with the purpose of promoting polymerization from the metal surfaces. Such formed layer constitutes an additional protection of the metal against its environment.¹⁻⁵ Moreover it enables the functionalization of its surface that can be harnessed for post-polymerization purposes, as the introduction of a functional polymer layer by a “grafting from” approach. To be successful, this particular point implies therefore the introduction of selective functional moieties that allow the initiation of a chain growth process from the surface. However, initiating sites such as alkyl-halogen groups (Atom Transfer Radical Polymerization (ATRP) initiating group),⁶ often supported by an ester group, are quite sensitive to degradation when long reaction times and/or harsh conditions are required. Therefore, mild conditions during SAMs preparation must be applied to prevent the initiating group degradation.

In this respect and considering the long modification times usually required to obtain densely formed monolayers, strategies to activate the SAMs preparation were developed in order to shorten preparation time and maintain the quality of the SAM. First, thermal activation using both conventional and magnetic induction heating were investigated by our team.⁷⁻⁹ The magnetic induction heating (MIH) in particular has emerged as a powerful activator process in surface chemistry, as recently reported in current literature.^{7,10,11} MIH is a technique based on physical phenomena (Faraday-Lenz law, Eddy currents, and Joule effect) commonly used to heat electrically conductive materials thanks to a time-varying magnetic field. A significant advantage of this technique relies on the possibility of heating locally a material without any contact. In particular, the energy can be focused on the surface of the material, hence limiting the energy input.^{10,12,13}

Alternatively, Metoki *et al.*¹⁴ as well as Vanhooland *et al.*¹⁵ from our group have recently investigated the electrochemical (EC) formation of alkylphosphonic acid-based SAMs in aqueous media on Ti-6Al-4V and on NiTi alloy surfaces, respectively. This method leads to the formation of high-quality SAMs of alkyl phosphonic acids within shorter modification time thanks to the positive polarization of the material and a preferential orientation of the molecules towards this electrode.

Short reaction times and mild reaction conditions make both MIH and EC processes very attractive to prepare functional SAMs retaining initiating sites starting from functional phosphonic acid derivatives. For this purpose, EC process is investigated in comparison to MIH and conventional heating to form sensitive SAMs carrying alkyl-halogen initiating groups (11-(2-bromoisobutyrate)-undecyl-1-phosphonic acid, BUPA). As a proof of concept, the unaffected initiating functions

are used to kick off the surface initiation of a model monomer, *i.e.* 2-(dimethylamino)ethyl methacrylate (DMAEMA), by Surface Initiated ATRP (coined as SI-ATRP)(Scheme 4.1). The benefits of this simple method are highlighted over NiTi corrosion inhibition, surface functionalization and physico-chemical property changes and imaging.



Scheme 4.1. Nitinol surface methodology used in this chapter: self-assembly of BUPA monolayers (left) and subsequent SI-ATRP of DMAEMA (right).

4.2 Experimental section

4.2.1. Thermally assisted grafting of BUPA monolayers on NiTi

The Nitinol substrates are modified by immersion in 10.0 mL of 1 mM solution of 11-(2-bromoisobutyrate)-undecyl-1-phosphonic acid (BUPA) in ultra-pure milli-Q water either at room temperature (RT), or heating using both magnetic induction (MIH) or conventional (CH) heating at 90°C according to the temperature profiles presented on Figure 4.1. The substrates are then ultrasonically cleaned in denatured ethanol for 15 min, before being blown dried under nitrogen and stored for characterizations.

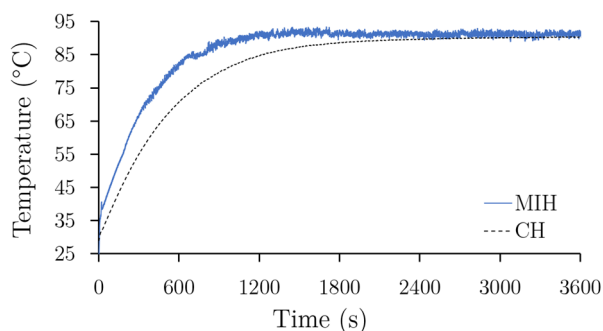


Figure 4.1. Temperature profiles of a Nitinol substrate heated in 10 mL ultra-pure milli-Q water by magnetic induction (MIH) or conventional (CH) heating at 90°C.

4.2.2. Electroassisted grafting of BUPA monolayers on NiTi

A solution (20.0 mL) composed of 1 mM 11-(2-bromoisobutyrate)-undecyl-1-phosphonic acid (BUPA) and 10 mM KNO_3 is prepared in ultra-pure milli-Q water.

The SAM is obtained by immersion of the substrate in the BUPA solution for 5 or 10 min, under a voltage of 0.5, 0.8 or 1.2 V *vs* a saturated calomel electrode (SCE). At the end, the substrates are ultrasonically cleaned in denatured ethanol for 15 min, before being blown dried under nitrogen and stored for characterizations.

4.2.3. SI-ATRP of DMAEMA

In a two-neck round-bottom flask are added $3.0 \cdot 10^{-4}$ mol of copper bromine (CuBr) and $6.0 \cdot 10^{-4}$ mol of 1,1,4,7,10,10-hexamethyltriethylenetetramine (HMTETA). The lateral neck is closed by a septum into which a clip is inserted to hold two substrates. The flask is then purged by three repeated vacuum/nitrogen cycles. In a second round-bottom flask are introduced 5.1 mL of 2-(dimethylamino)ethyl methacrylate (DMAEMA) and 14.8 mL of THF to reach a concentration of 1.5 M. The solution is then deprived from oxygen by nitrogen bubbling for few minutes.

The content of the second flask is transferred into the first one by the mean of a flamed dry capillary under N_2 atmosphere. The polymerization is then carried for 1 h at 60°C in an oil bath. At the end of the reaction, the flask is cooled down to room temperature. The substrates are then rinsed with THF and sonicated in THF for 15 min, rinsed with EtOH and sonicated in EtOH for 15 minutes. They are finally dried and stored under N_2 atmosphere.

4.3 Elaboration of SI-ATRP initiating monolayer

The preparation of functional and well-ordered SAMs through mild and time-saving processes is highly desirable to initiate a polymer coating via a “grafting from” approach, and hence to reinforce metal corrosion resistance. For this purpose, magnetically-induced heating (MIH) and electrochemically (EC) assisted processes are explored and compared to the conventional heating process to prepare homogeneous ATRP initiator-based SAMs, with increased resistance against corrosion and enabling the SI-ATRP of methacrylic monomers from the undamaged initiating species on the surface.

4.3.1. Thermally assisted grafting of BUPA monolayers on NiTi

The commercially available 11-(2-bromoisobutyrate)-undecyl-1-phosphonic acid (BUPA) is chosen to prepare a functional SAMs carrying ATRP initiating groups.

In a first series of experiments, the formation of BUPA monolayers is conducted by immersion of NiTi in a BUPA aqueous solution at either room temperature or at 90°C under conventional heating. Figure 4.2 presents the contact angle of water measured before and after surface modification in both conditions.

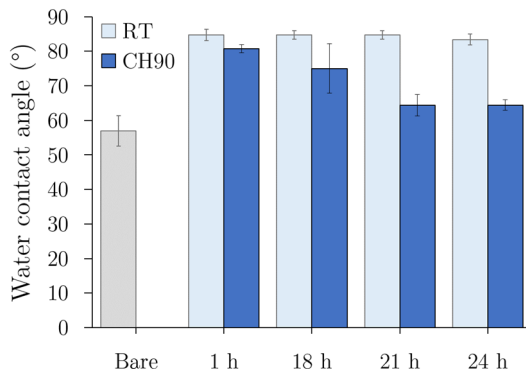


Figure 4.2. Water contact angles for bare NiTi and NiTi modified by immersion in a solution of 1 mM BUPA in ultra-pure milliQ water at room temperature (light blue) or under conventional heating at 90°C (dark blue).

As expected for a successful surface derivatization, the water contact angles of the material increase up to less hydrophilic values after only one hour of immersion. However, one can also observe a decrease of water contact value versus time when conventional heating is applied. This behaviour is explained via the thermal degradation of BUPA, and especially the hydrolysis of the bromoisobutyrate group, which leads to hydroxide functions on the surface. This hypothesis is confirmed by PM-IRRAS as no absorbance bands typical of the C=O and C-O bonds usually seen at 1734 and 1178 cm^{-1} are detected (Supporting information - Figure A.1). Hence, long modification times must be avoided under thermal conditions, and only modifications times of 1 h will be further considered in the sequel.

X-ray photoelectron spectroscopy (XPS) analyses performed on both bare and modified NiTi reveal the successful surface modification of the NiTi through the general shape of the obtained spectra for C1s core level as presented in Figure 4.3. Both bare (Figure 4.3a) and modified (Figure 4.3b) NiTi exhibit peaks at similar energies, but with higher intensities for the SAM modified NiTi, attesting therefore to a successful organic modification of the surface alloy. Those bands, at energies of 285 eV, 286.5 eV and 289.1 eV, correspond respectively to carbon atoms involved in C-H/C-C, C-O and O-C=O bonds present in BUPA (1-3) or in atmospheric contaminations (a-c). The peak at 283.3 eV is assigned to an artefact from the spectrometer.

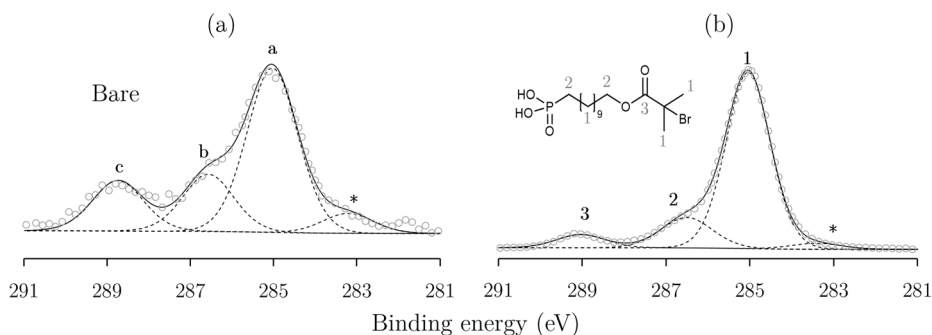


Figure 4.3. XPS general shape of core spectra for C1s component obtained for bare NiTi (bottom) and NiTi modified by immersion in a solution of 1 mM BUPA in ultra-pure milliQ water at room temperature or under conventional heating at 90°C (top).

The C/NiTi and P/NiTi ratios are used to evaluate the amount of organic molecules grafted on NiTi. The evolution of these ratios as a function of the tested conditions (Figure 4.4) shows an increase of the C/NiTi and P/NiTi ratios for all applied conditions, attesting the formation of BUPA layer. The ratios presented in Figure 4.4 indicates that the 1h thermal activation process used for the grafting lead to a layer as dense as the one obtained after 24h at RT . The same experiment was conducted under MIH for 1h, whereas this activation seems less effective as the C/NiTi and P/NiTi ratios decrease, even if exhibiting a similar water contact angle value of 81.3 ± 0.4 .

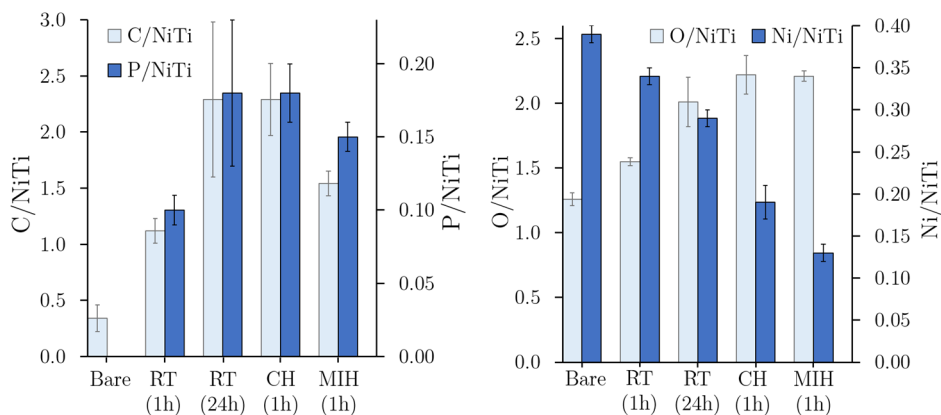


Figure 4.4. XPS atomic ratios for bare NiTi and NiTi modified after immersion in a solution of 1 mM BUPA in ultra-pure milliQ water at room temperature or under conventional heating at 90°C.

The impact of the grafting process on the NiTi substrate itself has also been investigated by measuring the O/NiTi and Ni/NiTi ratios. Two important effects

can be considered: a slight reinforcement of the oxide layer, represented by an increase of O/NiTi ratio, and a strong decrease of the detected amount of nickel. These observations are in agreement with the studies conducted by Devillers *et al.*^{10,15} where authors concluded that the hydrothermal treatment of NiTi leads to an enrichment of the titanium oxide layer at the surface while nickel is released in the environment once immersed in boiling water.

Despite these positive results concerning the grafting of BUPA, no bromine atom is detected by XPS (Supporting information - Figure A.2), meaning that the BUPA monolayers are degraded by hydrolysis, even for shorter reaction times, and are thus inappropriate for the post-functionalization by SI-ATRP.

4.3.2. Electroassisted grafting of BUPA monolayers on NiTi

Electro-assisted grafting is a promising alternative to thermally assisted processes as it allows the use of much shorter reaction time, in the absence of thermal assistance, which is expected to maintain the chemical integrity of the BUPA molecule. Its grafting has been assessed for different potentials and times.

The water contact angle values ranging from 75° to 80° after NiTi modification with BUPA (Figure 4.5) point to a significant decrease of the hydrophilicity. These values are typical of BUPA-modified NiTi by immersion at room temperature. The applied potential has less effect as the water contact angles remain invariable.

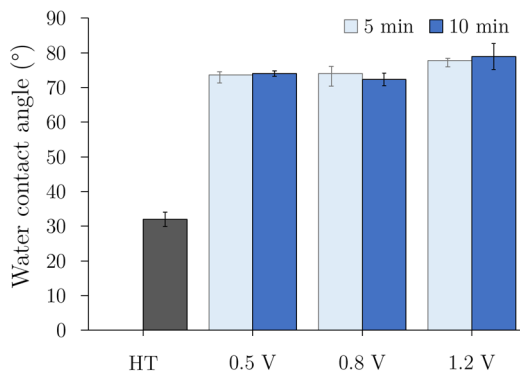


Figure 4.5. Water contact angles for hydrothermally treated NiTi and hydrothermally treated NiTi modified by immersion in a solution of 1 mM BUPA in ultra-pure milliQ water in presence of 10 mM KNO_3 under a potential of 0.5, 0.8 or 1.2 V vs SCE during 5 or 10 min.

Figure 4.6 displays PM-IRRAS spectra for hydrothermally treated NiTi, which is completely flat, and for BUPA modified NiTi for different times and potentials. Whatever the time and potential conditions, bands characteristic of BUPA molecule are visible, more precisely the band at 1734 cm^{-1} , typical of the stretching of

C=O bonds and the two bands centred at 1238 and 1178 cm^{-1} are respectively assigned to the asymmetric and the symmetric stretching of the C-O bond of the bromoisobutyrate function.

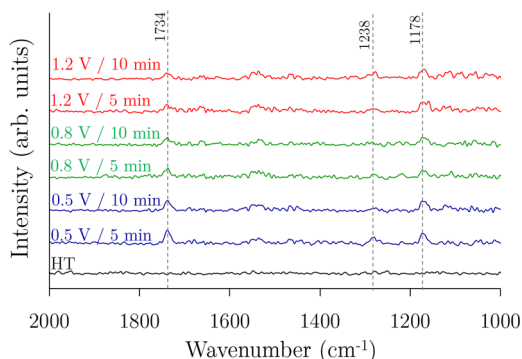


Figure 4.6. PM-IRRAS spectra of hydrothermally treated NiTi and NiTi modified by immersion in a solution of 1 mM BUPA in ultra-pure milli-Q in presence of 10 mM KNO_3 under a potential of 0.5, 0.8 or 1.2 V vs SCE during 5 or 10 min

The XPS results, especially the high C/NiTi and Br/P ratios (Figure 4.7), confirm the efficiency of BUPA electrochemically assisted grafting as C/NiTi ratio increases in comparison to the hydrothermally treated substrate. More importantly Br3s electrons can also be detected at the various applied potentials and for 5 and 10 minutes of reaction times (Figure 4.8). These observations attest the retention of the alkyl-bromine function when electrochemically assisted grafting is used. This result proves that BUPA is less degraded by electro- than by thermally assisted grafting.

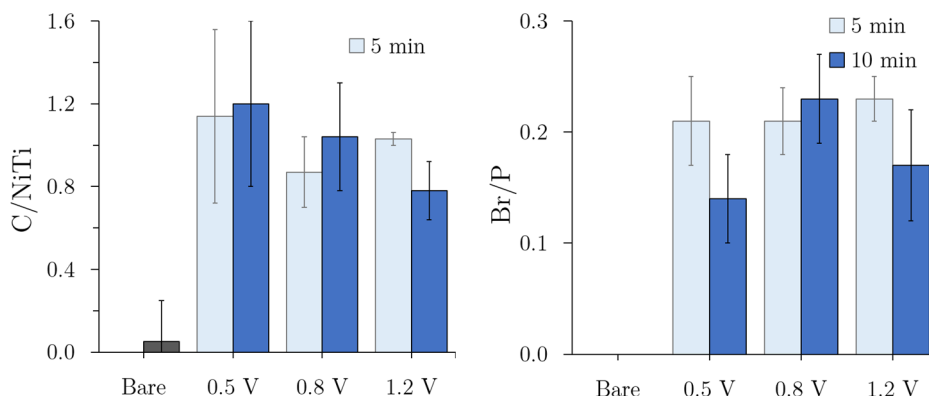


Figure 4.7. XPS atomic ratios for bare NiTi, hydrothermally treated NiTi and NiTi modified by immersion in a solution of 1 mM BUPA and 10 mM KNO_3 in ultra-pure milliQ water under a potential of 0.5, 0.8, or 1.2 V vs SCE.

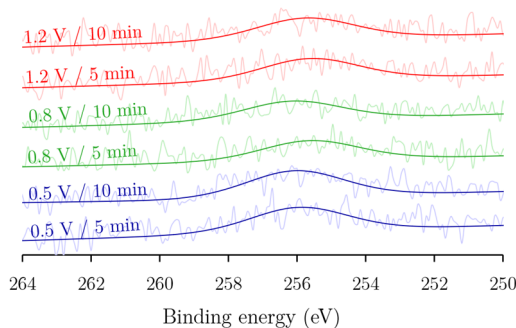


Figure 4.8. Br3s core level for NiTi modified by immersion in a solution of 1 mM BUPA and 10 mM KNO₃ in ultra-pure milliQ water under a potential of 0.5, 0.8, or 1.2 V vs SCE.

The results obtained by linear sweep voltammetry (LSV) (Table 4.1) do not indicate an improvement of the corrosion resistance of BUPA covered NiTi substrates, as j_{corr} barely decreases and E_{corr} barely increases. This is in accordance with the molecular structure of BUPA, which prevents the formation of a compact monolayer due to the size of its hydrophilic bromoisobutyrate group.

Table 4.1. Values of E_{corr} and j_{corr} for bare NiTi, hydrothermally treated NiTi and NiTi substrates modified by electrografting of BUPA 1 mM in ultrapure water at 0.5, 0.8, or 1.2 V vs SCE during 5 or 10 min in presence of 10 mM KNO₃ (obtained by LSV).

Sample	E_{corr} (mV vs SCE)	j_{corr} (A cm ⁻²)
Bare	-293 ± 66	9.05 10 ⁻⁷ ± 5.31 10 ⁻⁷
HT	-268 ± 18	7.29 10 ⁻⁸ ± 4.98 10 ⁻⁸
0.5 V / 5'	-278 ± 34	9.80 10 ⁻⁸ ± 1.63 10 ⁻⁸
0.5 V / 10'	-319 ± 39	9.07 10 ⁻⁸ ± 2.18 10 ⁻⁸
0.8 V / 5'	-268 ± 29	1.80 10 ⁻⁷ ± 2.61 10 ⁻⁸
0.8 V / 10'	-227 ± 43	2.21 10 ⁻⁷ ± 5.22 10 ⁻⁸
1.2 V / 5'	-255 ± 26	1.65 10 ⁻⁷ ± 5.46 10 ⁻⁸
1.2 V / 10'	-186 ± 182	9.98 10 ⁻⁸ ± 7.81 10 ⁻⁸

From these results, the optimum grafting conditions (high C/NiTi, Br/NiTi and reproducibility) appears to be the EC process at a potential of 1.2V during 5 min.

4.4 SI-ATRP of DMAEMA on BUPA-covered NiTi

The so-formed BUPA-covered Nitinol substrates are used for SI-ATRP of 2-(dimethylamino)ethyl methacrylate (DMAEMA, *cf.* 4.2.3) to validate the benefits of the EC process as it ensures the quality and the usability of the initiation layer.

The polymerization was conducted at a concentration of 1.5 M for 1 h in the presence of CuBr.2HMTETA complex, in THF.

After polymerization, the measured WCA of the modified surface drops from a value of 78.2 ± 1.1 down to 61.2 ± 12.3 . This increase in hydrophilicity is consistent with the presence of the hydrophilic PDMAEMA layer grafted on the surface. The nature of the formed coating is confirmed jointly by PM-IRRAS (Figure 4.9) and XPS (Figure 4.10).

The PM-IRRAS spectrum obtained for the modified substrate presents several distinct absorption bands. The first ones, at 1154 and 1239 cm^{-1} , correspond to the asymmetrical stretching of C-N bonds. The two bands centred at 1178 and 1273 cm^{-1} are respectively assigned to the symmetrical and asymmetrical stretching of C-O bonds, whereas those centred at 1461 and 1486 cm^{-1} correspond to the asymmetrical deformation of CH_3 groups and to the scissoring of C-H bonds. The band at 1734 cm^{-1} is attributed to the stretching of C=O bonds and the last ones centred at 2721 and 2821 cm^{-1} correspond to the stretching of N-C-H bonds.¹⁶ All those bands are characteristics of PDMAEMA.

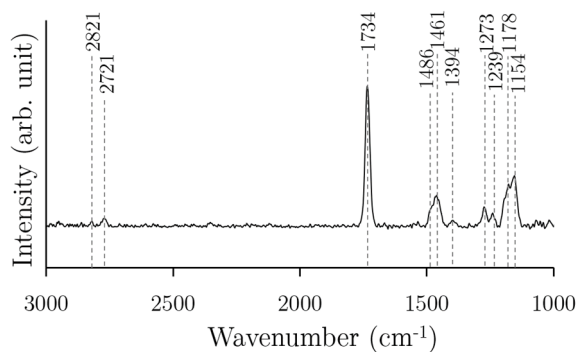


Figure 4.9. PM-IRRAS spectrum of BUPA-covered NiTi modified by SI-ATRP of 1.5 M DMAEMA in solution in THF in presence of 13.9 mM CuBr and 1.39 mM HMTETA for 1 hour at 60°C

The XPS spectra (Figure 4.10) obtained for C1s (and its subsequent analyses) and N1s unambiguously confirm the nature of PDMAEMA. Br atoms are also detected from the surface analysis, which is consistent with the controlled nature of the SI-ATRP process. Finally, no copper has been detected at the surface, meaning that no catalyst is trapped in the polymer layer. Knowing the high propensity of tertiary amines to form complexes with copper through Lewis acid-base interactions, this observation renders our approach particularly attractive for biomedical applications.

As an additional control, the same polymerizations were conducted from a hydrothermally treated NiTi, while in this case, the metal surface is free of initiating groups. In these conditions, no absorption band can be detected on the PM-IRRAS spectra (Supporting information - Figure A.3), whereas only peaks of low intensities can be seen on XPS spectrum (Supporting information - Figure A.4), those corresponding to BUPA.

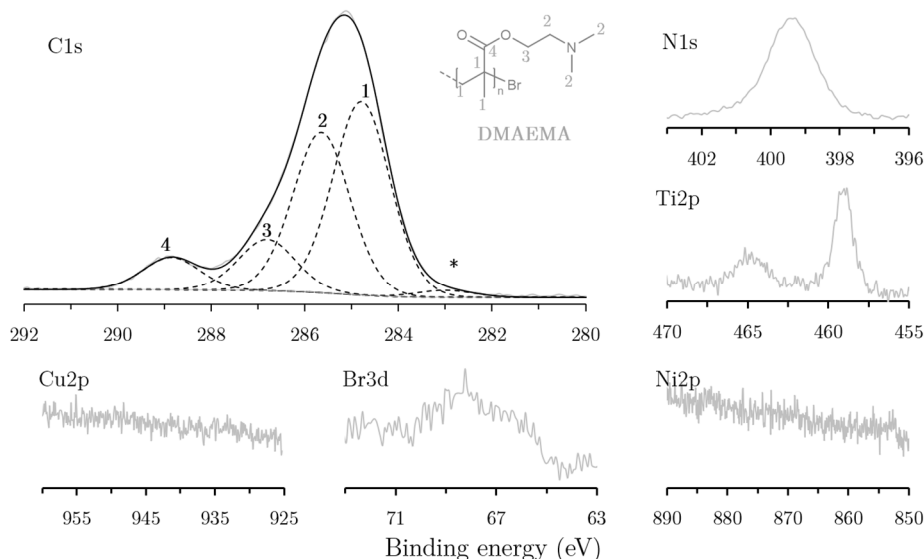


Figure 4.10. XPS core spectra for C1s, N1s, Ti2p, Ni2p, Cu2p and Br3d components obtained for BUPA-covered NiTi modified by SI-ATRP of 1.5 M DMAEMA in solution in THF in presence of 13.9 mM CuBr and 1.39 mM HMTETA for 1 hour at 60°C

The obtained results attest that PDMAEMA layer arises from a “grafting from” approach and mediated in a control way by ATRP. Indirectly, these results demonstrate for the first time the ability of electrochemically assisted approach to form stable functional BUPA-based SAMs retaining sensitive initiating sites.

The protective behaviour of the formed polymer layers has been assessed by LSV (Table 4.2). The results indicate a slight improvement of the corrosion resistance of the substrates, as j_{corr} decreases and E_{corr} increases.

Table 4.2. Values of E_{corr} and j_{corr} for HT-NiTi and BUPA covered NiTi modified by SI-ATRP of 1.5 M DMAEMA in solution in THF in presence of 13.9 mM CuBr and 1.39 mM HMTETA for 1 hour at 60°C.

Sample	E_{corr} (mV vs SCE)	j_{corr} (A cm ⁻²)
HT	-268 ± 18	7.29 10 ⁻⁸ ± 4.98 10 ⁻⁸
BUPA	-255 ± 26	1.65 10 ⁻⁷ ± 5.46 10 ⁻⁸
PDMAEMA	-203 ± 34	8.30 10 ⁻⁸ ± 1.97 10 ⁻⁸

As a confirmation, the same polymerization process has been performed on thermally assisted grafted NiTi substrates. As expected, no PDMAEMA coating is detected by PM-IRRAS and XPS (Figure A.5), thus confirming the degradation of BUPA under thermal treatment.

4.5 Conclusions

In this chapter, thermally- and electro-assisted self-assembling of 11-(2-bromoisobutyrate)-undecyl-1-phosphonic acid (BUPA) on Nitinol have been compared.

Among all the tested conditions, the best grafting of BUPA is achieved by 5 minutes of electrochemically (EC) assisted self-assembly at RT. PM-IRRAS and XPS results obtained for EC point to a successful surface modification of NiTi by BUPA (amounts of grafted molecules and of remaining Br atoms at the surface. Thus, the electrografting appears to be a good alternative for fast self-assembly of sensitive molecules such as BUPA.

Finally, the so-formed BUPA monolayer have been successfully used as an initiation layer for the surface-initiated atom transfer polymerization of 2-(dimethyl-amino)ethyl methacrylate, a model methacrylic monomer, as proven by PM-IRRAS and XPS results.

Nonetheless, the thermally assisted processes used in this work (CH and MIH) remain a very attractive tool to promote the self-assembly of robust phosphonic acid derivatives, such as aliphatic phosphonic acid derivatives and deserve deeper investigation and interest.

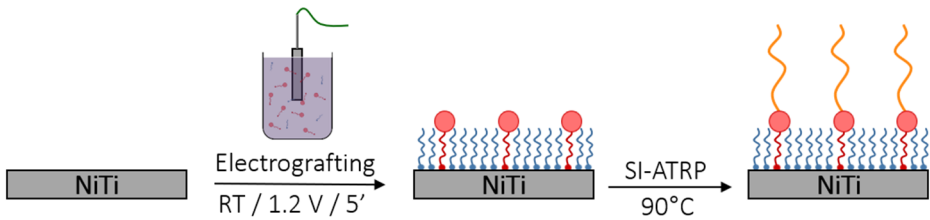
References

- (1) Quiñones, R.; Raman, A.; Gawalt, E. S. Functionalization of Nickel Oxide Using Alkylphosphonic Acid Self-Assembled Monolayers. *Thin Solid Films* **2008**, *516* (23), 8774–8781.
- (2) Ishizaki, T.; Okido, M.; Masuda, Y.; Saito, N.; Sakamoto, M. Corrosion Resistant Performances of Alkanoic and Phosphonic Acids Derived Self-Assembled Monolayers on Magnesium Alloy AZ31 by Vapor-Phase Method. *Langmuir* **2011**, *27* (10), 6009–6017.
- (3) Devillers, S.; Lemineur, J. F.; Dilimon, V. S.; Barthélémy, B.; Delhalle, J.; Mekhalif, Z. Polyelectrolyte Multilayer Deposition on Nickel Modified with Self-Assembled Monolayers of Organophosphonic Acids for Biomaterials: Electrochemical and Spectroscopic Evaluation. *J. Phys. Chem. C* **2012**, *116* (36), 19252–19261.
- (4) Guerrero, G.; Alauzun, J. G.; Granier, M.; Laurencin, D.; Mutin, P. H. Phosphonate Coupling Molecules for the Control of Surface/interface Properties and the Synthesis of Nanomaterials. *Dalt. Trans.* **2013**, *42* (35), 12569.
- (5) Abohalkuma, T.; Telegdi, J. Corrosion Protection of Carbon Steel by Special

- Phosphonic Acid Nano-Layers. *Mater. Corros.* **2015**, No. 12, 1382–1390.
- (6) Matyjaszewski, K.; Tsarevsky, N. V. Macromolecular Engineering by Atom Transfer Radical Polymerization. *J. Am. Chem. Soc.* **2014**, *136* (18), 6513–6533.
- (7) Devillers, S.; Lanners, L.; Delhalle, J.; Mekhalif, Z. Grafting of Bifunctional Phosphonic and Carboxylic Acids on Phynox: Impact of Induction Heating. *Appl. Surf. Sci.* **2011**, *257* (14), 6152–6162.
- (8) Barthelemy, B.; Devillers, S.; Fonder, G.; Delhalle, J.; Mekhalif, Z. Chitosan and Alginate Layer-by-Layer Assembly on Phynox (Co-Cr Alloy) Surface Modified by Alkylcarboxylic ammonium phosphonate Derivatives. *J. Electrochem. Soc.* **2013**, *160* (11), H820–H828.
- (9) Jacques, A.; Barthélémy, B.; Delhalle, J.; Mekhalif, Z. 1-Pyrrolyl-10-Decylammonium phosphonate Monolayer: A Molecular Nanolink between Electropolymerized Pyrrole Films and Nickel or Titanium Surfaces. *Electrochim. Acta* **2015**, *170*, 218–228.
- (10) Devillers, S.; Barthélémy, B.; Delhalle, J.; Mekhalif, Z. Induction Heating Vs Conventional Heating for the Hydrothermal Treatment of Nitinol and Its Subsequent 2-(Methacryloyloxy)ethyl 2-(Trimethylammonio)ethyl Phosphate Coating by Surface-Initiated Atom Transfer Radical Polymerization. *ACS Appl. Mater. Interfaces* **2011**, *3* (10), 4059–4066.
- (11) Devillers, S.; Lemineur, Q.; Delhalle, J.; Mekhalif, Z. Induction vs . Conventional Heating : Impact on the Morphology and Crystallinity of Copper Electrodeposits on Nickel. *J. Electrochem. Soc.* **2011**, *158* (11), E111–E118.
- (12) Rudnev, V.; Loveless, D.; Cook, R.; Black, M. *Handbook of Induction Heating*, Marcel Dek.; Marinescu, I., Geoffrey, B., Eds.; CRC Press: New York, 2002.
- (13) Jacques, A.; Chehimi, M. M.; Poleunis, C.; Delcorte, A.; Delhalle, J.; Mekhalif, Z. Grafting of 4-Pyrrolylphenyldiazonium in Situ Generated on NiTi, an Adhesion Promoter for Pyrrole Electropolymerisation? *Electrochim. Acta* **2016**, *211*, 879–890.
- (14) Metoki, N.; Liu, L.; Beilis, E.; Eliaz, N.; Mandler, D. Preparation and Characterization of Alkylphosphonic Acid Self-Assembled Monolayers on Titanium Alloy by Chemisorption and Electrochemical Deposition. *Langmuir* **2014**, *30* (23), 6791–6799.
- (15) Vanhooland, A.; Devillers, S.; Issakova, T.; Michaux, C.; Delhalle, J.; Mekhalif, Z. Electroassisted Auto-Assembly of Alkylphosphonic Acids Monolayers on Nitinol. *J. Electrochem. Soc.* **2016**, *163* (10), G173–G177.
- (16) Socrates, G. *Infrared and Raman Characteristic Group Frequencies: Tables and Charts*, Third Edit.; John Wiley & Sons, 2004.

Chapter 5

Electrografting of organophosphonic mixed monolayer for SI-ATRP of 2-methacryloyloxyethyl phosphorylcholine



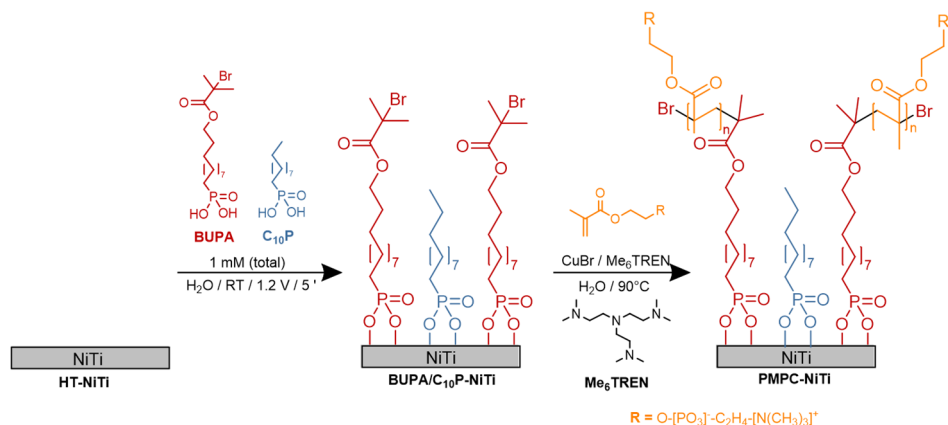
5.1	Introduction	81
5.2	Experimental section	82
5.2.1.	Electroassisted grafting of mixed initiating monolayers on NiTi.....	82
5.2.2.	SI-ATRP of MPC	82
5.3	Elaboration of BUPA/C₁₀P mixed monolayers	83
5.4	SI-ATRP of MPC on BUPA/C₁₀P-covered NiTi.....	88
5.5	Conclusions	92
	References	93

5.1 Introduction

In the previous chapter, the electro-assisted approach has been proven to lead to the formation of high quality SAMs within short modification times and at room temperature. Thus, it is an alternative way to graft SI-ATRP initiators based on phosphonic acid derivatives while preserving the sensitive chemical functions, such as C-Br in the 11-(2-bromoisobutyrate)-undecyl-1-phosphonic acid (BUPA) used as ATRP initiator.¹ However, BUPA initiating functions are quite bulky and may lead to disordered and less protective layers. The use of mixed monolayers resulting from the co-adsorption of two organophosphonic acid derivatives differing in length and/or terminal functional groups has been reported to improve the corrosion resistance as well as the layer organization.²⁻⁵

Among the promising and versatile surface characterization techniques, scanning electrochemical microscopy (SECM), based on the use of an ultramicroelectrode facing a substrate, allows to probe locally its electrochemical property, *i.e.* its conducting/insulating behaviour, or to provide high resolution information on the electrochemical processes occurring at the surface.⁶⁻⁹ Over the last years, SECM has been widely applied for the study of self-assembled monolayers properties and impact over corrosion resistance,¹⁰⁻¹³ and on organic layer permeability.^{14,15} But so far, only few SECM studies have been performed on Nitinol,^{10,16,17} which thus remain of great interest.

The aim of the work presented in this chapter is to improve the quality of the electro-grafted SAMs on NiTi. To this end, mixed SAMs carrying alkyl-halogen initiating groups of 11-(2-bromoisobutyrate)-undecyl-1-phosphonic acid (BUPA) are formed on NiTi after its hydrothermal treatment by incorporating 1-decylphosphonic acid (C₁₀P) molecules with a shorter hydrophobic alkyl chain. Various amounts of BUPA/C₁₀P are studied to optimise the quality of the SAM organisation and consequently the NiTi corrosion resistance while keeping sufficient amount of grafted BUPA for the polymerisation. The so-formed mixed SAMs are used to initiate the surface polymerization of 2-methacryloyloxyethyl phosphorylcholine (MPC), a biocompatible monomer (Scheme 1). The originality of this work resides in the combination of the electro-assisted approach for the grafting of mixed monolayer which is in itself a relatively new promising method and particularly suitable for temperature sensitive groups. In this context, the SI-ATRP can be considered as an indirect evaluation way for the achievement of those surface modifications. The benefits of this method are highlighted over NiTi corrosion inhibition, surface functionalization and physico-chemical properties.



Scheme 5.1. Nitinol surface methodology used in this chapter: self-assembly of BUPA monolayers (left) and subsequent SI-ATRP of MPC (right).

5.2 Experimental section

5.2.1. Electroassisted grafting of mixed initiating monolayers on NiTi

Solutions (20.0 mL) composed of 1 mM of a mixture of 11-(2-bromoisobutyrate)-undecyl-1-phosphonic acid (BUPA)/1-decylphosphonic acid (C_{10}P) in various ratios and 10 mM KNO_3 are prepared in ultra-pure milli-Q water.

The SAMs on HT-NiTi surfaces are obtained by immersion of the substrate in the solution for 5 min, under a voltage of 1.2 V *vs* a saturated calomel electrode (SCE). At the end, the substrates are ultrasonically cleaned in denatured ethanol for 15 min, before being blown dried under nitrogen and stored for characterizations.

5.2.2. SI-ATRP of MPC

In a four-neck round-bottom flask are added $3.0 \cdot 10^{-4}$ mol of copper bromine (CuBr) and $6.0 \cdot 10^{-4}$ mol of tris[2-(dimethylamino)ethyl]amine (Me_6TREN). The three lateral necks are closed by septums into which a clip is inserted to hold two substrates. The flask is then purged by three repeated vacuum/nitrogen cycles. In a second round-bottom flask are introduced $3.4 \cdot 10^{-3}$ mol of 2-methacryloyloxyethyl phosphorylcholine and 19.8 mL of milli-Q water to reach a concentration of 0.17 M. The MPC solution is then deaerated by nitrogen bubbling for few minutes.

The content of the second flask is transferred into the first one by the mean of a flamed dry capillary under N_2 atmosphere. The polymerization is then carried out for 1, 3 or 6 h at 90°C in an oil bath. At the end of the reaction, the flask is cooled down to room temperature. The substrates are then rinsed with denatured EtOH and sonicated in denatured EtOH for 15 minutes. They are finally dried and stored under N_2 atmosphere.

5.3 Elaboration of BUPA/C₁₀P mixed monolayers

The electro-assisted approach, based on the optimised conditions determined in our previous work ($E=1.2$ V vs SCE and $t=5$ min),¹ is transposed to the grafting of C₁₀P (C₁₀P-NiTi), BUPA (BUPA-NiTi) and their mixture in different ratios (BUPA/C₁₀P-NiTi) on HT-NiTi. The resulting modified NiTi surfaces are characterized with contact angle measurements, PM-IRRAS, XPS and electrochemical analyses.

Figure 5.1 highlights the wettability properties of HT-NiTi, C₁₀P-NiTi, BUPA-NiTi and BUPA/C₁₀P-NiTi. The water contact angle values (θ_w) ranging from 78° to 92° after NiTi modification point to a significant increase of the contact angle compared to HT-NiTi ($\theta_w = 30^\circ$). The highest θ_w value, indicating the less hydrophylic surface, is obtained for C₁₀P-NiTi ($\theta_w = 92^\circ$). Increasing the ratio of BUPA/C₁₀P does not drastically change the θ_w values which remain very close ($\theta_w \sim 80^\circ$) to that of BUPA-NiTi. This is consistent with the fact that C₁₀P molecules are shorter than BUPA and have thus less impact on the wettability properties, even at high concentration in the mixed monolayer.

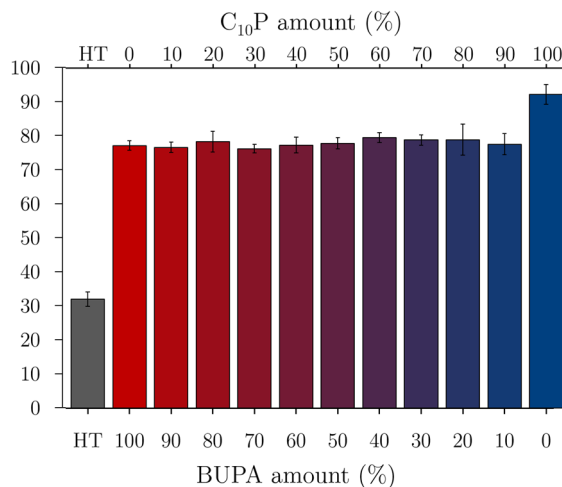


Figure 5.1. Water contact angles for HT-NiTi, BUPA-NiTi, C₁₀P-NiTi and BUPA/C₁₀P-NiTi (in various ratios).

Figure 5.2 displays PM-IRRAS spectra for HT-NiTi and BUPA/C₁₀P-NiTi. HT-NiTi does not show any signal of any chemical functions while BUPA/C₁₀P-NiTi show, whatever the molecular ratio, vibrational bands typical of BUPA at 1276/1261 and 1170 cm⁻¹, assigned respectively to the asymmetric and the symmetric stretching of the C-O bond of the bromoisobutyrate function, and to C-H deformation.¹⁸

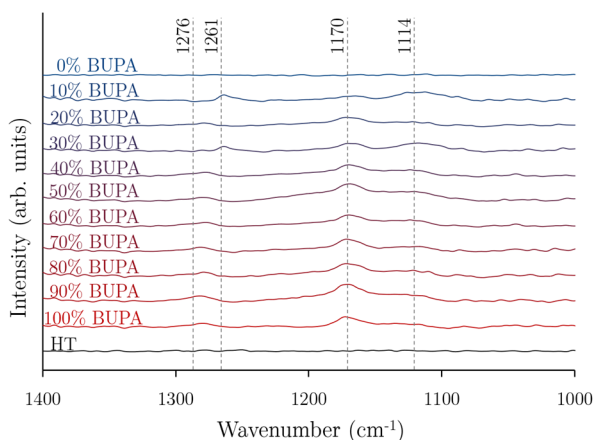


Figure 5.2. PM-IRRAS spectra for HT-NiTi, BUPA-NiTi, C₁₀P-NiTi and BUPA/C₁₀P-NiTi.

Results of the X-ray photoelectron spectroscopy (XPS) analyses performed on HT-NiTi and modified NiTi are reported in Figure 5.3 and Table 5.1. C1s core-level (Figure 5.3) displays peaks at similar energies but with higher intensities for modified NiTi indicating therefore an effective grafting of C₁₀P and BUPA on HT-NiTi. These peaks at energies of 285 eV, 286.5 eV and 289.1 eV, correspond respectively to carbon atoms involved in C-H/C-C, C-O/C-P and O-C=O bonds present in the phosphonic acid derivatives (peak 1 for C₁₀P) and (peaks 1-3 for BUPA) or in atmospheric contaminations (peaks a-c for HT-NiTi). The one at 283.3 eV (*) is assigned to an artefact from the spectrometer.

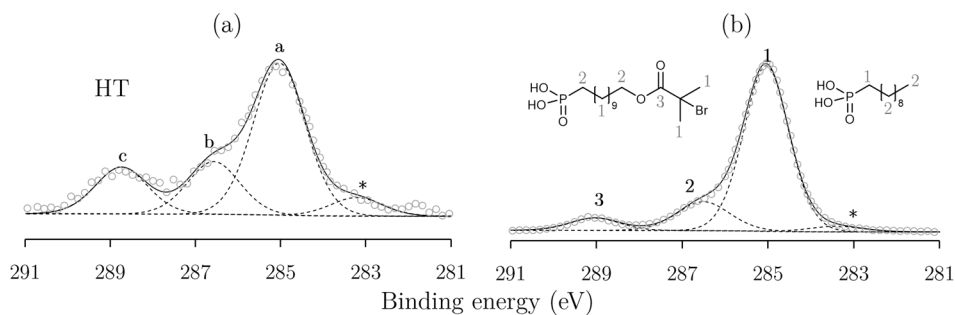


Figure 5.3. Representative XPS C1s core-levels for HT-NiTi, BUPA-NiTi, C₁₀P-NiTi and BUPA/C₁₀P-NiTi (in various ratios).

In addition to the increase of C1s intensity, XPS analyses reveal the presence of P2p for all BUPA-NiTi, C₁₀P-NiTi and BUPA/C₁₀P-NiTi and Br3s for BUPA-NiTi and BUPA/C₁₀P-NiTi. When adding C₁₀P to BUPA, the C/NiTi and P/NiTi ratios increase (Table 5.1) indicating the formation of denser and more organized layers due to the insertion of C₁₀P. The maximum is achieved for 60% of BUPA.

The C/NiTi ratio then decreases due to the shorter chain of C₁₀P replacing the longer BUPA ones while P/NiTi remains almost stable (0.13-0.17). The Br/P ratio is barely affected by the decrease of BUPA amount which prove that pure BUPA layer is not very well organised and partially degraded.

Table 5.1. XPS atomic ratios for HT-NiTi and BUPA/C₁₀P-NiTi (in various ratios) and estimated SAM thickness.

Sample	C/NiTi	P/NiTi	Br/P	d _{SAM} (nm)
HT	0.10 ± 0.20	-	-	-
100% BUPA	1.03 ± 0.32	0.09 ± 0.01	0.23 ± 0.05	1.93 ± 0.38
90% BUPA	1.34 ± 0.48	0.11 ± 0.01	0.23 ± 0.07	1.90 ± 0.15
80% BUPA	1.63 ± 0.27	0.11 ± 0.01	0.25 ± 0.05	1.83 ± 0.15
70% BUPA	2.29 ± 0.23	0.15 ± 0.01	0.21 ± 0.02	1.87 ± 0.15
60% BUPA	2.51 ± 0.25	0.17 ± 0.01	0.18 ± 0.01	1.71 ± 0.12
50% BUPA	1.93 ± 0.20	0.15 ± 0.01	0.18 ± 0.02	1.76 ± 0.16
40% BUPA	1.64 ± 0.10	0.13 ± 0.01	0.16 ± 0.02	1.58 ± 0.07
30% BUPA	1.68 ± 0.26	0.13 ± 0.01	0.19 ± 0.04	1.54 ± 0.22
20% BUPA	1.61 ± 0.12	0.15 ± 0.01	0.20 ± 0.07	0.95 ± 0.12
10% BUPA	1.66 ± 0.26	0.14 ± 0.01	0.21 ± 0.05	1.03 ± 0.37
0% BUPA	1.51 ± 0.11	0.15 ± 0.01	-	0.60 ± 0.13

The approximated thickness of BUPA layer (1.93 ± 0.38 nm) is consistent with the simulated value of 2.02 nm (Figure 5.4a), whereas the estimated thickness of C₁₀P layer is underestimated from a theoretical value of 1.41 nm to 0.60 ± 0.13 nm. This difference could result from a tilted denser organization of the C₁₀P layer. The coating thickness decreases with the incorporation of C₁₀P (Table 5.1), which also attests the formation of a tilted denser layer as shown on Figure 5.4b.

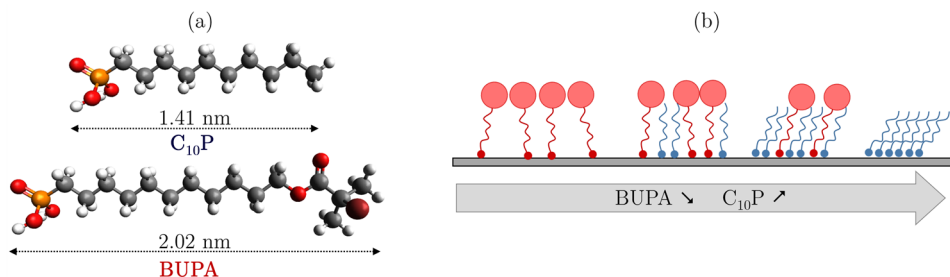


Figure 5.4. Model structures of C₁₀P and BUPA (a), and schematic representation of BUPA/C₁₀P coatings thickness based on XPS results (b).

Electrochemical evaluation of modified NiTi is compared to HT-NiTi on the basis of three methods (LSV, CV and SECM). LSV results (Figure 5.4 - Table 5.2

- Supporting information Figure A.6) indicate a strong improvement of the corrosion resistance of BUPA/C₁₀P-NiTi with the decrease of BUPA amount, *e.g.* corrosion current density (j_{corr}) decreases from 95.1 nA cm⁻² to 9.4 nA cm⁻² for 20 % of BUPA. This is once again in accordance with the formation of a denser and more organized layer due to higher amount of C₁₀P within the layer.

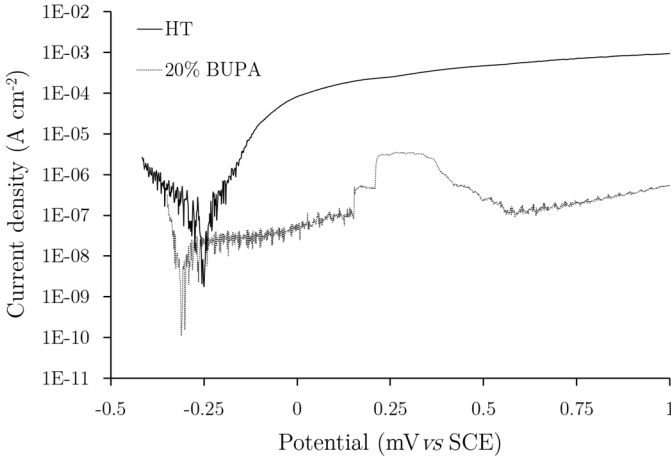


Figure 5.5. Representative polarization curves for HT-NiTi and BUPA/C₁₀P (20/80) in 0.5 M NaCl at a scan rate of 1 mV s⁻¹.

Table 5.2. Values of E_{corr} , j_{corr} , IE, BF and k_{ct} for HT-NiTi and BUPA/C₁₀P-NiTi (in various ratios) (obtained by LSV, CV and SECM).

Sample	E_{cor} (mV vs SCE)	j_{corr} (nA cm ⁻²)	IE (%)	BF (%)	k_{ct} ($\mu\text{m s}^{-1}$)
NiTi-HT	-266 ± 22	103.6 ± 22.2	-	-	10.8 ± 1.1
100% BUPA	-262 ± 34	95.1 ± 28.8	89.1 ± 3.3	72.3 ± 5.0	1.8 ± 1.6
90% BUPA	-233 ± 70	29.2 ± 21.1	96.6 ± 2.4	96.3 ± 1.9	1.2 ± 0.1
80% BUPA	-193 ± 45	31.2 ± 17.1	96.4 ± 2.0	84.4 ± 6.4	0.5 ± 0.3
70% BUPA	-217 ± 24	35.7 ± 27.2	95.9 ± 3.1	88.0 ± 16.7	2.1 ± 0.6
60% BUPA	-289 ± 19	72.3 ± 3.8	91.7 ± 0.4	76.8 ± 23.1	0.4 ± 0.2
50% BUPA	-194 ± 86	11.1 ± 10.4	98.7 ± 1.2	98.2 ± 0.3	1.8 ± 0.2
40% BUPA	-296 ± 13	109.4 ± 41.2	87.4 ± 4.7	86.0 ± 8.1	0.9 ± 0.2
30% BUPA	-160 ± 96	32.9 ± 22.2	96.2 ± 2.6	88.2 ± 10.5	1.0 ± 0.2
20% BUPA	-314 ± 41	9.4 ± 6.4	98.9 ± 0.7	93.9 ± 6.6	0.6 ± 0.1
10% BUPA	-252 ± 56	82.7 ± 55.6	90.5 ± 6.4	93.7 ± 2.1	0.7 ± 0.1
0% BUPA	-256 ± 29	59.0 ± 38.9	93.5 ± 4.5	97.1 ± 2.3	0.4 ± 0.2

As expected, the use of high C₁₀P amount leads to the formation of more resistant layers. Among all the conditions, the layers made of 20 and 50% of BUPA

exhibit the best inhibition efficiencies (IE) with respective values of 98.7 and 98.9%, hence the best corrosion resistance.

Cyclic voltammetry (CV) (Figure 5.6 - Table 5.2 - Supporting information Figure A.7) confirms the protective efficiency due to BUPA and C₁₀P grafting, as well as the reinforcement of the TiO₂ external layer.

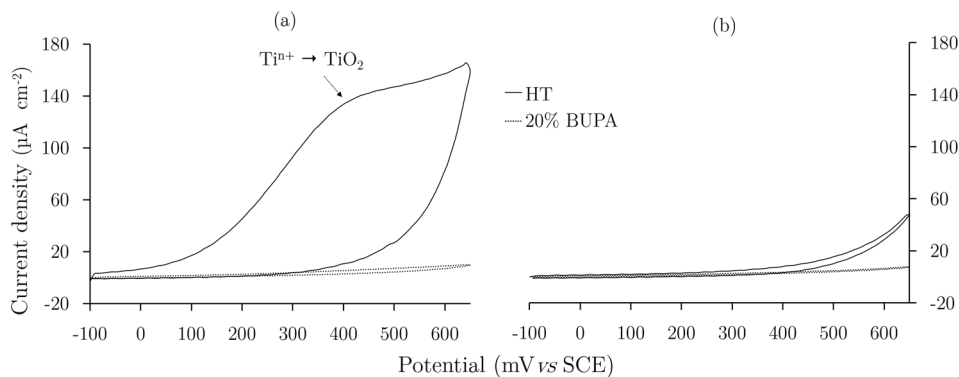


Figure 5.6. Representative first (a) and second (b) cycles of the voltammograms for HT-NiTi and BUPA/C₁₀P (20/80) in 0.1 M NaOH at a scan rate of 20 mV s⁻¹.

For bare NiTi substrate, the first cycle reveals two anodic peaks at 200 and 500 mV vs SCE, respectively assigned to Tiⁿ⁺ and Ni²⁺ oxidations, but only one cathodic peak assigned to Ni³⁺ reduction. On the second cycle, only nickel oxidation and reduction peaks are still present due to the irreversible passivation of the electrode via the titanium oxide layer. For HT-NiTi, only the oxidation peak of Tiⁿ⁺ can be observed on the first cycle and no more Ni reactions, even during the second cycle. This confirms the efficiency of the hydrothermal treatment on the reinforcement of TiO₂ layer and on the prevention of Ni^{x+} release. Once electroassisted grafting of BUPA/C₁₀P is performed on HT-NiTi, their CV analyses do not show any electrochemical activity, thus confirming the protective efficiency of the grafted phosphonic derivatives. As expected, the increase of C₁₀P concentration within the layer leads to the formation of more blocking layers. In line with the conclusions made from LSV results, BUPA/C₁₀P ratios of 50/50 and 20/80 exhibit the best blocking factors, thus the best protection of the substrate.

SECM is used to assess the charge transfer process occurring at Bare-NiTi, HT-NiTi, and BUPA/C₁₀P-NiTi electrodes during the reduction of FcMeOH⁺. Figure 7 and Figure A.8 (Supporting information) show the normalized approach curves in feedback mode. The curves are fitted on general analytical expressions given for first-order heterogenous finite kinetics^{19,20} at the sample surface with respect to the FcMeOH⁺ generated at the tip surface.

The apparent charge transfer rate constants (k_{ct} - Table 5.2) attest the regeneration rate of FeMeOH by the NiTi samples evolves through the modification steps. The obtained values of k_{ct} are in line with the results presented for CV. Indeed, the hydrothermal passivation of NiTi leads to the formation of a slightly more protective oxide layer, as attested by a k_{ct} down from 16.0 to 10.8 $\mu\text{m s}^{-1}$. This phenomenon is amplified by the additional presence of BUPA/C₁₀P monolayers, with k_{ct} ranging from 0.4 to 10.5 $\mu\text{m s}^{-1}$. Among the assessed BUPA/C₁₀P ratios, the best results are obtained for the coatings with 0, 60, 80 and 20% BUPA with respective k_{ct} of 0.4, 0.4, 0.5 or 0.6 $\mu\text{m s}^{-1}$.

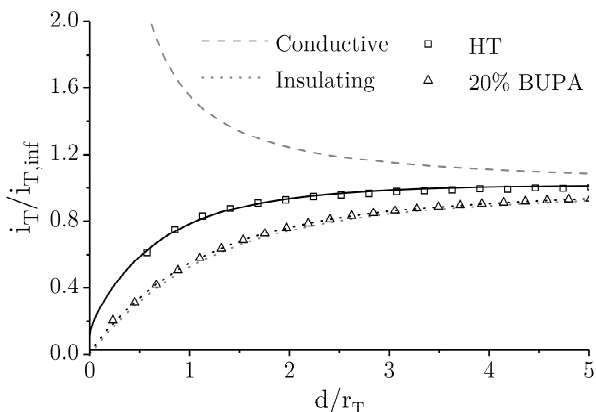


Figure 5.7. Representative normalized SECM FB approach curves for HT-NiTi ($k_{ct}=11.2$), BUPA/C₁₀P-NiTi (20/80) ($k_{ct}=0.6$) in 1 mM FeMeOH / 0.1 M KNO₃. The tip was set at 0.4 V vs Ag|AgCl and moved at a scan rate of 1 $\mu\text{m s}^{-1}$. The symbols correspond to the experimental curves and the solid lines to the SECM theory.^{19,20}

From these results, the optimum BUPA/C₁₀P layer (high P/NiTi, Br/NiTi, BF, IE, k_{ct} , and reproducibility) is prepared from 20% of BUPA and 80% of C₁₀P. This molecular ratio will be used for all the upcoming fonctionnalisations.

5.4 SI-ATRP of MPC on BUPA/C₁₀P-covered NiTi

In this section, SI-ATRP of MPC is performed on the BUPA/C₁₀P-NiTi (modified in the optimum conditions determined above (*i.e.* $E = 1.2$ V vs SCE, $t = 5$ min, BUPA/C₁₀P = 20/80) for 1, 3 and 6 h (PMPC-NiTi). The so-modified substrates are characterized with water contact angle measurements, PM-IRRAS, XPS, SEM, LSV and SECM to attest to polymerization efficiency.

The modified surfaces are first characterized using water contact angle (Figure 5.8). More hydrophilic surfaces ($\theta_w = 45^\circ$) are obtained for PMPC-NiTi compared to BUPA/C₁₀P-NiTi (78.9°) which attests, considering the hydrophilic nature of the MPC, the formation of the polymer from the surface.

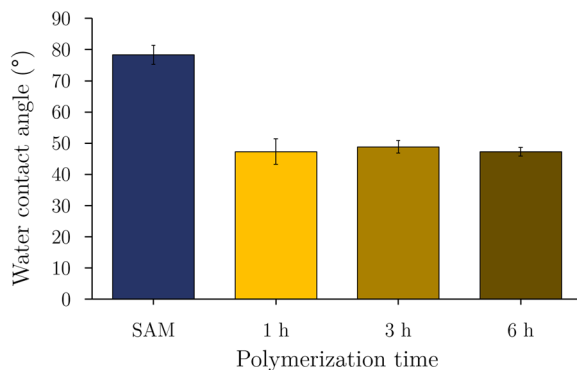


Figure 5.8. Water contact angles obtained for BUPA/C₁₀P-NiTi (20/80) and PMPC-NiTi prepared during 1, 3 or 6 h.

Figure 5.9 shows the PM-IRRAS spectra. For PMPC-NiTi coatings, absorptions bands in agreement with the structure of the molecules appears at 1721, 1486, 1255-1279, 1170, 1125, 1092 and 1054 cm⁻¹, respectively assigned to C=O_{stretch} (ester), C-O-C_{wag}, C-O_{asym stretch} (ester), C-O_{sym stretch} (ester), C-N_{stretch}, C-O_{stretch} (alcohol), and P-O_{stretch}. An increased signal is noticed, especially after 6 h of polymerization, which confirms the presence of a PMPC films on NiTi surface.

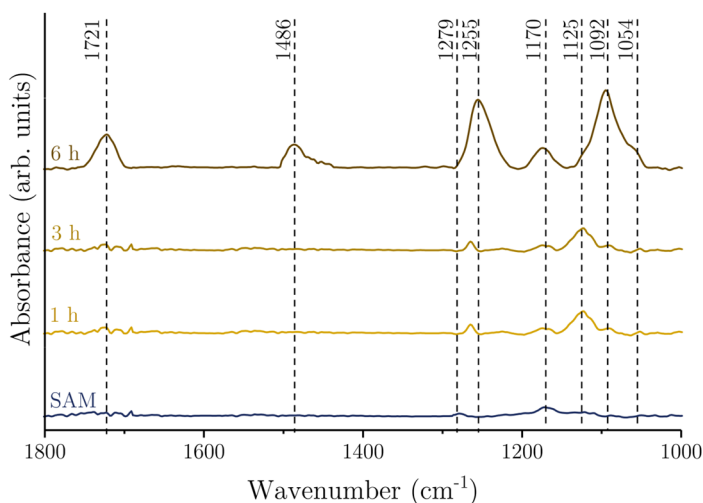


Figure 5.9. PM-IRRAS for BUPA/C₁₀P-NiTi (20/80) and PMPC-NiTi prepared during 1, 3 or 6 h.

XPS analyses confirm the formation of PMPC. Figure 5.10 presents C1s and N1s core-levels spectra for PMPC-NiTi and BUPA/C₁₀P-NiTi. As expected, C1s and N1s peaks are more intense after SI-ATRP of MPC and present different general shapes compared to the initial BUPA/C₁₀P-NiTi. The C1s core level spectra

(Figure 5.10 - left) present four components centred at 285.0, 285.7, 286.5 and 289.1 eV, respectively attributed to carbon atoms involved in C-H/C-C, C-N, C-O/C-P and O-C=O bonds present in BUPA, C₁₀P, PMPC and Me₆TREN. The peak at 283.3 eV (*) assigned previously to an artefact from the spectrometer is still visible.

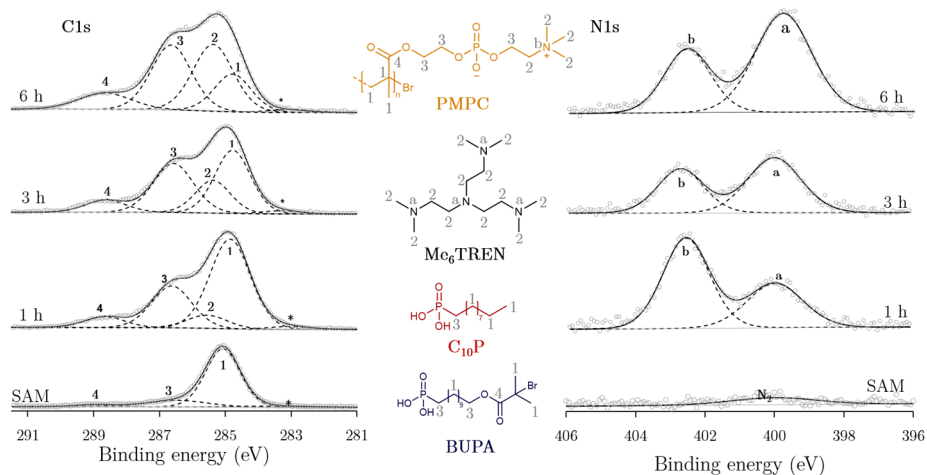


Figure 5.10. XPS general shape of core spectra for C1s and N1s components obtained for BUPA/C₁₀P (20/80) and PMPC-NiTi prepared during 1, 3 or 6 h.

The N1s core level spectra (Figure 5.10 - right) present two components centred at energies of 400.3 eV and 403.5 eV, respectively attributed to nitrogen atoms characteristic of the amine function of the Me₆TREN and of the ammonium present in PMPC. These confirms the efficiency of SI-ATRP of MPC on BUPA/C₁₀P (20/80) layer but also point out the presence of residues of the catalyst (complexed by Me₆TREN) trapped in the coating.

SEM images (Figure 5.11) highlight differences of modified NiTi morphologies as a function of the polymerization time. Within short polymerization time (1 h) the surface is highly inhomogeneous and shows a high density of polymer aggregates. After 3 h, the coating starts to be more homogenous but uncovered NiTi domains are still visible. However, the formation of PMPC film during 6 h lead to a good coverage with a quite uniform distribution of small aggregation spots probably resulting from non-uniform PMPC growth.

The increase of the hydrophylicity of PMPC-NiTi and the time dependent homogeneity of the surface induce differences in the electrochemical properties are shown in the LSV curves (Figure 5.12) and SECM images (Figure 5.13).

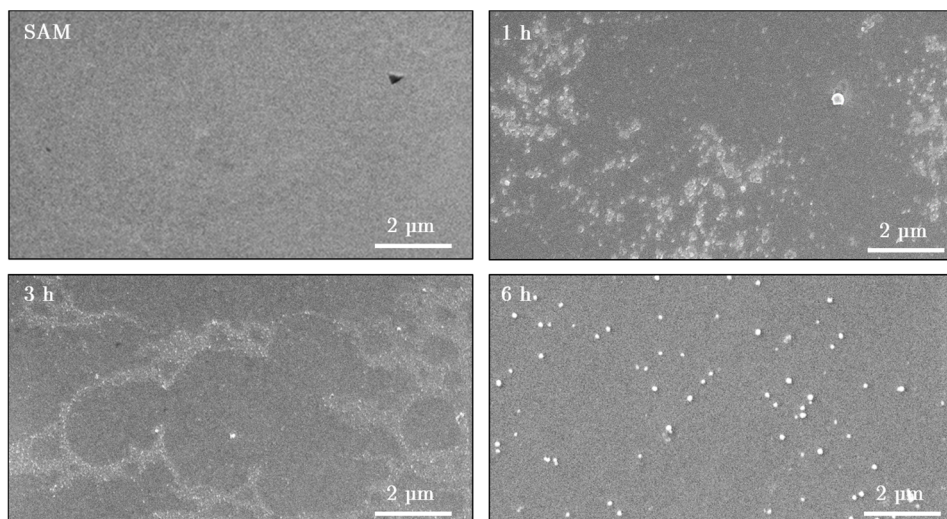


Figure 5.11. SEM images for BUPA/C₁₀P (20/80) and PMPC-NiTi prepared during 1, 3 or 6 h (obtained in secondary electron imaging mode).

For the substrate modified during 1 h, j_{corr} changes from 9.4 nA cm^{-2} (BUPA/C₁₀P-NiTi) to a value of 92.5 nA cm^{-2} as well as less negative E_{corr} (from -314 to -82 mV vs SCE) due to the high hydrophilicity and inhomogeneity of the PMPC layer. For higher SI-ATRP times, j_{corr} values are 12.0 nA cm^{-2} and 17.8 nA cm^{-2} for 3h and 6h, respectively. E_{corr} values remain in the same range with values of -110 and -153 mV vs SCE .

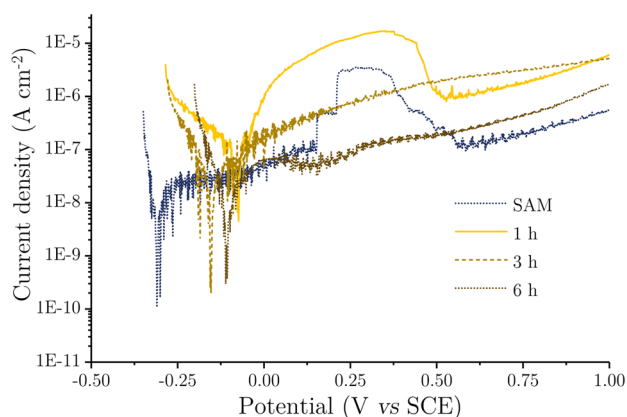


Figure 5.12. Polarization curves for BUPA/C₁₀P NiTi (20/80) and PMPC-NiTi prepared during 1, 3 or 6 h (obtained in 0.5 M NaCl at a scan rate of 1 mV s^{-1}).

Nevertheless compared to HT-NiTi ($j_{\text{corr}} \sim 103.6 \text{ nA cm}^{-2}$, $IE \sim 88.1$ and $E_{\text{corr}} \sim -266 \text{ mV vs SCE}$), the corrosion current and inhibition efficiency still indicates an improvements of the corrosion inhibition properties.

Representative SECM mapping images collected in FB mode are presented in Figure 13. Those point out the surface uniformity and the passivating behaviour of BUPA/C₁₀P SAM (Figure 13 – upper left). However, once SI-ATRP of MPC occurred, the average measured current increases up from ~ 0.2 to ~ 0.4 nA with a slightly less homogeneous behaviour. These results are in line with the previous observations made from SEM pictures (Figure 5.11) and LSV curves (Figure 5.12). The increased PMPC thickness induces an heterogeneous electroactivity especially for the 6 h polymerization, where several high current spots are noticeable. The increased electroreactivity is in accordance with the hydrophilic behaviour of PMPC coatings and thus the interactions between the coating and the redox probe, thus resulting in an intercalation of the probe inside the organic layer. In 2010, Matrab *et al.* investigated the transport and the reactivity within poly(glycidyl methacrylate) polymer brushes made by SI-ATRP and proved the permeability of such methacrylate-based polymer once solvated in aqueous media.²¹

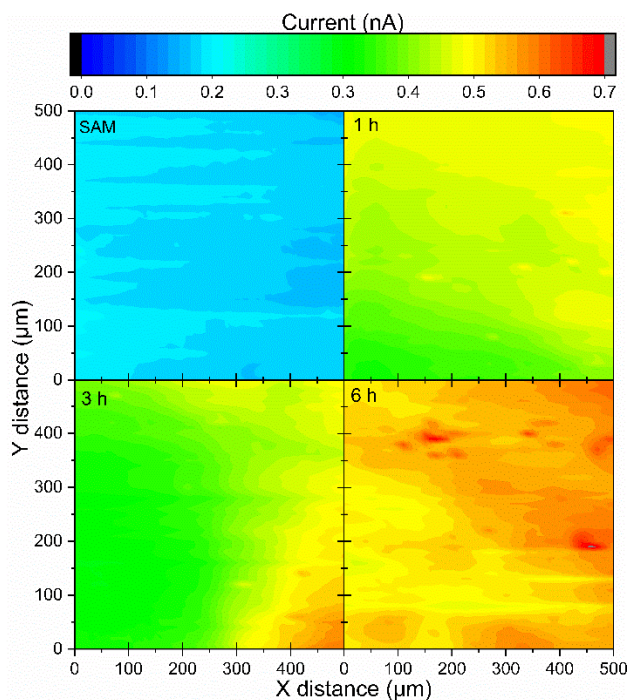


Figure 5.13. Normalized SECM FB mapping for BUPA/C₁₀P NiTi (20/80) and PMPC-NiTi prepared during 1, 3 or 6 h (obtained in 1 mM FeMeOH / 0.1 M KNO₃).

5.5 Conclusions

In this chapter, the electro-assisted grafting of BUPA/C₁₀P mixed monolayers in various ratios has been achieved to improve NiTi corrosion resistance.

First, the successful surface modifications have been attested by WCA, PM-IRRAS and XPS results and it has been proven that the substitution of some BUPA molecules by C₁₀P (a smaller and less hindered molecule) improve the anti-corrosion properties of Nitinol. Among all the tested conditions, the most protective and efficient layer (high blocking factor, high inhibition efficiency, low charge transfer constant k_{ct}) is obtained for a composition of 20% BUPA and 80 % C₁₀P.

Second, the surface-initiated ATRP of MPC has been achieved for 1, 3 or 6 h on the so-formed initiating layer. SEM images and SECM measurements evidenced the non-uniformity of the PMPC coatings for time lower than 6 h.

This part of the work opens the prospect of biocompatible polymers growth and tuning on Nitinol substrate modified by electrografted phosphonic-made ATRP initiators. Nevertheless, the structure of this system still requires some improvements with the prospect of a further biomedical application, as well is being evaluated in body simulated fluids.

References

- (1) Arrotin, B.; Delhalle, J.; Dubois, P.; Mespouille, L.; Mekhalif, Z. Electroassisted Functionalization of Nitinol Surface, a Powerful Strategy for Polymer Coating through Controlled Radical Surface Initiation. *Langmuir* **2017**, *33* (12), 2977–2985.
- (2) Gupta, R. K.; Singh, R. A. Inhibition of Corrosion by Poly(N-Hexadecylaniline)/Docosanol Mixed Langmuir–Blodgett Films on Copper in Sea Water. *Mater. Chem. Phys.* **2006**, *97* (2–3), 226–229.
- (3) Li, C.; Li, L.; Wang, C. Study of the Inhibitive Effect of Mixed Self-Assembled Monolayers on Copper with SECM. *Electrochim. Acta* **2014**, *115*, 531–536.
- (4) Barthélémy, B.; Maheux, S.; Devillers, S.; Kanoufi, F.; Combellas, C.; Delhalle, J.; Mekhalif, Z. Synergistic Effect on Corrosion Resistance of Phynox Substrates Grafted with Surface-Initiated ATRP (Co)Polymerization of 2-Methacryloyloxyethyl Phosphorylcholine (MPC) and 2-Hydroxyethyl Methacrylate (HEMA). *ACS Appl. Mater. Interfaces* **2014**, *6* (13), 10060–10071.
- (5) Barthélémy, B.; Kanoufi, F.; Combellas, C.; Delhalle, J.; Mekhalif, Z. Phynox Improved Corrosion Resistance with MPC Initiated from Mixed Monolayers of Phosphonic Acids. *J. Electrochem. Soc.* **2014**, *161* (12), C1–C6.
- (6) Wittstock, G.; Burchardt, M.; Pust, S. E.; Shen, Y.; Zhao, C. Scanning Electrochemical Microscopy for Direct Imaging of Reaction Rates. *Angew. Chemie - Int. Ed.* **2007**, *46* (10), 1584–1617.
- (7) Fan, F.-R. F.; Fernandez, J.; Liu, B.; Mauzeroll, J. Scanning Electrochemical Microscopy. In *Handbook of Electrochemistry*; Zoski, C. G., Ed.; Elsevier, 2007.
- (8) Bedioui, F.; Griveau, S.; Pailleret, A. Microscopie Électrochimique. *Tech. l'ingénieur* **2009**.
- (9) Izquierdo, J.; Knittel, P.; Kranz, C. Scanning Electrochemical Microscopy: An Analytical Perspective. *Anal. Bioanal. Chem.* **2018**, *410* (2), 307–324.

- (10) Maho, A.; Kanoufi, F.; Combellas, C.; Delhalle, J.; Mekhalif, Z. Electrochemical Investigation of Nitinol/Tantalum Hybrid Surfaces Modified by Alkylphosphonic Self-Assembled Monolayers. *Electrochim. Acta* **2014**, *116*, 78–88.
- (11) Li, C.; Li, L.; Wang, C.; Zhu, Y.; Zhang, W. Study of the Protection Performance of Self-Assembled Monolayers on Copper with the Scanning Electrochemical Microscope. *Corros. Sci.* **2014**, *80*, 511–516.
- (12) Estrada-Vargas, A.; Bandarenka, A.; Kuznetsov, V.; Schuhmann, W. In Situ Characterization of Ultrathin Films by Scanning Electrochemical Impedance Microscopy. *Anal. Chem.* **2016**, *88* (6), 3354–3362.
- (13) Yu, H.; Li, C.; Yuan, B.; Li, L.; Wang, C. The Inhibitive Effects of AC-Treated Mixed Self-Assembled Monolayers on Copper Corrosion. *Corros. Sci.* **2017**, *120*, 231–238.
- (14) Matrab, T.; Hauquier, F.; Combellas, C.; Kanoufi, F. Scanning Electron Microscopy Investigation of Molecular Transport and Reactivity within Polymer Brushes. *ChemPhysChem* **2010**, *11* (3), 670–682.
- (15) Blanchard, P. Y.; Sun, T.; Yu, Y.; Wei, Z.; Matsui, H.; Mirkin, M. V. Scanning Electrochemical Microscopy Study of Permeability of a Thiolated Aryl Multilayer and Imaging of Single Nanocubes Anchored to It. *Langmuir* **2016**, *32* (10), 2500–2508.
- (16) Schulte, A.; Belger, S.; Etienne, M.; Schuhmann, W. Imaging Localised Corrosion of NiTi Shape Memory Alloys by Means of Alternating Current Scanning Electrochemical Microscopy (AC-SECM). *Mater. Sci. Eng. A* **2004**, *378* (1–2 SPEC. ISS.), 523–526.
- (17) Izquierdo, J.; González-Marrero, M. B.; Bozorg, M.; Fernández-Pérez, B. M.; Vasconcelos, H. C.; Santana, J. J.; Souto, R. M. Multiscale Electrochemical Analysis of the Corrosion of Titanium and Nitinol for Implant Applications. *Electrochim. Acta* **2016**, *203*, 366–378.
- (18) Socrates, G. *Infrared and Raman Characteristic Group Frequencies: Tables and Charts*, Third Edit.; John Wiley & Sons, 2004.
- (19) Wei, C.; Bard, A. J.; Mirkin, M. V. Scanning Electrochemical Microscopy. 31. Application of SECM to the Study of Charge Transfer Processes at the Liquid/Liquid Interface. *J. Phys. Chem.* **1995**, *99* (43), 16033–16042.
- (20) Cannes, C.; Kanoufi, F.; Bard, A. J. Cyclic Voltammetry and Scanning Electrochemical Microscopy of Ferrocenemethanol at Monolayer and Bilayer-Modified Gold Electrodes. *J. Electroanal. Chem.* **2003**, *547* (1), 83–91.
- (21) Matrab, T.; Hauquier, F.; Combellas, C.; Kanoufi, F. Scanning Electron Microscopy Investigation of Molecular Transport and Reactivity within Polymer Brushes. *ChemPhysChem* **2010**, *11*, 670–682

Chapter 6

Evaluation of Nitinol behavior in physiological conditions:
a step towards biomedical applications

6.1	Introduction	97
6.2	Experimental section	97
6.2.1.	Preparation of body simulated fluid	97
6.2.2.	Growth of endothelial cells	98
6.3	Nitinol behavior in physiological medium.....	98
6.4	Growth of endothelial cells	100
6.5	Conclusions	101
	References	101

6.1 Introduction

This chapter focuses on the behavior of bare and modified Nitinol substrates in physiological conditions. In this context, the following results are divided into two sections.

The first one is dedicated to the corrosion properties of Bare-NiTi, HT-NiTi, BUPA/C₁₀P-NiTi and PMPC NiTi, and the potential subsequent leaching of Ni²⁺ ions. The NiTi materials are thus exposed to human blood plasma simulated body fluid for up to 6 weeks, and their corrosion is assessed by LSV and EIS, whereas the amount of released nickel is evaluated by optical emission spectroscopy coupled with inductively coupled plasma (ICP-OES).

In the second part, the ability of Bare-NiTi, HT-NiTi, BUPA/C₁₀P-NiTi and PMPC NiTi to grow endothelial cells is assessed by immunofluorescence.

6.2 Experimental section

6.2.1. Preparation of body simulated fluid

The ionic composition of human blood plasma (Table 6.1) can be reached through the preparation of a simulated body fluid (BSF) solution (Table 6.2).

Table 6.1. Ion concentration of human blood plasma.¹

Ion	Concentration (mM)
Na ⁺	142.0
K ⁺	5.0
Mg ²⁺	1.5
Ca ²⁺	2.5
Cl ⁻	103.0
HCO ₃ ⁻	27.0
HPO ₄ ²⁻	1.0
SO ₄ ²⁻	0.5

Table 6.2. Composition of prepared blood plasma SBF (for 1 L).¹

Reagents	Amount (g)
HEPES	11.928
NaCl	5.403
NaHCO ₃	0.40
Na ₂ CO ₃ • 10 H ₂ O	5.524
KCl	0.225
K ₂ HPO ₄	0.176
MgCl ₂ • 6 H ₂ O	0.311
CaCl ₂	0.293
Na ₂ SO ₄	0.072

The preparation of such fluid is done according to the procedure described by Oyane *et al.*¹ as followed. First, all the used glassware is washed with 1.0 M HCl, neutral detergent, and ultra-pure milliQ water. HEPES is first dissolved into 100 mL of ultra-pure water, whereas all the other compounds are used as such. 700 mL of ultra-pure milliQ-water are stirred at 36.5°C, and all the reagents are then dissolved in the sequence listed in Table 6.2. The volume is then adjusted to 1 L and

fluid is adjusted to a pH of 7.40 using aqueous 1.0 M NaOH and cooled down at 20°C.

6.2.2. Growth of endothelial cells

EA.hy926 endothelial cells (hybrid cells resulting from the fusion of human endothelial cells and lung carcinoma cells) are seeded on 1 cm² of Bare-NiTi, HT-NiTi, BUPA/C₁₀P-NiTi and PMPC-NiTi in a 6-wells plate with around 50 000 cells by well for 24h, 48h and 72h. After the exposure, each well is rinsed with phosphate buffered saline and the incubation is performed in a solution containing 0.5 ‰ Calcein AM and 2‰ Ethidium homodimer (LIVE/DEAD™ Viability/Toxicity Kit for mammalian cells, L3224, Invitrogen ThermoFisher) for 30 minutes at room temperature and away from light. The substrates are finally rinsed with phosphate buffered saline and observed by fluorescence microscopy. For reproducibility purposes, each test is performed three times. The number of living cells on the material is finally evaluated using ImageJ software.

6.3 Nitinol behavior in physiological medium

In this section, the behavior of Bare-NiTi, HT-NiTi, BUPA/C₁₀P-NiTi and PMPC in human blood plasma simulated fluid is assessed for various immersion length ranging from 0 to 6 weeks. Directly after the immersion, open circuit potential of the substrates is determined after one hour of equilibration (Table 6.3), whereas the amount of nickel released into the BSF solution is determined by ICP (Table 6.4).

Table 6.3. Open circuit potential (in mV vs SCE) of Bare-NiTi, HT-NiTi, BUPA/C₁₀P-NiTi and PMPC-NiTi after immersion in SBF of different length.

Time (week)	Bare-NiTi	HT-NiTi	BUPA/C ₁₀ P-NiTi	PMPC-NiTi
0	-289	-259	-206	-175
1	-370	-352	-300	-165
2	-354	-322	-282	-199
3	-330	-212	-175	-122
4	-367	-224	-146	-125
5	-250	-237	-207	-139
6	-256	-233	-220	-123

Before immersion in the BSF solution, the materials OCP increase with the number of modification, *i.e.* in increasing order Bare-NiTi (-289 mV), HT-NiTi (-259 mV), BUPA/C₁₀P-NiTi (-206 mV) and PMPC-NiTi (-175 mV), which confirms the improvement of Nitinol through the modification steps. These results are in line

with the analyses performed in 0.5 M NaCl and previously presented. The phenomenon can be similarly seen for all the tested immersion time.

After one week of exposure, Bare-NiTi, HT-NiTi and BUPA/C₁₀P-NiTi exhibit lower OCP, which is significative of a less efficient resistance of the materials to corrosion in the BSF. Such decrease of the OCP is also present for HT-NiTi, but later after 2 weeks of immersion, thus confirming the efficiency of PMPC-NiTi over Bare-NiTi and its subsequent intermediate modification steps.

Within the following weeks, the OCP of all materials temporarily increased. This increased corrosion resistance is explained by the formation and precipitation of corrosion products onto the surface, thus partially hindering the surface, and reducing the number of corrosion sites. Indeed, many corrosion products can be formed due to the variety of anions present in the used BSF, *e.g.* NiCl₂, NiSO₄, Ni(OH)₂ or NiO.² However, after a while, the OCP values tends to decrease again due to local corrosion.

The evolution of OCP as well as the precipitation of corrosion products is confirmed by the ICP results (Table 6.4). After one week of immersion in the BSF, the released amount of nickel obtained, in decreasing order, for Bare-NiTi (126 ppb), HT-NiTi (34 ppb), BUPA/C₁₀P-NiTi (17 ppb) and PMPC-NiTi (13 ppb) are in line with the previous results and attest the efficiency of each modification step on the corrosion resistance of Nitinol.

Furthermore, similarly to the evolution of the OCP, the amount of nickel detected by ICP fluctuates for all the substrates. This is a further proof of the precipitation of corrosion products onto the surface, until the corrosion process increases again, as seen by the increased amount of detected nickel.

Table 6.4. Released nickel (in ppb cm⁻²) of Bare-NiTi, HT-NiTi, BUPA/C₁₀P-NiTi and PMPC-NiTi after immersion in SBF of different length.

Time (week)	Bare-NiTi	HT-NiTi	BUPA/C ₁₀ P-NiTi	PMPC-NiTi
1	126	34	17	13
2	97	63	17	42
3	50	42	-	-
4	59	21	-	-
5	97	38	29	4
6	84	25	34	4

However, such precipitation of corrosion products cannot easily happen in the human body as the material would be located in a fluctuating fluid, on the contrary of the stagnant solution used for this study, and is therefore not of concern.

6.4 Growth of endothelial cells

In order to assess the usability of the modified Nitinol in cardiovascular application, EA.hy926 endothelial cells have been grown on Bare-NiTi, HT-NiTi, BUPA/C10P-NiTi and PMPC-NiTi.

Figure 6.1 depicts the adhering living EA.hy926 endothelial cells onto on each kind of modified Nitinol substrates after 24h, 48h or 72h, whereas the number of so-detected cells is presented in Table 6.5.

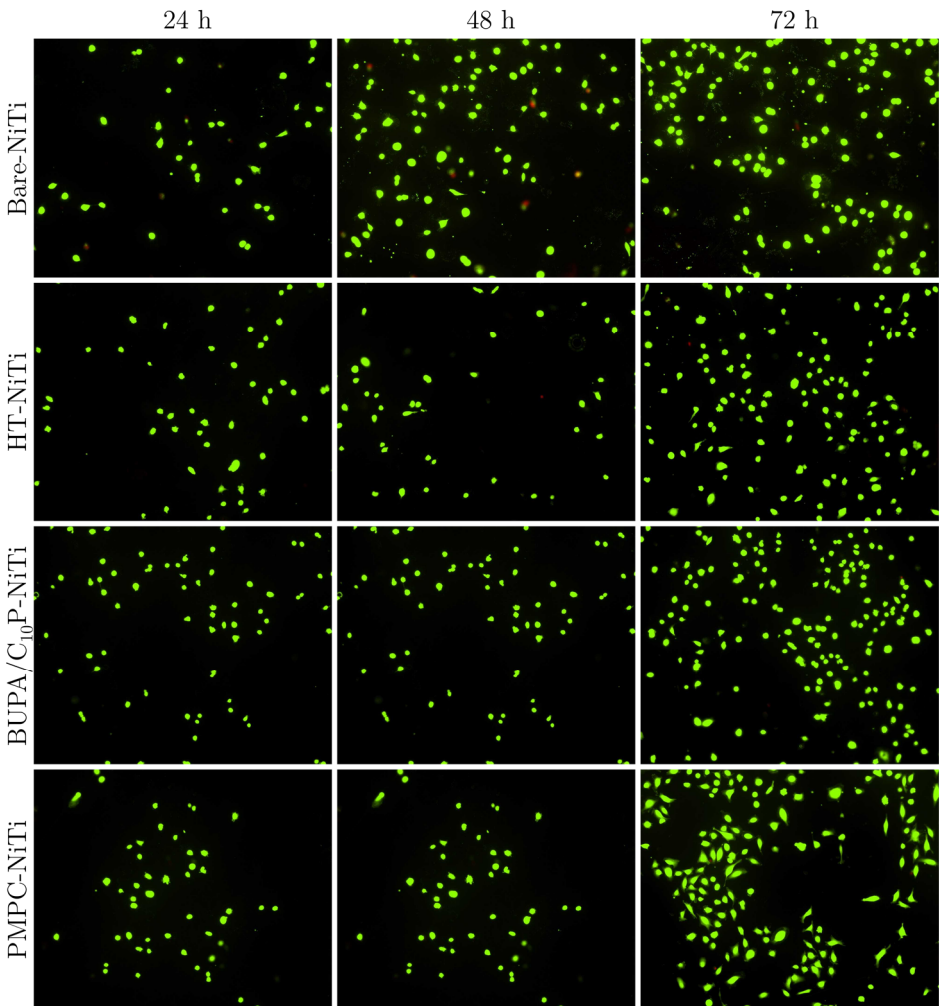


Figure 6.1. Living EA.hy926 endothelial cells observed by fluorescence microscopy on Bare-NiTi, HT-NiTi, BUPA/C₁₀P-NiTi and PMPC-NiTi.

Despite they point out to an increase in the number of adhering cells with exposure time, those results do not indicate any significant difference between

Bare-NiTi, HT-NiTi, BUPA/C₁₀P-NiTi and PMPC-NiTi over their ability to grow endothelial cells, which is probably due to the absence of any medical drug into the organic coating which would prevent from cell premature death.

Table 6.5. Number of living EA.hy926 endothelial cells observed by fluorescence microscopy on Bare-NiTi, HT-NiTi, BUPA/C₁₀P-NiTi and PMPC-NiTi.

Time (hours)	Bare-NiTi	HT-NiTi	BUPA/C ₁₀ P-NiTi	PMPC-NiTi
24	68 ± 25	54 ± 30	49 ± 15	17 ± 4
48	95 ± 30	59 ± 31	63 ± 21	66 ± 58
72	132 ± 63	138 ± 42	148 ± 37	174 ± 65

6.5 Conclusions

This chapter focused on the evaluation of bare and modified Nitinol substrates in biological media, especially through corrosion measurements and human endothelial cells growth.

First, it has been proven by the open-circuit potential as well as by the evaluated amount of released nickel ions that each modification step leads to an additional improvement of Nitinol corrosion resistance in human blood plasma simulated fluid. It was also demonstrated that a temporary passivation phenomenon occurs due to the precipitation of corrosion products. However, this phenomenon won't be possible in the context of cardiovascular stents as blood flow would clear them out.

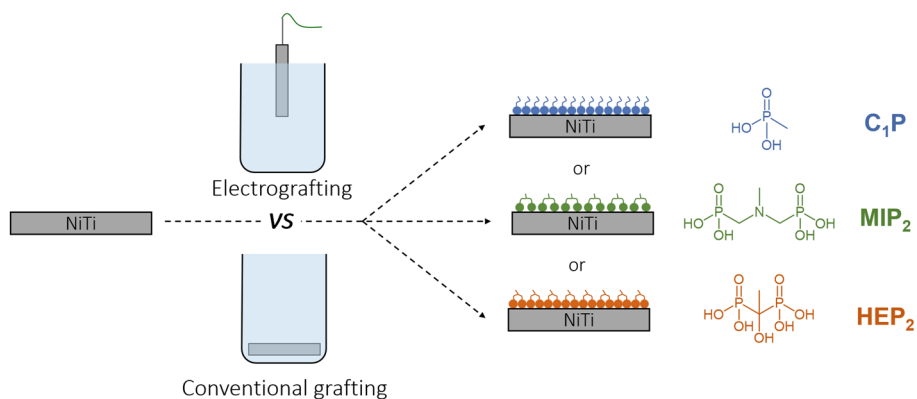
Second, a first attempts of human EA.hy926 endothelial cells growth was unsuccessfully performed on Bare-NiTi, HT-NiTi, BUPA/C₁₀P-NiTi and PMPC-NiTi, thus attesting their inefficiency for cardiovascular applications. This could be improved by modifying the architecture of the polymer coating, as well as by incorporating drugs of interest. So far, further improvement of the coating is thus still required.

References

- (1) Oyane, A.; Kim, H. M.; Furuya, T.; Kokubo, T.; Miyazaki, T.; Nakamura, T. Preparation and Assessment of Revised Simulated Body Fluids. *J. Biomed. Mater. Res. - Part A* **2003**, *65* (2), 188–195.
- (2) Haynes, W. M.; Lide, D. R.; Bruno, T. J. *CRC Handbook of Chemistry and Physics*; 2016.

Chapter 7

Elaboration of bisphosphonic acids coatings on Nitinol:
an alternative to mixed monolayers



7.1	Introduction	105
7.2	Experimental section	106
	7.2.1. Conventional grafting of organophosphonic derivatives on Nitinol.	106
	7.2.2. Electro-assisted grafting organophosphonic derivatives on Nitinol .	106
7.3	Mono- <i>vs</i> bisphosphonic anchoring group	106
7.4	Transposition to derivatives bearing alkyl chains	110
	7.4.1. Methylphosphonic <i>vs.</i> dodecylphosphonic derivatives	110
	7.4.2. Repulsion of non-grafted incorporated molecules	112
7.5	Conclusions	113
	References	113

7.1 Introduction

Chapter 5 was devoted to the use of mixed monolayers resulting from the co-adsorption of two organophosphonic acid derivatives differing in length and/or terminal functional groups to improve the corrosion resistance as well as the layer organization. However, despite it is efficient, this methodology also has some inconvenient. First, it is difficult to predict the organization of the so-formed layer. Second, it is impossible to control the distribution of both molecules and to insure the homogeneity of the coating.

The present exploratory work investigates the grafting on NiTi of short tail mono- and bisphosphonic acid derivatives, which could be an alternative to the mixed monolayers approach, to find the most efficient anchoring group to be used in molecules of biological interests. For this purpose, surface modifications based on bisphosphonic acid derivatives (*i.e.* (methylimino)dimethylene-bisphosphonic acid, MIP₂) and (1-hydroxyethylidene-1,1-diphosphonic acid, HEP₂) have been studied both by conventional (CH) and electro-assisted (EG) grafting approaches and compared to a monophosphonic acid derivative (methylphosphonic acid, C₁P) (Figure 7.1).

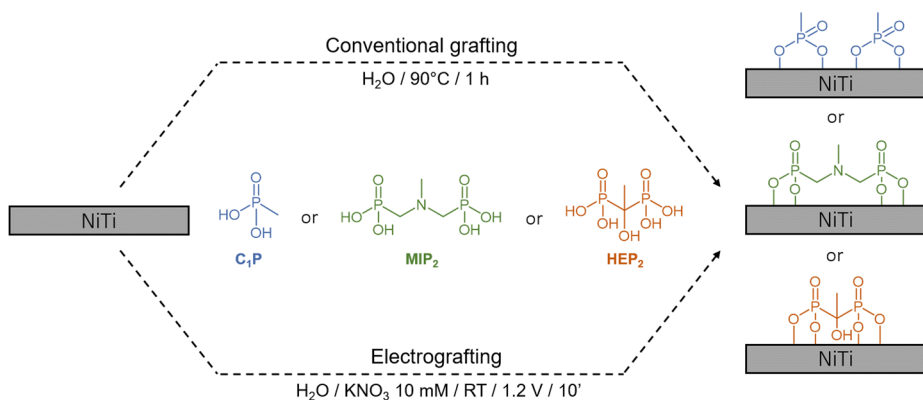


Figure 7.1. Schematic representation of the surface modification of Nitinol (NiTi) by conventional (CH) or electro-assisted (EG) grafting of phosphonic acid derivatives.

Subsequently, the second part of this chapter is devoted to the application of the best anchoring group to a classical molecule used for the elaboration of SAMs. Among the most classical molecules used for the elaboration of SAMs contains between 8 and 14 carbons alkyl chains to insure the interactions between the chains and the best efficiency. In this context, coatings made of bisphosphonic acid derivative with a 12-carbons alkyl chain, *i.e.* (dodecylimino)dimethylene-bisphosphonic acid (DIP₂ - Figure 7.2a) is investigated and compared to the classical 1-dodecylphosphonic acid (C₁₂P - Figure 7.2b).

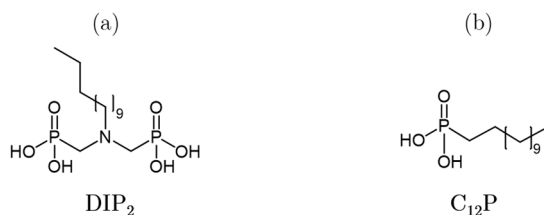


Figure 7.2. Chemical structures of (dodecylimino)dimethylene-bisphosphonic acid (a) and 1-dodecylphosphonic acid (b).

7.2 Experimental section

7.2.1. Conventional grafting of organophosphonic derivatives on Nitinol

The thermally assisted grafting (CH) on HT-NiTi is achieved by its immersion (1 h at 90°C) in 20 mL of 1 mM of the organophosphonic derivative (C₁P, MIP₂ or HEP₂) aqueous solution.¹ The substrates are then ultrasonically cleaned in denatured ethanol for 15 min before being blown dried under nitrogen.

7.2.2. Electro-assisted grafting organophosphonic derivatives on Nitinol

Solutions (20.0 mL) composed of 1 mM of the organophosphonic derivative (C₁P, MIP₂, HEP₂, C₁₂P or DIP₂) and 10 mM KNO₃ are prepared in ultra-pure milli-Q water. Electroassisted grafting (EG) on HT surface is obtained by immersion of the substrate in the solution for 10 min, under a voltage of 1.2 V *vs* a saturated calomel electrode (SCE).¹

7.3 Mono- *vs* bisphosphonic anchoring group

C₁P, HIP₂ and MIP₂ are used to assess the grafting efficiency on the hydrothermally treated NiTi (HT) via the conventional (CH) and the electro-assisted (EG) processes with a particular attention on the anchoring group size impact on NiTi corrosion resistance. The footprint size, estimated from molecular modelling (Figure 7.4), of the monophosphonic C₁P and the bisphosphonic derivatives, HIP₂ and MIP₂, are 2.8, 6.1 or 8.4 Å, respectively. These molecules are grafted on HT NiTi plates by the conventional (CH) and electro-assisted (EG).

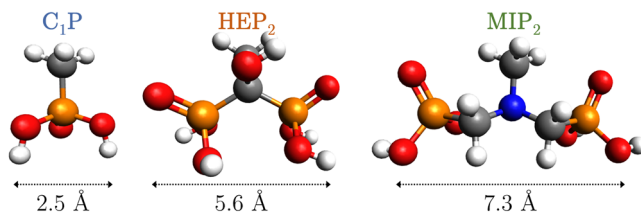


Figure 7.3. Simulated structures and estimated width of C₁P, HEP₂ and MIP₂.

In Figure 7.5 are given the water contact angle (WCA) values. It is observed that, comparatively to HT and irrespective of the modification process (CH and EG), these values are slightly higher in the case of C_1P and MIP_2 and similar (or slightly smaller) for HEP_2 . This is consistent with the presence of the -OH and of the $-CH_3$ head group carried out by HEP_2 and by C_1P and MIP_2 , respectively (Figure 1). Moreover, the similar contact angle between the oxidized surface ($EG_0 - 22.2^\circ \pm 2.7^\circ$) and HEP_2 -covered NiTi ($22.2^\circ \pm 4.6^\circ$) can be explained by the presence of -OH group on HEP_2 and the potential hydroxylation of the oxide layer through EG_0 .

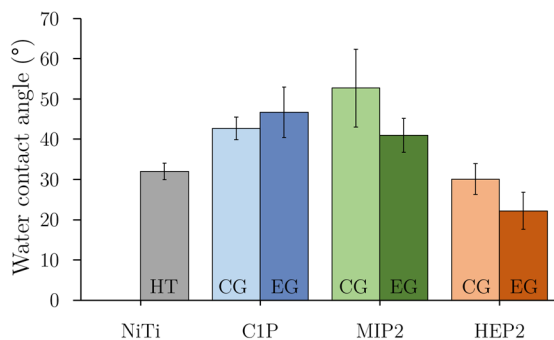


Figure 7.4. Water contact angles for HT NiTi, C_1P , MIP_2 and HEP_2 .

XPS analyses performed on HT, C_1P , MIP_2 and HEP_2 confirm the successful modification of HT NiTi through the appearing signal of P2p and through the general shape of the obtained spectra for C1s core level as presented in Figure 7.5. These samples exhibit peaks at similar energies but with higher intensities in the case of modified NiTi with organophosphonic derivatives, indicating a successful organic modification of the surface alloy. The peaks at energies of 285, 286.5, 287.7 and 289.1 eV correspond respectively to carbon atoms involved in C-H/C-C, C-O/C-P/C-N, C=O, and O-C=O bonds present in the grafted molecules and contributions from atmospheric contaminations. The increase of the peak at 286.5 eV is particularly noticeable in the case of EG- MIP_2 and EG- HEP_2 . XPS Ti2p and Ni2p core-levels for CH and EG, whatever the grafted molecule, are consistent with the CG_0 and EG_0 results, namely the metallic components of the Ti2p and Ni2p peaks are drastically reduced in the case of the EG treatment.

The amount of NiTi is evaluated considering the total concentration of detected nickel and titanium (metallic and oxidized). The P/NiTi ratios are used to evaluate the amount of organic molecules grafted on NiTi surface. The evolution of these ratios (Table 7.1) first attests for a better grafting efficiency (higher P/NiTi ratios) for the EG process. The presence of more phosphonic groups and thus more negative charges on the MIP_2 and HEP_2 molecules promotes their migration towards the anodically polarized sample.

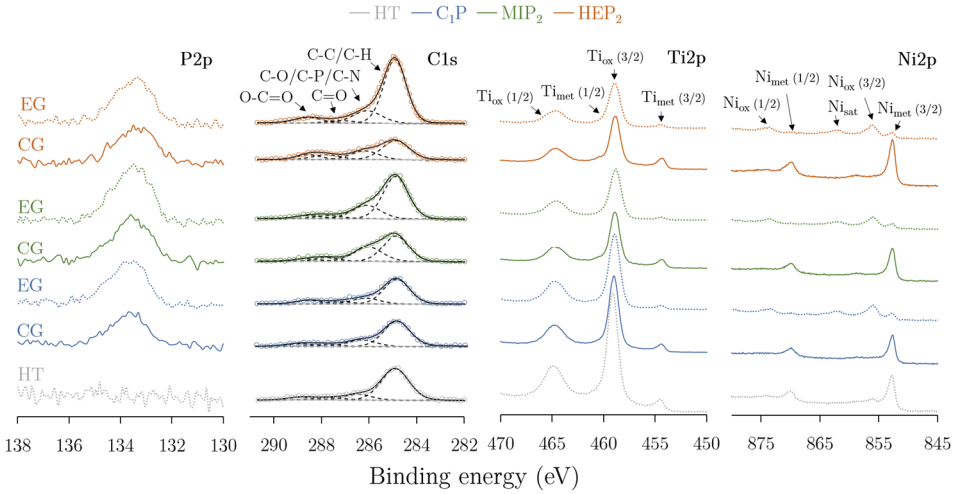


Figure 7.5. XPS core level spectra of P2p, C1s, Ti2p and Ni2p for HT NiTi, C₁P, MIP₂ and HEP₂.

Table 7.1. XPS atomic ratios for HT-NiTi and C₁P-NiTi, MIP₂-NiTi and HEP₂-NiTi.

Sample	P/NiTi	O/NiTi	Ni/NiTi	Ti/NiTi
HT	-	4.27 ± 0.70	0.15 ± 0.01	0.85 ± 0.01
C1P (CG)	0.02 ± 0.01	2.65 ± 0.56	0.18 ± 0.04	0.82 ± 0.04
C1P (EG)	0.05 ± 0.01	3.12 ± 0.21	0.13 ± 0.02	0.87 ± 0.02
MIP2 (CG)	0.09 ± 0.01	2.83 ± 0.23	0.21 ± 0.03	0.79 ± 0.03
MIP2 (EG)	0.14 ± 0.02	3.92 ± 0.36	0.15 ± 0.02	0.85 ± 0.02
HEP2 (CG)	0.08 ± 0.01	2.80 ± 0.23	0.30 ± 0.03	0.70 ± 0.03
HEP2 (EG)	0.12 ± 0.02	3.51 ± 0.90	0.15 ± 0.02	0.85 ± 0.02

Those results also attest for the formation of denser layers with bisphosphonic than with monophosphonic molecules (Figure 7.6). For the modification with organophosphonic derivatives (Table 2), the Ni/NiTi ratios (0.13-0.15) are lower and O/NiTi (3.12-3.92) ratios are higher for EG comparatively to CH. Ni/NiTi ratios for CH process are even higher (0.18) than for the HT treatment (0.15).

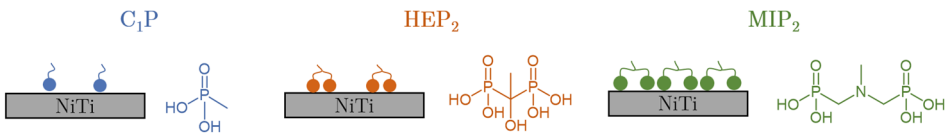


Figure 7.6. Schematic representation of the C₁P, HEP₂ and MIP₂ coatings obtained on HT NiTi.

The difference in the oxide layer composition between CH and EG processes and the nature of the grafting organophosphonic molecule have a synergetic effect and impact on NiTi corrosion resistance.

Figure 7.7 shows a significant difference between CH and EG, in particular in the anodic currents, which are quite similar to HT for CH samples while a huge decrease is noticed for the EG process. In Table 7.2 are listed the corrosion current densities, the corrosion potentials and inhibition efficiencies for all NiTi treatments. In particular it shows the superiority of C1P and MIP₂ made by EG, which confer to HT-NiTi a very good corrosion protection highlighted by an inhibition efficiency around 95%.

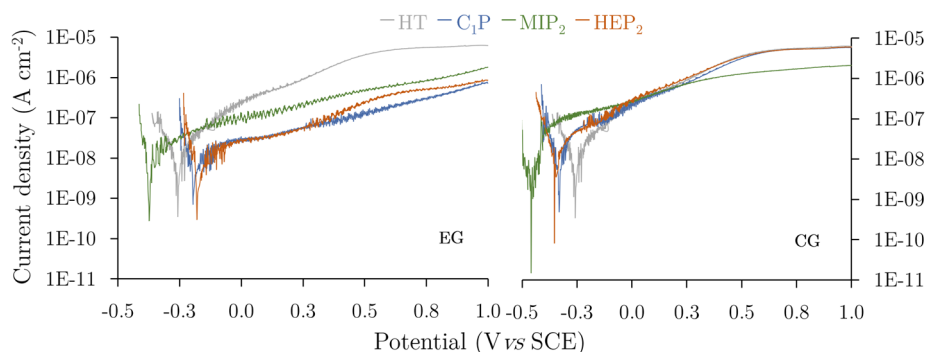


Figure 7.7. Representative polarization curves for HT NiTi, C₁P, MIP₂ and HEP₂ samples in 0.5 M NaCl at a scan rate of 1 mV s⁻¹.

Table 7.2. Values of E_{corr} , j_{corr} , IE and BF for HT NiTi, C₁P, MIP₂ and HEP₂ samples (obtained by LSV and CV).

Sample	E_{corr} vs SCE (mV)	j_{corr} (nA cm ⁻²)	IE (%)	BF (%)
HT	-284 ± 88	103.6 ± 22.2	-	-
C ₁ P (CG)	-392 ± 20	8.5 ± 2.6	91.8 ± 2.1	12.5 ± 3.2
C ₁ P (EG)	-189 ± 10	5.4 ± 1.6	94.8 ± 1.5	97.2 ± 0.5
MIP ₂ (CG)	-463 ± 29	16.6 ± 2.6	83.9 ± 2.5	2.4 ± 0.4
MIP ₂ (EG)	-371 ± 56	6.1 ± 2.4	94.1 ± 2.4	95.9 ± 2.9
HEP ₂ (CG)	-354 ± 11	15.5 ± 2.6	85.1 ± 2.5	4.9 ± 1.1
HEP ₂ (EG)	-182 ± 3	15.3 ± 0.9	94.9 ± 0.9	97.5 ± 0.5

The alteration of the oxide layer within the CH process, which results in particular in an increase of Ni content (Table 7.1), is confirmed by cyclic voltammetry (CV) measurements (Figure 7.8). The first CV cycles obtained for the CH-(C₁P, MIP₂ and HEP₂) show a larger oxidation peak, corresponding to higher oxidation amount of Ti comparatively to HT-NiTi and to the reappearance of Ni²⁺ to Ni³⁺

oxidation peak, which is more detectable in the case of CH-(HEP₂). Higher blocking factor (BF) are obtained for EG up to 98.4 %, resulting from a very low anodic current density and the absence of a nickel oxidation peak. CV, LSV and XPS results confirm the effectiveness of the electro-assisted grafting process (EG) whatever the organophosphonic derivative.

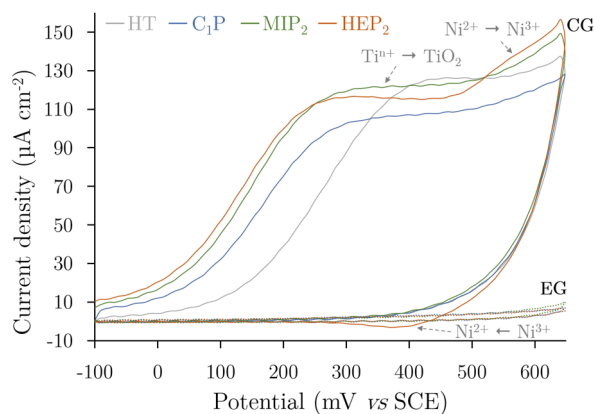


Figure 7.8. Representative first cycle of cyclic voltammograms for HT NiTi, C₁P, MIP₂ and HEP₂ samples in 0.1 M NaOH at a scan rate of 20 mV s⁻¹.

7.4 Transposition to derivatives bearing alkyl chains

7.4.1. Methylphosphonic vs. dodecylphosphonic derivatives

The second part of this chapter is devoted to the study of the electro-assisted grafting of (dodecylimino)dimethylene-bisphosphonic acid (DIP₂) and 1-dodecylphosphonic acid (C₁₂P) on HT-NiTi. These are compared to MIP₂ and C₁P.

First, the water contact angles point out to a decreased hydrophilicity of the surface after its modification by C₁₂P and DIP₂, with respective values of 96.5° ± 0.6° and 74.6° ± 2.2°. These values are higher to that of HT-NiTi (32.0°) and MIP₂ (41.0°) due to the presence of the hydrophobic alkyl chain. Furthermore, DIP₂ appears to be more hydrophylic than C₁₂P, which results from the spacement between the alkyl chains, and the subsequent interdigitation of molecules within the layer (Figure 7.10).

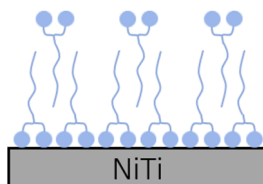


Figure 7.9. Schematic representation of the interdigitation phenomenon.

The grafting efficiency of $C_{12}P$ and DIP_2 is confirmed by XPS. The corresponding P/NiTi ratio (Table 7.3) indicates an increased amount of grafted molecules, with values increasing from 0.05 and 0.14 to respectively 0.11 and 0.25.

Table 7.3. XPS atomic ratios for HT-NiTi and C_1P -NiTi, MIP_2 -NiTi and HEP_2 -NiTi.

Sample	P/NiTi	O/NiTi	Ni/NiTi	Ti/NiTi
HT	-	4.27 ± 0.70	0.15 ± 0.01	0.85 ± 0.01
C_1P	0.05 ± 0.01	3.12 ± 0.21	0.13 ± 0.02	0.87 ± 0.02
MIP_2	0.14 ± 0.02	3.92 ± 0.36	0.15 ± 0.02	0.85 ± 0.02
$C_{12}P$	0.11 ± 0.03	3.14 ± 0.17	0.18 ± 0.04	0.82 ± 0.04
DIP_2	0.25 ± 0.01	3.21 ± 0.09	0.16 ± 0.01	0.84 ± 0.01

The presence of alkyl chain thus further improve the grafting efficiency of both mono- and bisphosphonic anchoring groups. In both cases, the presence of a second anchoring group onto the molecule improves the grafting efficiency and remains of interest. The composition of the surface in O, Ni and Ti is not affected.

This increased amount of grafted molecules seen for $C_{12}P$ and DIP_2 impacts NiTi corrosion resistance, as expressed by the decreased corrosion current densities (Figure 7.10 and Table 7.4).

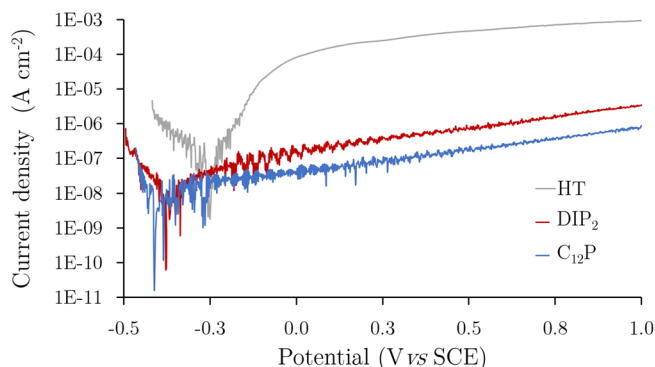


Figure 7.10. Representative polarization curves for HT-NiTi, $C_{12}P$ and DIP_2 in 0.5 M NaCl at a scan rate of 1 mV s^{-1} .

Table 7.4. Values of E_{corr} , j_{corr} and IE for HT-NiTi, C_1P , $C_{12}P$, MIP_2 and DIP_2 .

Sample	E_{corr} vs SCE (mV)	j_{corr} (nA cm^{-2})	IE (%)
HT	-284 ± 88	103.6 ± 22.2	-
C_1P	-189 ± 10	5.4 ± 1.6	94.8 ± 1.5
MIP_2	-371 ± 56	6.1 ± 2.4	94.1 ± 2.4
$C_{12}P$	-415 ± 6	2.4 ± 0.5	96.4 ± 0.1
DIP_2	-388 ± 14	2.2 ± 0.6	96.8 ± 0.2

7.4.2. Repulsion of non-grafted incorporated molecules

To prevent the incorporation of non-grafted molecules within C₁₂P and DIP₂ monolayers, a negative polarization of -0.5 V *vs* SCE is applied for 5 minutes to the NiTi substrate subsequently to the grafting in order to repulse the incorporated molecules. The obtained WCA (Figure 7.11a) confirm the presence of incorporated DIP₂ molecules within the layer, as well as the efficiency of their repulsion with an increased value of 93.3°, typical of aliphatic chains. However, no difference is seen in the case of C₁₂P, as no molecule can be intercalated due to the denser formed layer. These observations are further confirmed by a the XPS P/NiTi ratios, with similar amount a detected molecules of C₁₂P, but lower molecules of DIP₂ after repulsion.

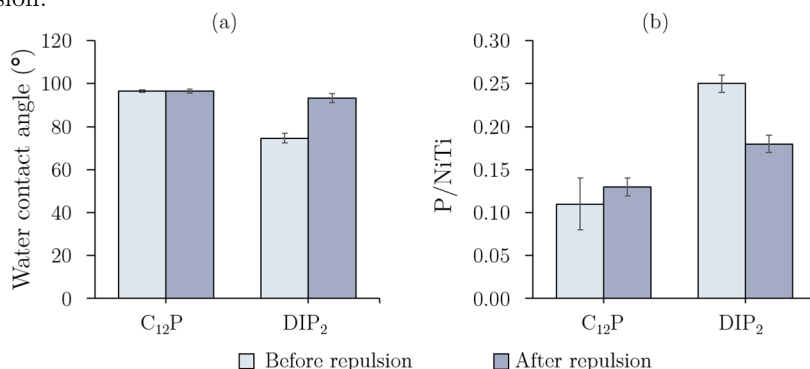


Figure 7.11. Water contact angles (a) and P/NiTi XPS atomic ratio (b) for HT-NiTi, and C₁₂P or DIP₂ (before and after repulsion) in 0.5 M NaCl at a scan rate of 1 mV s⁻¹.

The effect of the molecule repulsion on the corrosion resistance of NiTi is finally studied by LSV (Figure 7.12). Despite it does not affect the behaviour of C₁₂P, the repulsion process improved DIP₂-NiTi corrosion resistance with an inhibition efficiency increasing from 96.8 to 98.3%, which is due to a less hydrophilic behaviour.

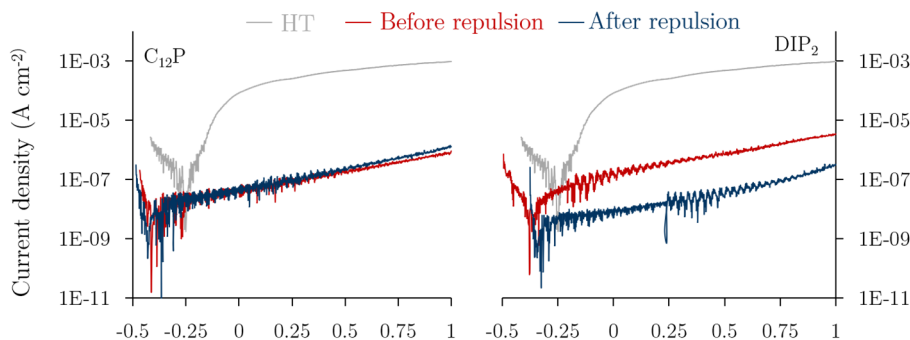


Figure 7.12. Representative polarization curves for HT-NiTi, and C₁₂P or DIP₂ (before and after repulsion) in 0.5 M NaCl at a scan rate of 1 mV s⁻¹.

7.5 Conclusions

Conventional (CH) and electro-assisted (EG) grafting of three organophosphonic derivatives (C_1P , MIP_2 and HEP_2) with one or two anchoring groups have been compared.

The electro-assisted process, achieved in 10 min and at room temperature by anodic polarization of HT-NiTi has shown to impact the oxide layer composition as well as the organophosphonic derivatives grafting reaction.

XPS results obtained for EG (C_1P , MIP_2 and HEP_2) point to a successful surface modification by C_1P , MIP_2 and HEP_2 , as well as a reinforcement of the oxide layer. The use of molecules with larger footprint size increases the grafting rate and leads to the formation of denser layers, thanks to the presence of more partially negative charge on the molecules.

The impact of the nature of the molecule and the grafting process assessed by electrochemical techniques (LSV and CV) confirm the superiority of the EG process over the CH process. It leads to an enhancement of the corrosion resistance and to the formation of a more blocked surface. EG process has two synergetic impacts, the reinforcement of the oxide layer and the high grafting efficiency of the organophosphonic derivatives. By contrast, the conventional grafting (CH) leads to a slight decrease of the corrosion resistance and an increase of Ni surface content.

References

- (1) Arrotin, B.; Delhalle, J.; Dubois, P.; Mespouille, L.; Mekhalif, Z. Electroassisted Functionalization of Nitinol Surface, a Powerful Strategy for Polymer Coating through Controlled Radical Surface Initiation. *Langmuir* **2017**, *33* (12), 2977–2985.
- (2) Socrates, G. *Infrared and Raman Characteristic Group Frequencies: Tables and Charts*, Third Edit.; John Wiley & Sons, 2004.
- (3) Wei, C.; Bard, A. J.; Mirkin, M. V. Scanning Electrochemical Microscopy. 31. Application of SECM to the Study of Charge Transfer Processes at the Liquid/Liquid Interface. *J. Phys. Chem.* **1995**, *99* (43), 16033–16042.
- (4) Cannes, C.; Kanoufi, F.; Bard, A. J. Cyclic Voltammetry and Scanning Electrochemical Microscopy of Ferrocenemethanol at Monolayer and Bilayer-Modified Gold Electrodes. *J. Electroanal. Chem.* **2003**, *547* (1), 83–91.

Chapter 8

General conclusions & perspectives

8.1	General conclusions	117
8.2	Perspectives	119

8.1 General conclusions

This aim of this thesis was to improve the surface properties of Nitinol, a nickel/titanium alloy of great interest for biomedical applications such as cardiovascular stent. Indeed, despite it exhibits outstanding properties, *e.g.* heat, impact and corrosion resistance, high fatigue strength or shape memory, the use of Nitinol is still hampered by nickel inclusions. In this context, the main objectives are, on one hand, to improve Nitinol corrosion resistance (especially in physiological conditions) and on another hand, to ease its biointegration and prevent side reactions such as inflammation. The strategy investigated within this work relied on a multistep surface modification process: (1) the hydrothermal reinforcement of the native oxide layer; (2) the elaboration of a protective initiating monolayer; and (3) the polymerization of 2-methacryloyloxyethyl phosphorylcholine, a biocompatible monomer of huge interest.

The first part of the work (Chapter 3) was dedicated to the study of the impact of a hydrothermal treatment of Nitinol native oxide layer over its corrosion resistance, its composition, its thickness and its stability over time. The results obtained from linear sweep voltammetry, cyclic voltammetry, scanning electrochemical microscopy, and electrochemical impedance spectroscopy pointed out the increased passivity and resistivity of the oxide layer, thus noticeably improving the material resistance. Furthermore, it has been proven by X-ray photoelectron spectroscopy that the composition of Nitinol surface was chemically reinforced in TiO_2 and depleted of Ni after such treatment, which is a further improvement and should decrease the risks of corrosion and prevent from the release of Ni^{2+} . However, even if the hydrothermal treatment of Nitinol has been proven to be beneficial for its corrosion resistance, the implementation of Nitinol in biomedical fields is still controversial and further surface modifications, *e.g.* the elaboration of protective organic coatings, are still required.

Based on that, the second modification step consisted in elaborating an organic coating that could further protect the material from corrosion, at the same time as enable to subsequent surface-initiated polymerization of monomer of biomedical interest, *e.g.* 2-methacryloyloxyethyl phosphorylcholine. For this purpose, the use of phosphonic-made self-assembled monolayers has been considered, and improved. The first attempt of improvement was based on the use of a thermal or an electrochemical assistance for the grafting of 11-(2-bromoisobutyrate)-undecyl-1-phosphonic acid, a phosphonic derivative bearing an ATRP initiating moiety (Chapter 4). Despite both thermal (by conventional and magnetic induction heating) and electrochemical assistance were proven to increase the grafting rate of the molecules as well as an improvement of the surface resistance by using shorter modification

times, it was demonstrated that in the case of sensitive molecules such as BUPA, only the electrografting efficiently preserved the ATRP initiating group, as proven by XPS results and by the efficient subsequent polymerization of 2-(dimethylamino)ethyl methacrylate (DMAEMA), a model monomer. Among all the tested conditions, the best grafting of BUPA was achieved by 5 minutes of electrochemically (EC) assisted self-assembly at RT, making the electrografting a good alternative for fast self-assembly of sensitive molecules such as BUPA.

However, BUPA initiating functions are quite bulky and may lead to disordered and less protective layers. To improve the quality of the monolayer, the use of mixed monolayers resulting from the co-adsorption of two organophosphonic acid derivatives differing in length and/or terminal functional groups has been considered using decylphosphonic acid as a spacer (Chapter 5). Among the tested BUPA/C₁₀P proportions, the use of small amount of BUPA, especially 20%, in the layer has been proven by XPS to improve the grafting efficiency by increasing the amount of grafting molecule and leading to denser layer. The anti-corrosion properties of the material as well as its passivity were also improved, as proven by linear sweep voltammetry, cyclic voltammetry and scanning electrochemical microscopy. Such organic layer was then used to successfully trigger the surface-initiated polymerization of 2-methacryloyloxyethyl phosphorylcholine (MPC). Images obtained by scanning electron microscopy, as well as SECM measurements evidenced the non-uniformity of the PMPC coatings for time lower than 6 h.

To ensure the usability of the so-formed coated Nitinol for cardiovascular applications, its behaviour in human blood plasma body simulated fluid was investigated for different immersion time (Chapter 6). Each modification step was shown to further improve Nitinol corrosion resistance, as the open-circuit potentials keep decreasing step after step. As a consequence, less and less nickel ions are released in the solution as expected. Another key point to validate the modification process is to ensure the ability of human endothelial cells to the surface of the material. For this purpose, a first attempts of EA.hy926 endothelial cells growth was performed on Bare-NiTi, HT-NiTi, BUPA/C₁₀P-NiTi and PMPC-NiTi. However, despite an increased amount of adhering living cells was noticed with time, no significant difference between the different materials was observed so far. Further improvement of the coating is thus mandatory, *e.g.* by modifying the architecture of the polymer coating, as well as by incorporating drugs of interest.

Finally, an alternative to mixed monolayers was investigated by using bisphosphonic acid derivatives (Chapter 7). As a proof of concept, the grafting of short tail mono- and bisphosphonic acid derivatives was performed and compared. In all cases, the corrosion resistance of Nitinol appeared enhanced, with a more

blocking layer. Surprisingly, the higher grafting rate was obtained for the molecule with the largest anchoring group.

8.2 Perspectives

The present thesis set up the basis for new perspectives, in biomedical and cardiovascular fields, but also as a convenient tool for surface modifications of oxidizable metals.

The first required investigation consists in statistically studying the cell growth of endothelial cells over more than 3 samples. Indeed, in the case of cell cultures, the use of triplicates is not enough to obtain statistically reliable results and might hide tendencies.

The most obvious continuity of this work would be to improve the quality of the organic coating and to enable its reendothelialization in human arteries. For this purpose, a first conceivable idea would rely on the elaboration of a more complex polymer and the subsequent intercalation of medical drugs of cardiovascular interest, *e.g.* an immunosuppressive agent to prevent the accumulation of anti-inflammatory cells. The key point would be to enable the time-controlled drug release of such agent directly on the inflamed site, and for a defined time. For this purpose, three kind of polymer coatings could be considered (Figure 8.1). First, a co-monomer, *e.g.* ethylene glycol dimethacrylate, could be used to elaborate a cross-linked coating into which the drug could be intercalated, and progressively released into the inflamed artery after natural degradation of the polymer by the blood plasma (Figure 8.1a). The second possibility relies on the use of a responsive polymer that could deploy themselves and release the drug following an external signal (such as an increase of temperature, or an UV irradiation) (Figure 8.1b). Depending on the medical requirements to cure the patient, a combination of both cross-linked and responsive polymer could be used to enable the differential release of different drugs (Figure 8.1c).

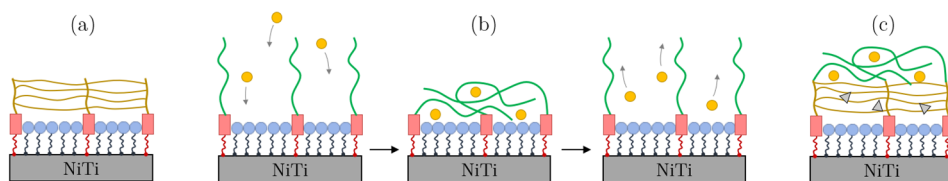


Figure 8.1. Schematic representation of polymer coatings of potential medical interest: (a) crosslinked system, (b) stimuli-responsive polymer, and (c) combination of crosslinked and stimuli-responsive coatings.

A second perspective of this work would be to generate SI-ATRP initiating sites from monolayers made of bisphosphonic derivatives (Figure 8.2a). The use of such layer as an alternative to mixed monolayers should allow a more uniform distribution of the initiating sites on the surface and thus ease the polymerization. It should also be possible to graft a more general molecule, *e.g.* bearing a terminal -OH group, that could be used for a subsequent functionalization with a variety of initiating groups for specific polymerization, thus prevent from the degradation of sensitive molecules during the grafting process (Figure 8.2a).

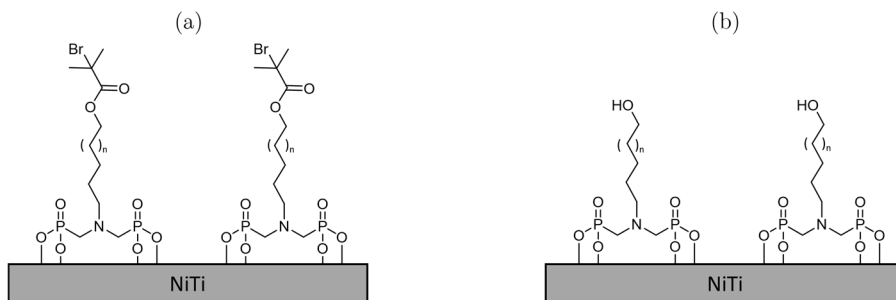


Figure 8.2. Schematic representation of (a) bisphosphonic-made SI-ATRP monolayer and of (b) -OH terminated bisphosphonic monolayer.

A last perspective would be to improve the polymerization process, and decrease the amount of required CuBr catalyst. Indeed, despite it was proven in chapter 4 that no copper was detected in PDMAEMA, CuBr might have affinity with other polymers and its presence in the layer could be detrimental for biomedical applications. For this purpose, the use of electrochemistry could be considered. Indeed, one of the most recent process derived from ATRP rely on the regeneration of the catalyst by electro-assisted reduction of CuBr₂, thus allowing the use of much less catalyst into the polymerization solution.

Appendices

A.1	Substrates and chemicals	123
A.2	Supporting information	124
A.2.1.	Chapter 4.....	124
A.2.2.	Chapter 5.....	126
A.3	An introduction to magnetic induction heating	127
A.3.1.	Principle.....	127
A.3.2.	Skin effect.....	127
A.3.3.	Hysteresis loss.....	128
A.4	Characterization techniques	129
A.4.1.	Water contact angle measurements.....	129
A.4.2.	Scanning electron microscopy.....	130
A.4.3.	Spectroscopic techniques.....	131
A.4.4.	Electrochemical techniques.....	135
A.5	Scientific articles	143
A.5.1.	Published articles.....	143
A.5.2.	In press.....	144
A.5.3.	Unrelated topics.....	144
References	145

A.1 Substrates and chemicals

Table A.1. List of chemicals used for the pre-treatment of Nitinol.

Chemical	Purity (%)
Nitinol (Ni 56%/Ti 44%; 20 x 10 x 0.3 mm ³)	AMF
MetaDi® UltraDiamond Paste (9 µm)	Buehler
MetaDi® Fluid	Buehler
MasterMet™ 2	Buehler
Hydrogen peroxide (35 wt.% in water)	Acros Organics

Table A.2. List of chemicals used for the surface modification of Nitinol.

Chemical	Purity (%)	Provider
1,1,4,7,10,10-Hexamethyltriethylenetetramine	97	Aldrich
11-(2-Bromoisobutyrate)-undecyl-1-phosphonic acid	≥ 97	Sikémia
1-Hydroxyethylidene-1,1-diphosphonic acid	98.5	Acros Organics
2-(Dimethylamino)ethyl methacrylate	98	Aldrich
2-Methacryloyloxyethyl phosphorylcholine	97	Sigma-Aldrich
Copper bromide	99	Aldrich
Decylphosphonic acid	98	abcr
Potassium nitrate	99	Chemlab
(Methylamino)dimethylene-bisphosphonic acid	98	Specific Polymer
Methylphosphonic acid	98	Sigma-Aldrich
Tris[2-(dimethylamino)ethyl]amine	97	Aldrich

Table A.3. List of chemicals used for the analysis solutions.

Chemical	Purity (%)	Provider
Ferrocenemethanol	97	Aldrich
Sodium chloride	≥ 99.5	Fluka
Sodium hydroxide	98.5	Acros Organics

Table A.4. List of the used solvents.

Chemical	Purity (%)	Provider
Diethyl ether	HPLC grade	Lab-Scan
Dried tetrahydrofuran	-	-
Disolol	≥ 99.5	Fluka
Technisolv	99	VWR
Ultra-pure (Milli-Q) water	18.2 mΩ cm	-

Table A.5. List of chemicals used for the preparation of the blood plasma body simulated fluid solution.

Chemical	Purity (%)	Provider
Calcium chloride	96	Acros Organics
HEPES	≥ 99.5	Sigma
Magnesium chloride hexahydrate	99	Acros Organics
Potassium chloride	≥ 99.0	Sigma-Aldrich
Potassium phosphate dibasic	≥ 99	Acros Organics
Sodium bicarbonate	≥ 99	Acros Organics
Sodium carbonate decahydrate	≥ 99	ucb
Sodium sulfate	99	Janssen Chimica

A.2 Supporting information

A.2.1. Chapter 4

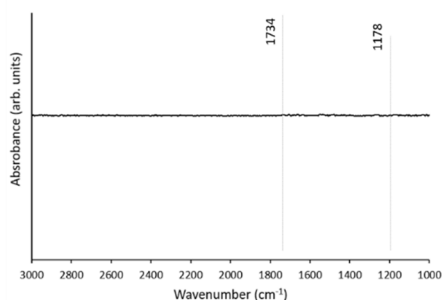


Figure A.1. PM-IRRAS spectrum of NiTi modified by immersion in a solution of 1 mM BUPA in ultrapure milliQ water under conventional heating at 90°C for 1 h.

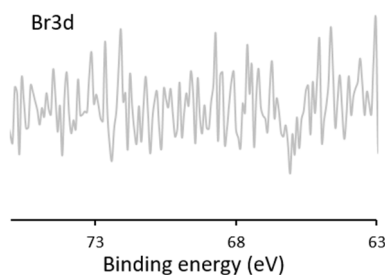


Figure A.2. XPS core spectrum for Br3s component obtained for NiTi modified by immersion in a solution of 1 mM BUPA in ultra-pure milliQ water at room temperature or under conventional heating at 90°C.

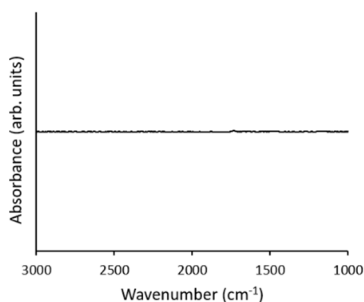


Figure A.3. PM-IRRAS spectrum of hydrothermally treated NiTi modified by SI-ATRP of 1.5 M DMAEMA in solution in THF in presence of 13.9 mM CuBr and 1.39 mM HMTETA for 1 hour at 60°C.

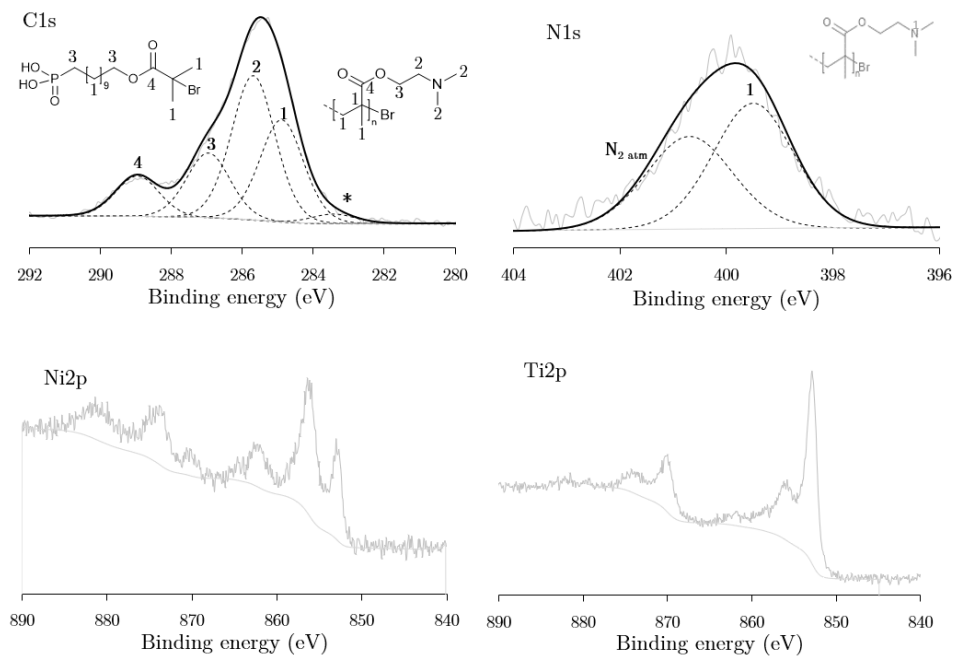


Figure A.4. XPS core spectrum for C1s, N1s, Ni2p and Ti2p obtained for hydrothermally treated NiTi modified by SI-ATRP of 1.5 M DMAEMA in solution in THF in presence of 13.9 mM Cubr and 1.39 mM HMTETA for 1 hour at 60°C.

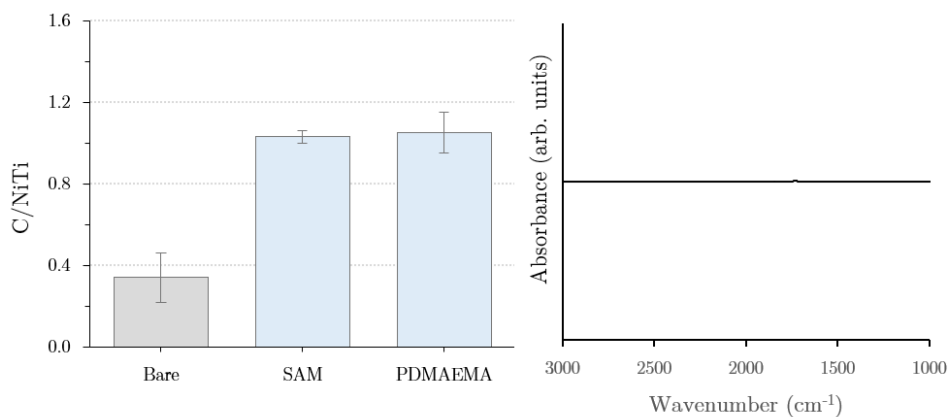


Figure A.5. XPS C/NiTi (A) and PM-IRRAS spectra (B) of BUPA covered NiTi substrates modified by SI-ATRP of 1.5 M DMAEMA in solution in THF in presence of 13.9 mM Cubr and 1.39 mM HMTETA for 1 hour at 60°C

A.2.2. Chapter 5

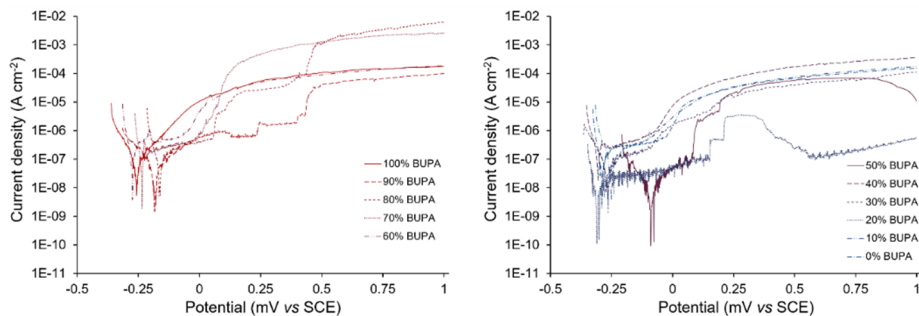


Figure A.6. XPS C/NiTi (A) and PM-IRRAS spectra (B) of BUPA covered NiTi substrates modified by SI-ATRP of 1.5 M DMAEMA in solution in THF in presence of 13.9 mM Cubr and 1.39 mM HMTETA for 1 hour at 60°C

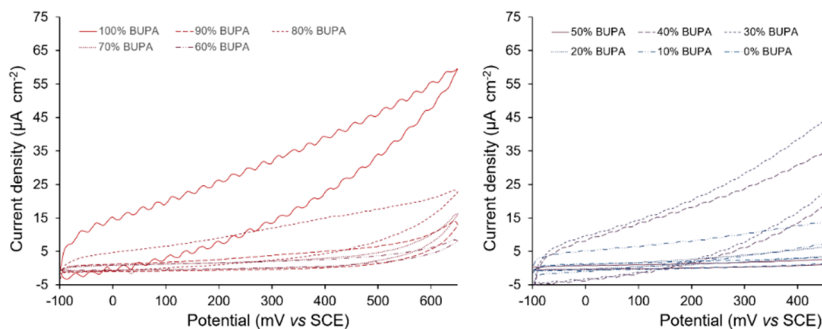


Figure A.7. XPS C/NiTi (A) and PM-IRRAS spectra (B) of BUPA covered NiTi substrates modified by SI-ATRP of 1.5 M DMAEMA in solution in THF in presence of 13.9 mM Cubr and 1.39 mM HMTETA for 1 hour at 60°C

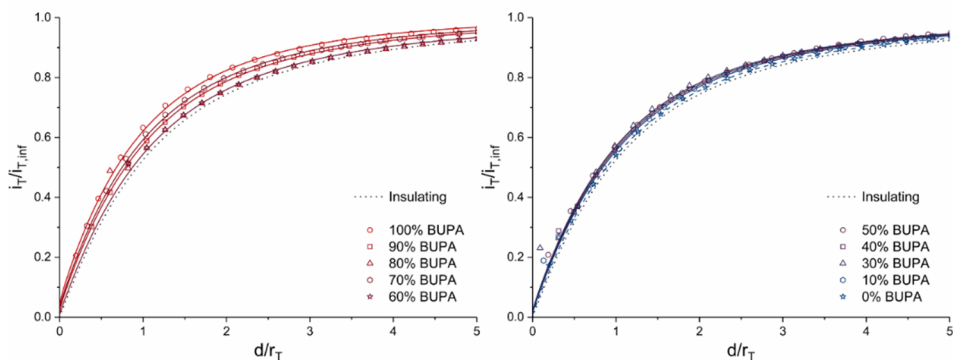


Figure A.8. XPS C/NiTi (A) and PM-IRRAS spectra (B) of BUPA covered NiTi substrates modified by SI-ATRP of 1.5 M DMAEMA in solution in THF in presence of 13.9 mM Cubr and 1.39 mM HMTETA for 1 hour at 60°C

A.3 An introduction to magnetic induction heating

A.3.1. Principle

Magnetic induction heating (MIH) is a process based on electromagnetic induction and used to locally heat electrically conducting materials in presence of a time-variable magnetic field in a direct and contactless way.¹ It is therefore an efficient tool in surface science, where it is used to activate physico-chemicals process at the surface of materials.²⁻⁴

The principle of MIH relies on Faraday’s and Lenz laws of induction that respectively states that: “The induced electromotive force (ε) in a closed circuit is proportional to the time rate of change of the magnetic flux (Φ_B) enclosed by this circuit”, and “The polarity of the induced emf is such that it opposes the cause of its production”. In the case of a N-spires solenoid, the Emf is thus given by the adapted Lenz-Faraday relation (Eq. A.1).

$$\varepsilon = -N \frac{\partial \Phi_B}{\partial t} \tag{Eq. A.1.}$$

The time-variable magnetic field (Figure A.9a) generated from alternative currents (AC) can be used to induce local Eddy currents within electrically conducting materials (Figure A.9b) and trigger their heating by Joule effect (Figure A.9c). The produced energy (W) by those current (I) through the conducting material of electrical resistance (R) during a determined time (t) is given by the relation (Eq. A.2.):

$$W = RI^2t \tag{Eq. A.2.}$$

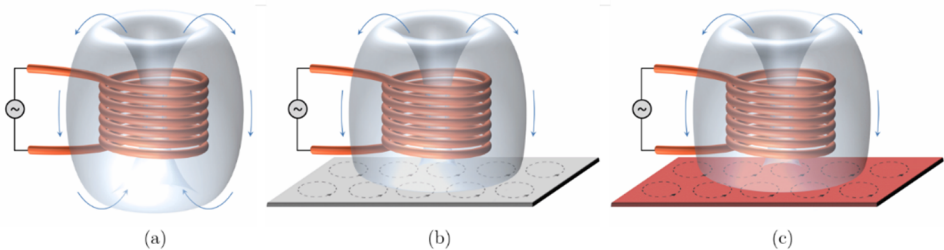


Figure A.9. Schematic representation of magnetic induction heating: generation of a time-variable magnetic field (a), induction of Eddy currents into the metal (b), and heat production by Joule effect (c).

A.3.2. Skin effect

In the case of AC currents, the eddy current density and the resulting heat distribution is not uniform within the material’s cross-section. This results from an

electromagnetic phenomenon called skin effect. According to this, the induced Eddy currents will mainly flow in the surface layer (with about 86 of the induced power).^{1,5} The distribution of the current density (I in A m^{-2}) along the material thickness can be evaluated thanks to its relation with the current density at the surface (I_0 in A m^{-2}), the distance from the surface (y in m) and the penetration depth (δ in m) (Eq. A.3.).¹

$$I = I_0 e^{-y/\delta} \tag{Eq. A.3.}$$

The skin effect is characterized by the penetration depth, defined as the distance below the surface where the current density falls to 37 of its value at the surface (Figure A.10). The corresponding power density is retained at 14 (as power relates to current as RI^2). About 63 of the current and 86 of the induced power is thus concentrated within a surface layer of thickness δ .^{1,5}

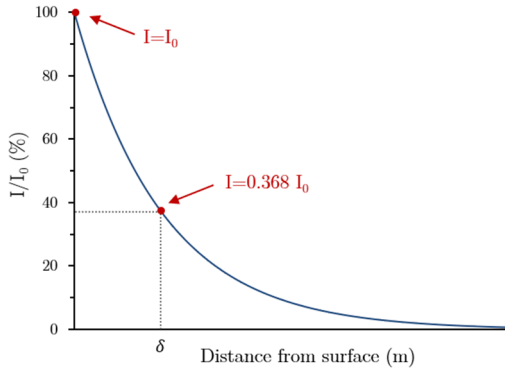


Figure A.10. Current density distribution due to skin effect (adapted from Rudnev *et al.*).^{1,5}

This penetration depth (δ in m) varies according to the electrical resistivity (ρ in $\Omega \text{ m}$), the frequency (f in Hz), and the relative magnetic permeability (μ_r) (Eq. A.4.).^{1,5}

$$\delta = 503 \sqrt{\frac{\rho}{\mu_r f}} \tag{Eq. A.4.}$$

Considering the ρ and μ_r values for Nitinol (respectively $82 \mu\Omega \text{ cm}$ and 1.002),^{6,7} the penetration depth (δ) for Nitinol can be estimated to a value of 1.0 mm .

A.3.3. Hysteresis loss

When a ferromagnetic material (like nickel) is submitted to induction heating, an additional heating mechanism takes place resulting from the existence of magnetic domains, called Weiss domains. When these materials are exposed to the time-

variable magnetic field, they are rapidly magnetized and de-magnetized, thus causing considerable friction and heating inside the material.

Hysteresis loss is thus characterized by the conversion of electromagnetic energy into thermal energy when these domains are rearranged during the hysteresis cycle. For the majority of materials, the heating effect due to hysteresis losses does not typically exceed 9–12% and for through hardening – 6–8% compared to the amount of heat generated by the eddy current (Joule heat).^{1,5}

Note that ferromagnetic materials lose their magnetic properties when heated above the Curie temperature. This temperature (or Curie point) is the temperature at which a ferromagnetic material becomes paramagnetic on heating. Above the Curie point, any further heating of the material must be due to induced eddy current alone.^{1,5}

A.4 Characterization techniques

A.4.1. Water contact angle measurements

The ability of a liquid to spread onto a solid surface, called wettability, can be represented by the contact angle θ defined as the angle between the solid surface and the tangent of the liquid surface (Figure A.11).⁸

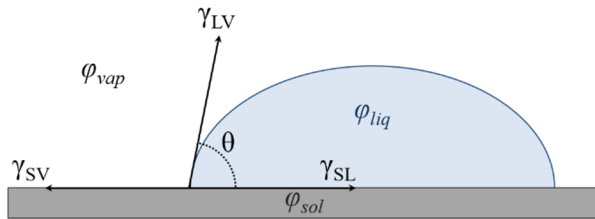


Figure A.11. Schematic representation of the contact angle formed at the equilibrium by a liquid droplet onto the surface of a solid.

Practically, once in contact with the surface, the liquid droplet will spread spontaneously until it reaches its equilibrium configuration (Figure A.11).⁹ The resulting contact angle (θ) is related to the solid/liquid (γ_{SL}), solid/vapor (γ_{SV}) and liquid/vapor (γ_{LV}) interfacial tensions by the Young equation (Eq. A.5).⁸⁻¹⁰

$$\cos \theta = \frac{\gamma_{SV} - \gamma_{SL}}{\gamma_{LV}} \quad (\text{Eq. A.5.})$$

The hydrophilicity or -phobicity of a material can thus be evaluated by the contact angle measurements of a water droplet. Four different cases exist depending on the surface tension:

- | | | | |
|-----|-------------------------------|---------------------------------|--|
| (1) | $\gamma_{sv} \gg \gamma_{sl}$ | $\theta = 0^\circ$ | Perfect wettability: perfectly hydrophilic surface |
| (2) | $\gamma_{sv} > \gamma_{sl}$ | $0^\circ < \theta < 90^\circ$ | Good wettability: hydrophilic |
| (3) | $\gamma_{sv} < \gamma_{sl}$ | $90^\circ < \theta < 180^\circ$ | Poor wettability: hydrophobic surface |
| (4) | $\gamma_{sv} \ll \gamma_{sl}$ | $\theta = 180^\circ$ | No wettability: perfectly hydrophobic surface |

A.4.2. Scanning electron microscopy

Scanning electron microscopy (SEM) is an imaging technique based on the electrons-material interactions widely used to image and analyse the morphology of conducting specimen. In a typical SEM, an electron beam (with an energy typically ranging from 0.1 to 50 keV) is emitted from an electron gun and deflected to scan the sample surface in two dimensions.^{11,12}

The signal collected from the interaction between the primary electron beam and the sample is the results of an electron diffusion inside the material (Figure A.12). This diffusion is due caused by a gradual loss of the electron energy as well as by a lateral spreading resulting from elastic large-angle scattering. Different interaction processes thus exist: the emission of secondary (SE), backscattered (BSE) or Auger (AE) electron, or even the diffusion of X-rays.^{11,13}

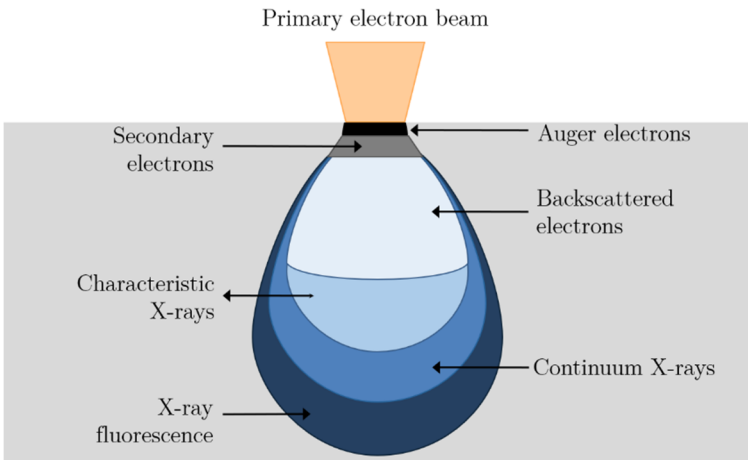


Figure A.12. Schematic representation of the interaction volume of primary electron beam with a surface.¹⁴

In the case of SEM, the most common imaging mode is based on the emission of secondary electrons resulting from inelastic scattering interactions of the electron beam with the valence levels of the constitutive atoms (**Figure A.13**). The SE are known to have a relatively low kinetic energy, they will thus be detected only for

the atoms close to the sample surface, making them sensitive to the surface morphology. Such electrons are used to generate a topographic picture of the observed area.

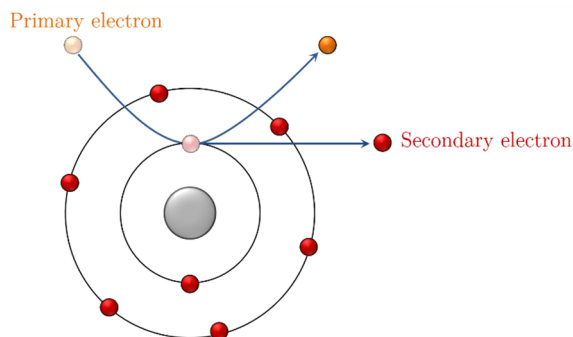


Figure A.13. Schematic representation of the formation of secondary electron.

Practically, a SEM requires different constituents (**Figure A.14**), mainly an electron optical system (consisting of an electron gun, a condenser lens and an objective lens) to produce an electron probe, a scanning coil to scan this electron probe, a sample holder, a secondary-electron detector to collect the emitted secondary electrons, and a display unit with an operative system.^{12,13}

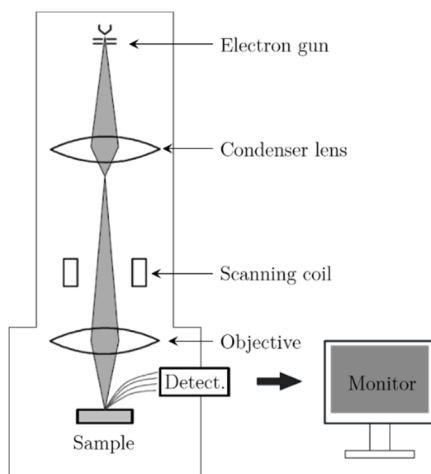


Figure A.14. Schematic representation of a scanning electron microscope.¹²

A.4.3. Spectroscopic techniques

A.4.3.1. X-ray photoelectron spectroscopy

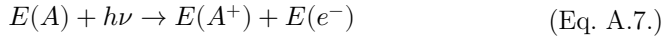
X-ray photoelectron spectroscopy (XPS), also known as electron spectroscopy for chemical analysis (ESCA) is a spectroscopic technique based on the photoionization phenomenon widely used to investigate the surface composition of a material

by providing quantitative and chemical state information. Once the material is irradiated with a monochromatic X-ray beam, photons X can induce the ejection of an electron (called photoelectron) from an atom (Eq. A.6.).^{15,16}



where h is Planck constant ($6.62 \cdot 10^{-34}$ J s) and ν is frequency of the radiation (Hz).

The principle of photoelectrons excitation/emission follows the conservation of energy principle (Eq. A.7.).¹⁶



The difference in energy between the ionized and neutral forms of the atom A corresponds to the binding energy (E_b), whereas the electron's energy is present solely as kinetic energy (E_k) (Eq. A.8.).¹⁶



where Φ is the work function of the spectrometer (*i.e.* the energy required to remove an electron from a solid).

By measuring the E_k of the emitted electrons, it is possible to determine the E_b of a core level photoelectron which gives information about the elements presents at the material's surface, their chemical states, and their chemical environment.¹⁶

After the emission of a photoelectron, the emitting atom is in an excited state. Two relaxation phenomena can then occur: the emission of an Auger electron (Figure A.15b) or the emission of X-rays (fluorescence - Figure A.15b).

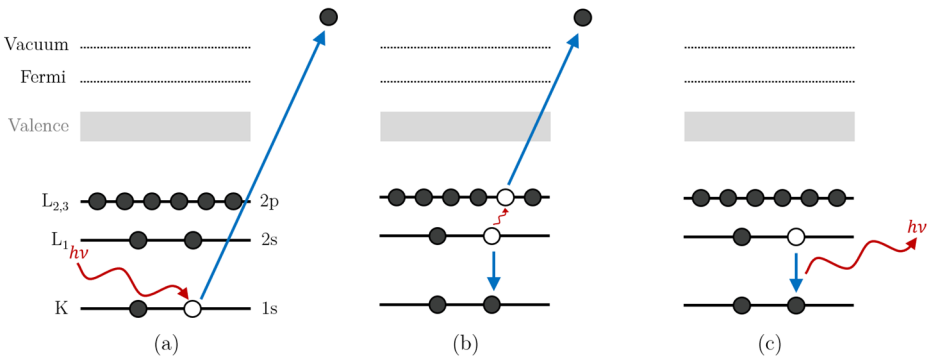


Figure A.15. Schematic representation of the photoionization process (a), the emission of Auger electron (b) or the emission of X-rays (c)(based on Watts et al.¹⁷).

In addition to the chemical information about the atoms present at the surface of a material, XPS can also provide quantitative information. The intensity of a photoelectron peak is indeed related to the number of atoms detected at the surface (N in cm^{-3}), the ionization cross-section of the element (σ), the mean free path of the photoelectron (λ), the analysed area (A), the transmission function of the analyser (T) and all the instrumental factors (K) (Eq. A.9.). The product $K\sigma\lambda AT$ corresponds to a sensitivity factor (called Scofield factor – S) specific for the different orbitals of each element, thus allowing the normalization of the measured intensities.

$$I = KN\sigma\lambda AT = SN \quad (\text{Eq. A.9.})$$

Due to the high specificity of the Scofield factor regarding the sample and the equipment, the quantification of the elements is commonly done using atomic ratios (Eq. A.10.).

$$\frac{I_A}{I_B} = \frac{S_A N_A}{S_B N_B} \quad (\text{Eq. A.10.})$$

Figure A.16 schematically depicts the K-Alpha X-ray photoelectron spectrometer system from ThermoFisher Scientific. The X-rays are produced from an aluminium anode. A quartz monochromator only allows the Al $K\alpha$ line at 1486.6 eV. The emitted photoelectrons are collected by a hemispherical analyser measuring their kinetic energy at a take-off angle of 0° with respect to the normal surface.

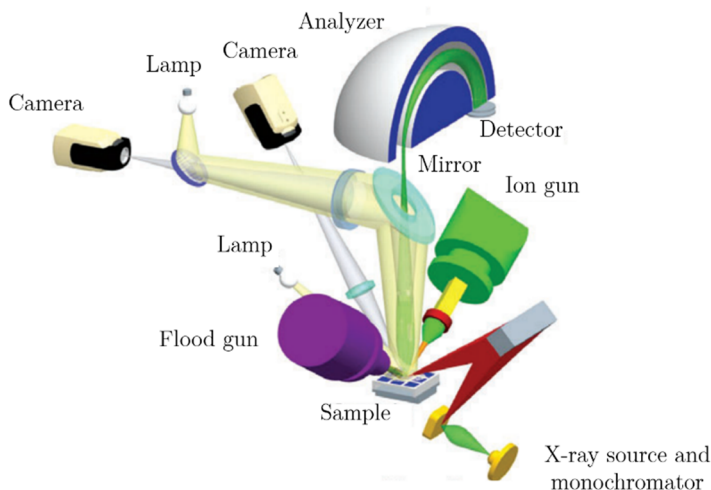


Figure A.16. Schematic representation of a K-Alpha XPS spectrometer.¹⁸

A.4.3.2. Polarization modulation-infrared reflection-adsorption spectroscopy

Fourier-transform infrared spectroscopy (FTIR) is widely used for studies of chemical composition of functional organic films exploiting the fact that molecules absorb the IR radiations at frequencies that are specific to the internal molecular vibrations of their chemical groups. Besides the conventional FTIR, specific surface-sensitive methods, such as polarization modulation infrared reflection absorption spectroscopy (PM-IRRAS), can provide high sensitivity for a small amount of organic molecules at metal surfaces.¹⁹

PM-IRRAS presents a high sensitivity with regard to the detection of surface species on metals. This is due to a fast modulation of the incident beam (Figure A.17a) between a perpendicular (p - Figure A.17b) and a parallel (s - Figure A.17c) polarizations with respect to the surface.

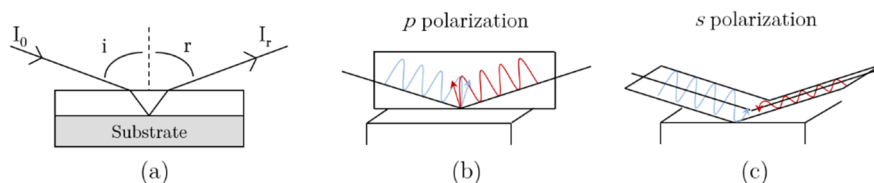


Figure A.17. Schematic representation of IRRAS (a) and of p (b) and s (c) polarized light.²⁰

Practically, the electromagnetic field of the incident IR beam interacts with the oscillating dipoles associated with the vibrational modes of the adsorbed molecules. Those dipoles can be decomposed into parallel ($\vec{\mu}_{//}$) and perpendicular ($\vec{\mu}_{\perp}$) dipoles.

The electrical fields associated to those dipoles induce the appearance of image dipoles into the metallic surface. If the metal is illuminated at grazing angle with p-polarized light, $\vec{\mu}_{\perp}$ is enhanced (Figure A.18a). Conversely, upon illumination with s-polarized light, $\vec{\mu}_{//}$ nearly is compensated and nearly vanishes at the surface (Figure A.18b).^{21,22}

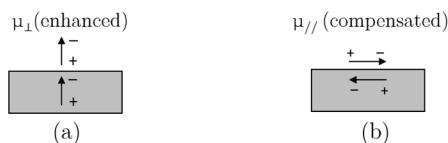


Figure A.18. Schematic representation of the reinforcement of perpendicular dipoles (a) and the compensation of parallel dipoles (b) by image dipoles.

The reflectivity of s-polarized light (R_s) is thus insensitive to the presence of an organic film and can be used to obtain the background spectrum, while the reflectivity of p-polarized light (R_p) is sensitive to molecules present at the surface

and can be used to obtain the spectrum of the film.²² The differential surface reflectivity is thus evaluated by normalized difference between R_p and R_s (Eq. A.11.).^{22,23}

$$\frac{\Delta R}{R} = \frac{2|R_p - R_s|}{(R_p + R_s)} \quad (\text{Eq. A.11.})$$

The obtained response does not contain any signal to absorption of atmospheric CO_2 and H_2O and only the surface species is detected.

A.4.4. Electrochemical techniques

Different electrochemical techniques can be used to characterize metallic materials: cyclic (CV) and linear sweep (LSV) voltammetry, electrochemical impedance spectroscopy (EIS) or scanning electrochemical microscopy (SECM). All electrochemical experiments (except SECM for which the equipment is presented in section A.4.4.4) are carried out using a three-electrode cell with a controlled-analysis spot surface (0.28 cm^2) on the sample (Figure A.19). NiTi substrates are used as the working electrode (WE), a platinum foil as the counter electrode (CE) and a saturated calomel electrode (SCE) as reference electrode (RE) with a potential $E=0.2412 \text{ V}$ vs standard hydrogen electrode (SHE).²⁴

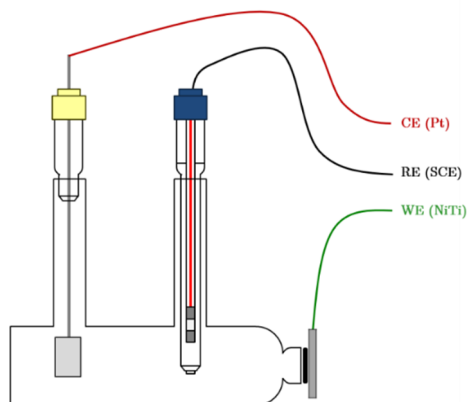


Figure A.19. Schematic representation of the electrochemical system used for the measurements.

A.4.4.1. Cyclic voltammetry

Cyclic voltammetry (CV) is a potentiodynamic technique implying a linear and alternate variation of the working electrode potential between an initial (E_i) and a final (E_f) potentials while the current response is measured (Figure A.20a). This

method is widespread nowadays and can be used for the study of reactional mechanisms as well as for quantitative measurements.^{25,26}

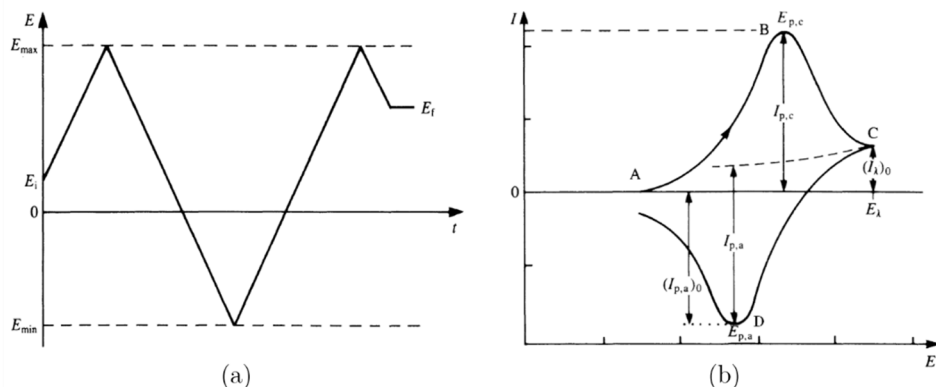


Figure A.20. Schematic representations of the linear potential scan used for cyclic voltammetry (a) and of a typical voltammogram (b) (E_i = initial potential, E_f = final potential, E_{\max} = maximal potential and E_{\min} = minimal potential).²⁷

The corresponding voltammogram (Figure A.20b) is characterized by currents/potentials of at least one oxidation peak ($E_{p,a}$) during the anodic scan, and the corresponding reduction peak(s) ($E_{p,c}$) during the cathodic scan. The intensity of those peaks (i_p) is related to the electrode surface (A in cm^2), the number of exchanged electrons (n), the diffusion coefficient (D in $\text{cm}^2 \text{s}^{-1}$), the scan speed (v in V s^{-1}) and the concentration (C in M) by Randles-Sevcik relation (Eq. A.12).²⁵

$$i_p = 2.69 \cdot 10^5 \cdot A \cdot n^{3/2} \cdot D^{1/2} \cdot v^{1/2} \cdot C \quad (\text{Eq. A.12.})$$

The diffusion coefficient is defined following Fick law as the proportional relation between the flux of a specie (J in $\text{mol cm}^{-2} \text{s}^{-1}$) and the gradient of its concentration (mol) (Eq. A.13).²⁵

$$J_i(x, t) = -D \left(\frac{\partial C_i(x, t)}{\partial x} \right)_x \quad (\text{Eq. A.13.})$$

A.4.4.2. Linear sweep voltammetry

Linear sweep voltammetry (LSV – also known as polarization curves measurements), used to assess the corrosion resistance of an electrode, is based on the linear scanning of a range of potentials (from the cathodic to the anodic domain) and the measurement of the current response. Generally, electrochemical reactions taking place at an electrode surface can be limited by charge transfer (electron transfer at the surface) or mass transfer (diffusion of the reactants and products). These two

parameters thus play an important role in the kinetics of electrochemical reactions at the surface of an electrode. However, the mass transfer limitation can be considered as negligible if a very low potential scan rate is used.^{25,28}

In this particular case, the relation between the current density (i) and the overpotential (η) (The Butler-Volmer describes the relation between the overpotential (η) (*i.e.* the difference between the applied potential E and the reversible potential E_{rev}) is described by the Butler-Volmer relation (Eq. A.14).^{25,28,29}

$$i = i_a + i_c = i_0 e^{\frac{\alpha n F}{RT} \eta} - i_0 e^{\frac{-(1-\alpha) n F}{RT} \eta} \quad (\text{Eq. A.14.})$$

where i_a , i_c and i_0 are respectively the anodic, cathodic and exchange (representative of the charge transfer at the equilibrium) current densities, α the charge transfer coefficient, n the number of electron implied in the reaction, T the temperature, and F and R respectively the Faraday (96 485,3 C mol⁻¹) and the ideal gas (8,314 J K⁻¹ mol⁻¹) constants.

Considering the anodic (β_a)(Eq. A.15.) and (β_c)(Eq. A.16.) cathodic Tafel coefficients:²⁹

$$\beta_a = \frac{RT}{\alpha n F} \quad (\text{Eq. A.15.})$$

$$\beta_c = \frac{RT}{(1 - \alpha) n F} \quad (\text{Eq. A.16.})$$

Butler-Volmer equation can be simplified (Eq. A.17.).²⁹

$$i = i_0 e^{\frac{\eta}{\beta_a}} - i_0 e^{-\frac{\eta}{\beta_c}} \quad (\text{Eq. A.17.})$$

When the overpotential is high enough, the kinetics of one of the two reactions becomes negligible with respect to the other and a linear relationship exists between the current density logarithm and the overpotential. By successively neglecting the cathodic and anodic reactions, the expression of the anodic (Eq. A.18.) and cathodic (Eq. A.19.) Tafel lines are respectively obtained if $\eta/\beta_a \gg 1$ or if $\eta/\beta_c \ll 1$.^{25,28,29}

$$\log i_a = \frac{\eta - a_a}{b_a} \quad (\text{Eq. A.18.})$$

$$\log i_c = \frac{\eta - a_c}{b_c} \quad (\text{Eq. A.19.})$$

where the parameters a and b are the Tafel constants. The value of E_{rev} , which is related to η (Eq. A.20.), and the associated current density can be determined at the intersection of those Tafel lines (Figure A.21a). However, in the case of mixed electrode (*i.e.* a system in which two different oxidation/reduction reactions occur), E_{rev} corresponds to the corrosion potential (E_{corr}), defined as the potential spontaneously reached by the electrode without any external current.²⁹

$$\eta = E - E_{rev} \quad (\text{Eq. A.20.})$$

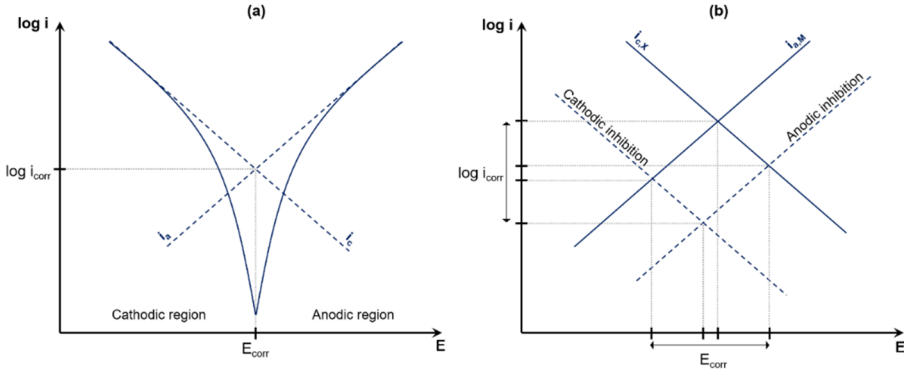


Figure A.21. Schematic representation of the current density variation as function of the overpotential and the corresponding Tafel lines (a) and of Evans diagram for a corrosion reaction (b).

A variation of the potential with respect to E_{corr} , called polarization (ζ) leads to an anodic current if it is positive, or to a cathodic current if it is negative. Therefore, for a corrosion reaction involving an anodic ($M \rightarrow M^{n+} + ne^-$) and a cathodic ($X^{n+} + ne^- \rightarrow X$) reactions, the current density corresponds to the sum of the partial current densities (Eq. A.21.).²⁹

$$i = i_{aM} + i_{cM} + i_{aX} + i_{cX} \quad (\text{Eq. A.21.})$$

At potentials close to E_{corr} , i_{cM} and i_{aX} are negligible (Eq. A.22.).²⁹

$$i = i_{aM} + i_{cX} \quad (\text{Eq. A.22.})$$

The Evans diagram (Figure A.21b) represents the partial anodic and cathodic current densities of each reaction. This representation can be used to assess the inhibiting properties resulting from a surface modification (physical treatment, coating, *etc.*). Three kinds of inhibition are possible (Figure A.21b): a cathodic inhibition resulting from a decrease of i_{corr} and a cathodic shift of E_{corr} , an anodic

inhibition resulting from a decrease of i_{corr} and an anodic shift of E_{corr} , and a mixed inhibition resulting from a strong decrease of i_{corr} and a small shift of E_{corr} .

Generally, polarization curves can be divided into different distinct stages (Figure A.22). In the cathodic range, the measured current densities result from the reduction of H^+ or M^{n+} ions and the metal is immune to corrosion. Its active dissolution starts in the anodic range, at $E > E_{corr}$ until the passivation potential (E_{pass}) is reached. At this stage, the current densities decrease by several order due to the metal passivation (Figure A.22 – 2). As a comparison, the behaviour of a non-passive metal is presented in dashed-dotted line (Figure A.22 – 1). Beyond the pre-passive (PP) transition and under specific conditions (*e.g.* presence of corrosive anions, acidic conditions, *etc.*), metastable (Figure A.22 – 3) or stable (Figure A.22 – 4) pitting phenomena characterized by an increased current density can occur at the pitting potential (E_{pit}). Such pitting may occasionally be followed by a second metal passivation (Figure A.22 – 5). The potential will then finally evolve in the transpassive range ($E > E_{O_2}$)(Figure A.22 – 6), characterized by a rupture of the passive layer, the dissolution of metal ions and the oxidation of H_2O in O_2 , thus leading to an increase of the current density.³⁰

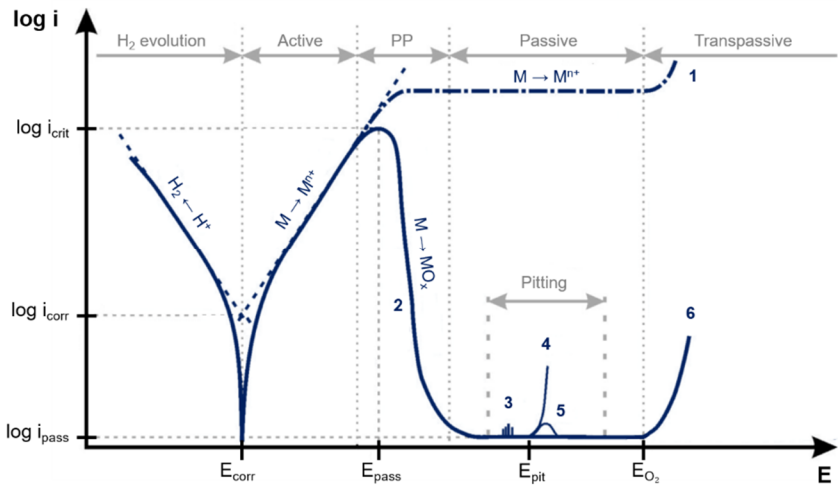


Figure A.22. Schematic representation of a typical polarisation curve for a metallic substrate (adapted from Albu³⁰).

A.4.4.3. Electrochemical impedance spectroscopy

Electrochemical impedance spectroscopy (EIS) is an electroanalytic technique using a sine wave excitation function of the electrode potential over variable frequencies. If we consider the current response for small potential perturbations as

linear, a sinusoidal variation of the electrode potential (Eq. A.23.) around a constant potential (E_0) with a small amplitude will generate a sinusoidal current response with the same frequency, but with a possible dephasing with respect to the potential (Eq. A.24.).

$$E(t) = E_0 + \Delta E \sin(\omega t) \quad (\text{Eq. A.23.})$$

$$I(t) = I_0 + \Delta I \sin(\omega t + \phi) \quad (\text{Eq. A.24.})$$

where ω is the pulsation (linked to the frequency f following $\omega = 2\pi f$ and ϕ is the phase angle between the two signals. In the case of an electrochemical system, the transfer function from $E(\omega)$ to $I(\omega)$ is called the admittance of the system (Y)(Eq. A.25.).

$$Y(\omega) = \frac{I(t)}{E(t)} = |Y(\omega)|e^{j\phi} \quad (\text{Eq. A.25.})$$

In the same way, the transfer function from $I(\omega)$ to $E(\omega)$ is called impedance of the system (Z), also known as the inverse of the admittance (Eq. A.26.).

$$Z(\omega) = \frac{1}{Y(\omega)} = \frac{E(t)}{I(t)} = |Z(\omega)|e^{j\phi} \quad (\text{Eq. A.26.})$$

where $|Z(\omega)|$ is the impedance modulus.

The transfer function in the frequency domain being a complex number, $Z(\omega)$ can be expressed considering its real ($Z_{re}(\omega)$) and an imaginary ($jZ_{im}(\omega)$) parts (Eq. A.27.).

$$Z(\omega) = Z_{re}(\omega) - jZ_{im}(\omega) \quad (\text{Eq. A.27.})$$

$Z(\omega)$ can be graphically presented in two ways known as Bode (Figure A.23a) or Nyquist (Figure A.23b) diagrams.

The key step in electrochemical impedance experiments is the construction of an equivalent circuit that mimics the electrical behaviour of the system. It is indeed necessary to consider the different elements associated to an electrochemical measurement at the electrode/electrolyte interface:^{25,29,31} (1) the internal **electrolyte resistance** (R_{el}) between the electrodes; (2) the differential **double layer capacitance** (C_{dl}) corresponding to the adjustment of the ionic atmosphere until the charge balance between the electrode surface and the solution is reached; (3) the **charge**

transfer resistance (R_{ct}) due to the electron transfer process; and (4) the **Warburg impedance** (W) due to the mass transfer process (not always present).

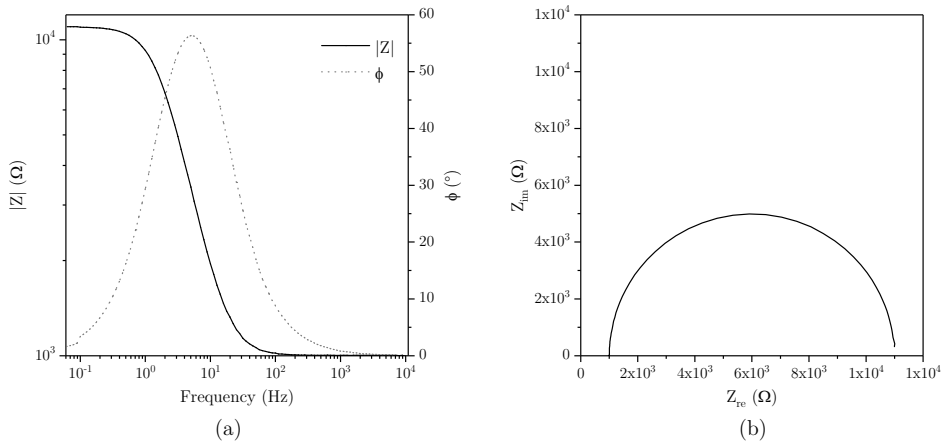


Figure A.23. Schematic representation of Bode (a) and Nyquist (b) plots.

The simplest electrical equivalent circuit resulting from those elements is called Randles circuit (Figure A.24).^{25,29,32} However, in most cases, different elements can be added to this circuit to mimic more complex electrochemical phenomena.

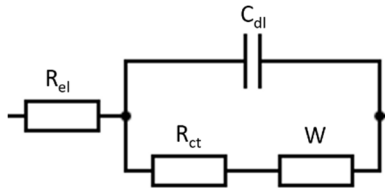


Figure A.24. Randles equivalent circuit.

A.4.4.4. Scanning electrochemical microscopy

Scanning electrochemical microscopy (SECM) is a scanning probe technique used to obtain three-dimensional images of surfaces by scanning an ultramicroelectrode (UME) tip across the substrate. UMEs are characterized by dimensions smaller than 30 μm and can present various geometries, the most common being a disk-shaped electrode obtained by sealing a conductive wire of radius r in a glass capillary of radius R (Figure A.25a). The advantage of UME is the formation of a hemispherical diffusion field that improves mass-transport rate and reduces the ohmic loss, leading to a steady-state diffusion-limited faradaic current ($i_{T,\infty}$ - Figure A.25b) that depends on the concentration (C) of the electrochemical species, its diffusion coefficient (D in cm^2/s), the number of exchanged electrons (n), the Faraday constant (F) and the UME tip radius (r_T) (Eq. A.28).³³⁻³⁵

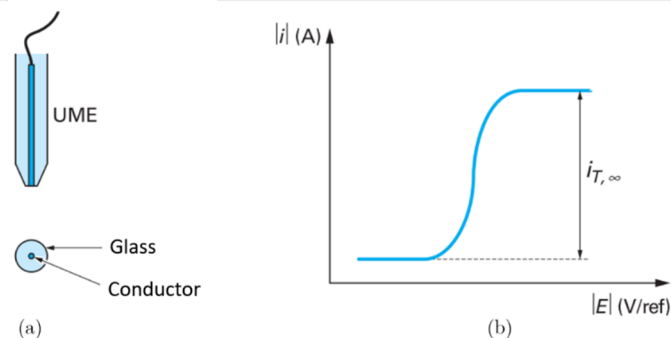


Figure A.25. Schematic representation of an ultramicroelectrode (a) and general shape of a typical corresponding voltammogram.³⁶

$$i_{T,\infty} = 4nFDCr_T \quad (\text{Eq. A.28.})$$

SECM experiments can be carried out in feedback (FB) or in generation collection (GC) mode. For measurements in FB mode, a redox couple is added to the supporting electrolyte as a mediator. If this mediator is added in its reduced form (R) the UME can be used to follow its diffusion-controlled conversion into its oxidized form (O). In the bulk solution (Figure A.26a), the flux of R at the tip surface is constant and lead to a steady-state current. When the tip is brought close to an insulating substrate (Figure A.26b), the diffusion of R towards the UME is hindered and i_T decreases (Figure A.27). This phenomenon is called “negative feedback”. However, when the tip is moved towards a conductive substrate (Figure A.26c), R can be regenerated by both electrochemical conversion and by diffusion of new species, thus increasing i_T (Figure A.27).^{33,35,36}

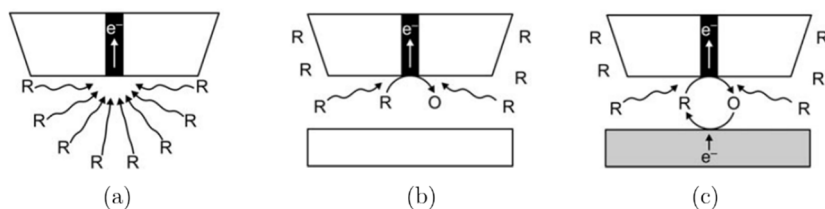


Figure A.26. Principle of the feedback mode: in the bulk solution (a), hindered diffusion when the UME approaches an insulating substrate (b), and mediator regeneration when the UME approaches a conductive sample.³⁵

A SECM consists of a positioning system (including the positioning elements, translation stages, and motor controllers) that moves an UME with respect to the sample (**Figure A.28**). The UME, used as a local probe, is connected to a bipotentiostat and the electrochemical cell is completed by a reference (Ag/AgCl ; $E = +0.222 \text{ V vs ENH}^{24}$) and a counter electrode. Depending on the analysis (especially

in GC mode), the sample can also be connected to the bipotentiostat as a second working electrode.

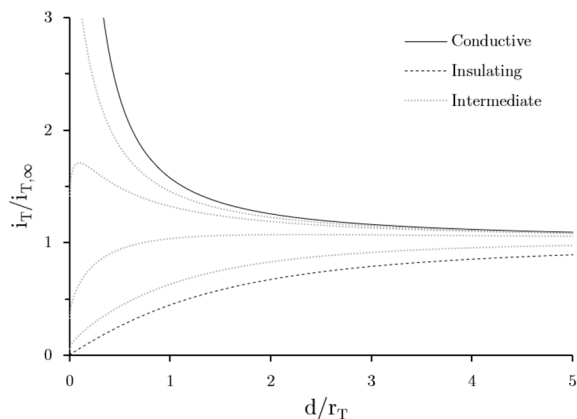


Figure A.27. Examples of approach curves obtained in feedback mode for a conductive, an insulating and intermediates samples. (adapted from Wittstock *et al.*³⁵).

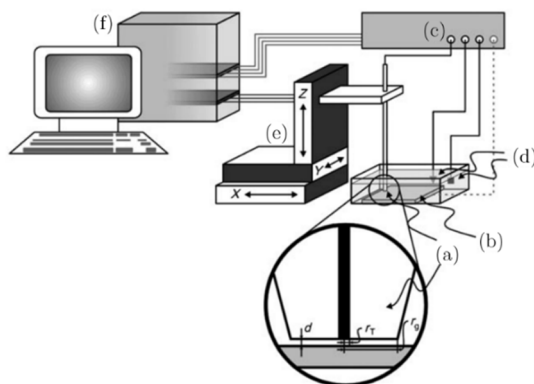


Figure A.28. Components of a SECM: disk-shaped ultramicroelectrode (a), sample (b), bipotentiostat (c), reference and counter electrodes (d), positioning system (e), and informatic control (f).³⁵

A.5 Scientific articles

A.5.1. Published articles

- Arrotin, B.; Delhalle, J.; Mespouille, L.; Mekhalif, Z. Electroassisted Functionalization of Nitinol Surface, a Powerful Strategy for Polymer Coating through Controlled Radical Surface Initiation. *Langmuir* **2017**, *33* (12), 2977–2985

A.5.2. In press

- Arrotin, B.; Noël, J.-M.; Delhalle, J.; Mespouille, L.; Mekhalif, Z. Electrografting of organophosphonic mixed monolayer for SI-ATRP of 2-methacryloyloxyethyl phosphorylcholine. Submitted in *Journal of Coatings Technology and Research*
- Arrotin, B.; Libiouille, C.; Mespouille, L.; Delhalle, J.; Mekhalif, Z. A comparative study of the electro-assisted grafting of mono- and bisphosphonic acids on Nitinol. Submitted in *Protection of Metals and Physical Chemistry of Surfaces*

A.5.3. Unrelated topics

- Arrotin, B.; Jacques, A.; Devillers, S.; Delhalle, J.; Mekhalif, Z. Induction Heating to Trigger the Nickel Surface Modification by in Situ Generated 4-Carboxybenzene Diazonium. *Appl. Surf. Sci.* **2016**, *370*, 320–327.

References

- (1) Rudnev, V.; Loveless, D.; Cook, R.; Black, M. *Handbook of Induction Heating*; Marcel Dek.; Marinescu, I., Geoffrey, B., Eds.; CRC Press: New York, 2002.
- (2) Devillers, S.; Barthélémy, B.; Delhalle, J.; Mekhalif, Z. Induction Heating Vs Conventional Heating for the Hydrothermal Treatment of Nitinol and Its Subsequent 2-(Methacryloyloxy)ethyl 2-(Trimethylammonio)ethyl Phosphate Coating by Surface-Initiated Atom Transfer Radical Polymerization. *ACS Appl. Mater. Interfaces* **2011**, *3* (10), 4059–4066.
- (3) Devillers, S.; Lanners, L.; Delhalle, J.; Mekhalif, Z. Grafting of Bifunctional Phosphonic and Carboxylic Acids on Phynox: Impact of Induction Heating. *Appl. Surf. Sci.* **2011**, *257* (14), 6152–6162.
- (4) Devillers, S.; Lemineur, Q.; Delhalle, J.; Mekhalif, Z. Induction vs . Conventional Heating: Impact on the Morphology and Crystallinity of Copper Electrodeposits on Nickel. *J. Electrochem. Soc.* **2011**, *158* (11), E111–E118.
- (5) Rudnev, V. I.; Loveless, D. *Induction Hardening: Technology, Process Design, and Computer Modeling*; Elsevier, 2014; Vol. 12.
- (6) Nitinol Devices & Components (ndc). *Material Data Sheet Superelastic Nitinol Alloys **; Fremont, 2016.
- (7) Thompson, S. A. An Overview of Nickel-Titanium Alloys Used in Dentistry. *Int. Endod. J.* **2000**, *33* (4), 297–310.
- (8) Tsujii, K. *Wetting and Surface Characterization*; Elsevier Inc., 2017.
- (9) Chen, L.; Bonaccorso, E.; Gambaryan-Roisman, T.; Starov, V.; Koursari, N.; Zhao, Y. Static and Dynamic Wetting of Soft Substrates. *Curr. Opin. Colloid Interface Sci.* **2018**, *36*, 46–57.
- (10) Atkins, P.; De Paula, J. *Physical Chemistry*, 8th Ed.; Oxford University Press: UK, 2006.
- (11) Reimer, L. *Scanning Electron Microscopy: Physics of Image Formation and Microanalysis*, 2nd Ed.; Springer, 1998.
- (12) Jeol Ltd. *Scanning Electron Microscope A To Z*; 2012.
- (13) Lawes, G. *Scanning Electron Microscopy and X-Ray Microanalysis*; Wiley, 1987.
- (14) Vivegnis, S. Électrodéposition D'aluminium Sur Aciers Inoxydable et Carbone En Milieu Liquide Ionique (Master Thesis), University of Namur, 2016.
- (15) *Handbook of X-Ray Photoelectron Spectroscopy*; Chastain, J., Ed.; Perkin Elmer Corporation: USA, 1992.
- (16) Aziz, M.; Ismail, A. F. *X-Ray Photoelectron Spectroscopy (XPS)*; Elsevier

- B.V., 2017.
- (17) Watts, J. F.; Wolstenholme, J. Electron Spectroscopy: Some Basic Concepts. In *An Introduction to Surface Analysis by XPS and AES*; Wiley, 2005; pp 1–15.
- (18) *K-Alpha: A New Concept in XPS*; Thermo Fisher Scientific Inc., 2008.
- (19) Roodenko, K.; Aureau, D.; Yang, F.; Thissen, P.; Rappich, J. Characterization of Thin Organic Films with Surface-Sensitive FTIR Spectroscopy. In *Ellipsometry of Functional Organic Surfaces and Films*; Springer International Publishing, 2014; Vol. 52, pp 305–324.
- (20) Fonder, G. Greffage de Nanofilms Organiques Sur Le Cuivre (Thèse), FUNDP, 2010.
- (21) Moskovits, M. Surface Selection Rules. *J. Chem. Phys.* **1982**, 77 (9), 4408–4416.
- (22) Kycia, A. H.; Su, Z. F.; Brosseau, C. L.; Lipkowski, J. In Situ PM-IRRAS Studies of Biomimetic Membranes Supported at Gold Electrode Surfaces. *Vib. Spectrosc. Electrified Interfaces* **2013**, 345–417.
- (23) Zamlynny, V.; Lipkowski, J. Quantitative SNIFTIRS and PM IRRAS of Organic Molecules at Electrode Surfaces. In *Advances in Electrochemical Science and Engineering*; 2006; Vol. 9, pp 315–376.
- (24) Haynes, W. M.; Lide, D. R.; Bruno, T. J. *CRC Handbook of Chemistry and Physics: A Ready-Reference Book of Chemical and Physical Data.*; 2016.
- (25) Miomandre, F.; Sadki, S.; Audebert, P.; Méallet-Renaut, R. *Électrochimie: Des Concepts Aux Applications*, 3rd Ed.; Dunod, 2014.
- (26) Bedioui, F. Voltampérométrie. Théorie et Mise En Œuvre Expérimentale. *Tech. l'ingénieur* **2015**, p2126.
- (27) Brett, C. M. A.; Brett, A. M. O. *Electrochemistry: Principles, Methods, and Applications*; Oxford University Press: USA, 1993.
- (28) Darchen, A. Électrochimie Appliquée: Caractérisations Des Systèmes Électrochimiques. *Tech. l'ingénieur* **2013**, k800.
- (29) Girault, H. H. *Analytical and Physical Electrochemistry*, 1st Ed.; EFLP Press, 2004.
- (30) Albu, S. P. Morphology and Growth of Titania Nanotubes - Nanostructuring and Applications (Thesis), Universität Erlangen-Nürnberg, 2012.
- (31) Denuault, G.; Sosna, M.; Williams, K.-J. Classical Experiments. In *Handbook of Electrochemistry*; Zoski, C. G., Ed.; Elsevier, 2007.
- (32) *Handbook of Electrochemistry*; Zoski, C. G., Ed.; Elsevier, 2007.
- (33) Fan, F.-R. F.; Fernandez, J.; Liu, B.; Mauzeroll, J. Scanning Electrochemical Microscopy. In *Handbook of Electrochemistry*; Zoski, C. G., Ed.; Elsevier, 2007.

-
- (34) Forster, R. J.; Keyes, T. E. Ultramicroelectrodes. In *Handbook of Electrochemistry*; Zoski, C. G., Ed.; Elsevier, 2007.
- (35) Wittstock, G.; Burchardt, M.; Pust, S. E.; Shen, Y.; Zhao, C. Scanning Electrochemical Microscopy for Direct Imaging of Reaction Rates. *Angew. Chemie - Int. Ed.* **2007**, *46* (10), 1584–1617.
- (36) Bedioui, F.; Griveau, S.; Pailleret, A. Microscopie Électrochimique. *Tech. l'ingénieur* **2009**.